"A Parametric Analysis of the BISRU Sled Tester's Dynamic Response"

Masters Dissertation

In the Department of Mechanical Engineering

University of Cape Town

Patrick M Smith

August 2009

Supervisors:

Prof GN Nurick
Mr KJ Balchin

DECLARATION

"I know the meaning of plagiarism and declare that all the work in the document, save for that which is properly acknowledged, is my own".

_____

Patrick Montague Smith

ACKNOWLEDGEMENTS

The author would like to extend his appreciation to the following people:

Professor G.N. Nurick for his guidance and experience as the supervisor this study.

Mr K.J. Balchin for his support and technical knowhow which was invaluable during this study.

Mr V.H. Balden for his help with ABAQUS and his extensive modelling knowledge.

Mr G. Perks of FESTO for his willingness to provide information regarding the pneumatic system.

Mr T. J. Cloete for input regarding the loading of the sled at the moment of impact.

Ms J.M. Fryer for her untiring correction of grammatical and typographical errors and patience over the past year.

My parents for their devotion to my upbringing and all the sacrifices they have made.

Josie, my sister, for her personal support and supply of cupcakes.

ABSTRACT

In order to test the effects of high decelerations on a range of mechanical components and human surrogates the Blast Impact and Survivability Research Unit (BISRU) is in the process of commissioning a sled tester.

Due to the high accelerations experienced by the sled, the effects of the inertial forces experienced by the sled and the rail system are important. A method predicting the maximum velocity reached by the sled and the dynamics of the entire system was also required.

A predictive simulation of the sled loading and dynamics during the deceleration stage had already been written by the suppliers of the deceleration equipment. Modifications were made to the Deceleration Stage model to allow the result to be imported to the finite element model more easily.

A model of the acceleration was written to predict the loading on the sled during the acceleration stage. The model was written in such a way that input parameters of a particular test could be easily adjusted to analyse their affect. Using the results of the Acceleration Stage model as inputs to the Deceleration Stage model, loading profiles for a particular set of input parameters for both stages were predicted.

The finite element model, of the rail system and conceptual design of the sled, was loaded using these profiles. The results allowed structural integrity of the rail system to be analysed as well as improvements to the conceptual design of the sled to be made.

The final version of the Acceleration Stage model predicted the dynamics of this stage well, while adjustments needed to be made to the results of the Deceleration Stage model due to a numerical anomaly. The finite element model showed high stresses in the rail system which needed to be addressed. As construction of the rails had already begun, modifications which changed the existing design as little as possible were necessary. A suggestion of a workable solution is given in Appendix A. Areas of the conceptual sled design which needed to be reviewed were also highlighted by the finite element analysis.

CONTENTS

Declaration i

Acknowledgements ii

Abstract iii

List of Figures vii

List of Tables xii

Glossary of Terms xiii

List of Symbols xiv

1 Introduction 1

2 Background to the Development of the Sled Tester Design 6

2.1 Overview of the BISRU Sled Tester 6

2.2 Limiting Specifications of the Design 7

2.3 Deceleration Methods Considered 8

2.4 Central Control System 12

2.5 MOOG Control System 14

2.5.1 Overview 14

2.5.2 Control Parameters 15

2.6 Stroke Cushioning 20

3 Theory 22

3.1 Pneumatic Theory 22

3.1.1 The Ideal Gas Law 22

3.1.2 Friction Factor 22

3.1.3 Accounting for System Losses 25

3.1.4 Flow Rate Calculations 27

3.2 Pneumatic System Models 31

3.2.1 Beater Model 31
3.2.2 Mare Model 36
3.3 Friction Models 40
4 Modelling of System Dynamics 44
4.1 Introduction 44
4.2 Development of the Acceleration Stage Model 45
4.3 Simulink Model of the Deceleration Stage 53
4.3.1 Digital Controller 55
4.3.2 Sled and Hydraulic Mechanical System 62
4.4 Combining the Acceleration and Deceleration Stage Models 65
4.5 Outputs from the Acceleration and Deceleration Stage Models 67
5 Finite Element Model of the Sled Tester 70
5.1 Introduction 70
5.2 Model Description 70
5.2.1 Model Geometry 71
5.2.2 Material Properties 81
5.2.3 Meshing and Elements 84
5.3 Assembly 90
5.4 Constraints 93
5.5 Interactions 95
5.6 Boundary Conditions 96
5.7 Loading 96
5.7.1 Loading using a Velocity Boundary Condition vs Force 99
5.7.2 Deceleration Stage Numerical Anomaly 100
6 Results and Analysis 106
6.1 Acceleration Stage Simulation 106

6.2 Deceleration Stage Simulation 122
6.3 Finite Element Analysis 130
6.3.1 Modal Analysis 130
6.3.2 Dynamic Analysis 134
7 Discussion 149
8 Concluding Remarks 154
9 Works Cited 157
10 Appendix A: A Recommended Solution ..... A i

LIST OF FIGURES

Figure 1-1: Photos of the sled tester during construction....1
Figure 1-2: Photo showing the 12 ports on the acceleration manifold and the rear of the cylinder....2
Figure 1-3: Flow chart showing what work was completed for this thesis....5
Figure 2-1: Schematic of the BISRU Sled Tester....6
Figure 2-2: Schematic of the eddy current braking method....9
Figure 2-3: Schematic of the braking method using ploy urethane tubes....10
Figure 2-4: Schematic of the braking method using steel bar....11
Figure 2-5: Schematic of the control system....13
Figure 2-6: Labelled photograph of the deceleration system....14
Figure 2-7: Labelled schematic of MOOG cylinder....15
Figure 2-8: Schematic of an adjustable cushioning system (8)....20
Figure 3-1: Moody Diagram showing Darcy friction factors (12)....23
Figure 3-2: Schematic showing the separation region in a 90° bend (11)....26
Figure 3-3: Typical plot of mass flow rate vs pressure ratio for the sonic conductance model....29
Figure 3-4: A labelled schematic of a cylinder....35
Figure 3-5: Plot of simulated and actual piston displacements and velocities (14)....37
Figure 3-6: Plot of chamber pressure time history for validation test (14)....38
Figure 3-7: Plot of difference between the simulated and experimental results (14)....39
Figure 3-8: Classic Friction model showing Static and Coulomb friction....40
Figure 3-9: Friction model showing Static, Coulomb and Viscous friction....41
Figure 3-10: Friction model including Stribeck friction....42
Figure 4-1: Plot of the friction between the piston and the cylinder casing for FESTO's DNG-250-PPV cylinder (15)....51
Figure 4-2: Plot of the quadratic functions reproducing the cylinder friction curve....52
Figure 4-3: Screenshot of the main window of SDS_5.mdl (23)....54
Figure 4-4: Screenshot of the controller unit window (23)....56
Figure 4-5: Screenshot of the input dialog for the sled demand (23)....57
Figure 4-6: Extract of Position Control PID from the controller window (23)....58

Figure 4-7: Extract of the pressure contol PID section from the control window (23) 59
Figure 4-8: Simplified schematic the P/X Mode logic 61
Figure 4-9: Screen shot of the Sled Hydro Mechanincal System window 64
Figure 4-10: Flow diagram of the combined simulation script file 66
Figure 5-1: Photos showing the construction of the rail support structure 71
Figure 5-2: Cross sections of physical rail components 72
Figure 5-3: Dimensions used to create the shell models of the rail supports and cross members 73
Figure 5-4: Image of the Cross Member part 74
Figure 5-5: Image of the entire left hand side rail support including the braces 75
Figure 5-6: Enlargements of the deceleration end of the left hand side rail support 75
Figure 5-7: Sketch showing the simplifications made to the rail geometry 76
Figure 5-8: Images of the modelled slide geometry 77
Figure 5-9: Image of the first revision of the sled design 78
Figure 5-10: Image of the second sled revision 79
Figure 5-11: Image of the final revision of the sled 80
Figure 5-12: Dimensioned image of the final revision of the sled model 80
Figure 5-13: Graphical representation of the rail support section assignments 83
Figure 5-14: Graphical representation of the sled section assignments 84
Figure 5-15: Definitions of ABAQUS shell offsets 88
Figure 5-16: Sketch of normals used for circular sections 89
Figure 5-17: Graphical representation showing the shell normal orientations and shell offsets 90
Figure 5-18: Image of locations of cross members relative to the rail supports 90
Figure 5-19: Image showing the alignment of the bolt holes in the cross members and the rail supports 91
Figure 5-20: Image of showing the placement of the rails relative to the rail supports 91
Figure 5-21: Image showing the vertical alignment of the sled, slides and rails 92
Figure 5-22: Isometeric view of the entire model assembly 92
Figure 5-23: Image showing the tie constraints involving the rail supports 93
Figure 5-24: Photo showing the bolts attaching a rail to its support 94
Figure 5-25: Image showing the constraints involving the sled 95

Figure 5-26: Plot of the acceleration force profile 97
Figure 5-27: Plot of the different deceleration force profiles 98
Figure 5-28: Image of the sled during the acceleration stage when using a varying velocity boundary condition 99
Figure 5-29: Plot of the deceleration force profile directly from the Deceleration Stage simulation.....101
Figure 5-30: Sketch describing varibles used in the derivation 102
Figure 5-31: Schematic of the spring mass model.....103
Figure 5-32: Plot of the reproduction of the 170 MN spike created by the Spring Mass model 103
Figure 5-33: Plots of the Impact force profiles from the impact simulations 104
Figure 5-34: Plot of the Deceleration Stage model force profile overlayed with the impact simulation results.....105
Figure 6-1: Plot of pneumatic chamber pressures histories for the maximum velocity simulation.....107
Figure 6-2: Plot of the piston velocity history for the maximum velocity simulation 108
Figure 6-3: Plot of the pneumatic piston velocity vs stroke for the maximum velocity simulation.....109
Figure 6-4: Velocity vs stroke plot if no cushioning air is used.....110
Figure 6-5: Plot of the sled velocity history for the maximum velocity simulation 110
Figure 6-6: Surface plot showing the effect of the input parameters on the final sled velocity 112
Figure 6-7: Comparative plot of velocity histories for simulations with similar final sled velocities 113
Figure 6-8: Comparative plot of the velocity vs stroke profiles for simulation with similar final sled velocities.....114
Figure 6-9: Comparative plots of the chamber pressure histories for simulations with similar final sled velocities 115
Figure 6-10: Plot of the velocity histories for simulations using 12 acceleration valves.....115
Figure 6-11: Comparative plot of the velocity histories of simulations with a supply pressure of 10 bar 116
Figure 6-12: Plot of the variation of decay time with an increase in acceleration valves.....117

Figure 6-13: Comparative plot of using different numbers of cushioning valves 118
Figure 6-14: Comparative plot of the velocity vs piston position profiles for varying numbers of deceleration valves.....119
Figure 6-15: Comparative plot of chamber pressure profiles for varying numbers of deceleration valves 119
Figure 6-16: Plot of the sled velocity and deceleration profiles for a 100 bar set point.....123
Figure 6-17: Plot of the effective pressure history for a 100 bar set point 125
Figure 6-18: Comparative plot of the Deceleration velocity profiles with set points of 100 and 200 bar 126
Figure 6-19: Comparative plot of the sled and piston positions for the 100 and 200 bar simulations 127
Figure 6-20: Comparative plot of Piston and Sled positions showing the effect of an end stop collision 128
Figure 6-21: Comparative plot of the effective pressure profiles for the 100 and 200 bar simulations 129
Figure 6-22: Plots of the sled eigenmodes 131
Figure 6-23: Base state for the Modal analysis of the Rail system and the contour legend..132
Figure 6-24: plots of the rail system eigenmodes 133
Figure 6-25: Contour plot of a slide at is maximum stress state 135
Figure 6-26: Contour plot of sled at its maximum stress state 136
Figure 6-27: Force distribution across the sled impact area from the auxiliary simulations.136
Figure 6-28: Contour plot of the maximum stresses of the cross members.....138
Figure 6-29: An exagerated deformation of the forst cross member 139
Figure 6-30: Contour plot of the stresses in the rail supports at a brace connection point..140
Figure 6-31: Contour plot of the stresses in the rail supports over the entire deceleration region 141
Figure 6-32: Displacement contour plot of the rail system exhibiting mode 9 behaviour 142
Figure 6-33: Displacement contour plot of the rail system exhibiting mode 8 behaviour 142
Figure 6-34: Displacement contour plot of the rail system exhibiting mode 8 and 9 behaviour 143
Figure 6-35: Comparative plot of the kinetic energies of the different loading scenarios 144

Figure 6-36: Comparative plot of the total strain energies for the different loading scenarios 145
Figure 6-37: Comparative plot of the acceleration experience by the dummy mass during the deceleration stage 146
Figure 6-38: Comparative plot of the dummy mass velocity over the entire simulation 147

LIST OF TABLES

Table 2-1: Optimised Control Parameters proposed by MOOG (6) 18
Table 3-1: Absoulte roughness of some commonly used piping materials (13) 25
Table 3-2: Table of separation loss coefficients (11) 26
Table 3-3: Table of ISO 6358 standard conditions 30
Table 3-4: Table of simulation errors 39
Table 4-1: Valve properties for the festo MHF-3-3/4-S solenoid valve (15) 49
Table 4-2: Truth Table showing the results of the P/X Mode logic 62
Table 5-1: Mechanical properties of the materials used 81
Table 5-2: Material yield strengths 82
Table 6-1: Table of maximum sled velocities for combinations of input variables 111
Table 6-2: Examples of input parameter sets with similar final sled velocities 112
Table 6-3: Differences in the simulation conditions 120
Table 6-4: Comparison of the FESTO and Acceleration Stage model velocity predictions 120
Table 6-5: Maximum stresses in the slides instances 134
Table 6-6: Maximum stresses in the sled 135
Table 6-7: Maximum stresses in the cross members 137
Table 6-8: Maximum stresses in the rail supports 139

GLOSSARY OF TERMS

Acceleration Stage model:
A time discretised model created in this study of the pneumatic cylinder and sled based on pneumatic theory to predict the dynamics of the cylinder and sled.

Dead Volume:
A dead volume is any volume between the closed valve and the piston when it is abutted against the end cap of the chamber in question.

Deceleration Stage model:
A model based in Simulink of the deceleration system, including the control system and mechanical components. The model was written by the suppliers of the system.

Delivery Pressure:
The pressure of the fluid or gas after it has passed through a valve.

SCADA:
Supervisory Control and Data Acquisition – A computer system which forms an interface between a system of equipment and its operator; simple schematics and command button show the status of and control the equipment.

PID Controller:
Proportional-Integral-Derivative Controller – A controller used in feedback control. The controller uses feedback of the controlled parameter, its integral and derivative to track a set point.

PLC:
Programmable Logic Controller – An electronic device which can monitor and emit voltages; binary logic programmed into the device controls the output signals depending on the status of the input signals.

Supply Pressure:
The pressure of the fluid or gas received by a valve from its supply vessel

Working Volume:
The working volume is the increase in volume from the dead volume value when the piston moves from against the end cap to a new position.

LIST OF SYMBOLS

a	Acceleration
A	Area
b	Critical Pressure Ratio
c	Wave Speed
C	Sonic Conductance
c_p	Specific Heat for const pressure
c_v	Specific Heat for constant volume
D	Diameter
e	Absolute pipe roughness
E	Elastic Modulus
f	Friction Factor
F	Force
k	Separation Loss Coefficient
K	Spring Constant
l	Length
m	Mass
P	Pressure
Q	Flow Rate
R	Gas Constant
Re	Reynolds Number
T	Temperature
t	Time
v	Velocity
V	Volume
x	Distance
β	Bulk Modulus
Δ	Change in
γ	Ratio of Specific Heats
ε	Error
ϵ	Strain
μ	Dynamic Viscosity
ρ	Density
σ	Stress
d/dt	Time Derivative
$\dot{}$	Time Derivative
δ	Partial Derivative

Subscripts

a	Rear Chamber
b	Front Chamber
$bore$	Cylinder Bore
c	Closing
cyl	Cylinder
d	Darcy
e	Maximum Available from Energy
eff	Effective
f	Fanning
in	Into Chamber
n	Required
o	Reference (ISO6358 Standard)
out	Out of Chamber
pis	Piston
pre	Pre-acceleration
s	Supply
t	Target

1 INTRODUCTION

At the Blast Impact and Survivability Research Unit (BISRU), the effects of blast and impact loading on structures and how these effects affect human and equipment survivability are investigated.

At present the unit is commissioning a sled tester (shown in Figure 1-1), which will be used to test the affects of the high deceleration on a range of specimens, including human surrogates. The sled tester consists of a rail system on which the sled slides between a pneumatic and a hydraulic cylinder. The pneumatic cylinder will accelerate the sled up to a maximum velocity of 17 m/s; the sled will then be released from the pneumatic cylinder and coasts towards the extended hydraulic cylinder. After the sled has made contact with the end of the hydraulic piston, the hydraulic cylinder (assisted by a sophisticated control system) will decelerate the sled at a rate of up to 59g.

FIGURE 1-1: PHOTOS OF THE SLED TESTER DURING CONSTRUCTION

To achieve all this in the space available accelerations of up to 10g during the acceleration stage were necessary. In order for the pneumatic cylinder to be able to exert sufficient force on the sled a custom cylinder was necessary. The combination of the required stroke (>2.5

m), bore diameter (250 mm) and flow rates into and out of the chambers could not be accomplished with a standard cylinder. To retain adequate pressure in the rear chamber of the cylinder as the piston extended a very high flow rate of supply air into the chamber is required. As the largest valve available from the suppliers did not deliver enough flow, multiple valves were used. Custom end caps were machined for both ends of the cylinder, allowing 12 solenoid valves (not shown in Figure 1-2) to service the rear chamber and 6 identical valves the front chamber (the front chamber would be pressurised to release the sled and cushion the piston).

FIGURE 1-2: PHOTO SHOWING THE 12 PORTS ON THE ACCELERATION MANIFOLD AND THE REAR OF THE CYLINDER

In the case of the rear chamber the benefits of have multiple valves were twofold: sufficient flow was available for the maximum velocity case; and being able to change the number of activated valves at the beginning of a test gave another element of control. The velocity of the sled as it is released is influenced be two factors: the supply pressure and the number of acceleration valves activated.

For the front chamber all 6 valves need to be activated for every test to ensure that no cushioning air is lost through inactivated valves. This is a reality of the pneumatic circuit. Hence, the multiple valves only provide sufficient flow in this case.

Due to the higher pressures available to hydraulic systems, the required bore diameter of the hydraulic cylinder was 100 mm. The higher g-force experienced during the deceleration stage resulted in a shorter stroke of 1.1m being required. The challenge that the deceleration stage designers faced was the short duration of the stage. Pressures, flow rates and positions all need to be accurately controlled over the duration of the stage, which is

less than 130 ms in the 59g case. Because of this, a highly sophisticated control system was necessary to monitor the deceleration stage equipment.

During and between the acceleration and deceleration stages the sled slides along the rails. High accelerations and decelerations of the sled create large inertial forces which need to be survived by the rail system, specimen restraint system and the sled itself. To investigate the effects of these forces, the dynamics of the sled during the both the acceleration and deceleration stages needed to be known as well as the interactions between the sled and rails.

To predict the dynamics of the pneumatic system, a model of the acceleration stage was created. As a model of the deceleration stage had already been created by the suppliers of the hydraulic control system, it was not necessary to model this stage. The inner workings of supplier's model were investigated and the output adapted slightly to allow the results to be included into a finite element simulation. The resulting force profiles experienced by the sled during both of these stages were used as the loading in a finite element model of the rail system and conceptual sled design. A finite element analysis of these structures as well as an analysis of the sled dynamics was performed using the finite element model created in ABAQUS™ 6.8-2.

From the simulations: the dynamics of the acceleration piston for any combination of input parameters could be analysed; regions of high stress in the rail system were identified; the conceptual design of the sled was shown to be a workable solution; the dynamics of the deceleration stage were able to be linked to the results of a particular acceleration stage; and the dynamic effects experienced by the test specimen could be predicted.

As this thesis forms part of a larger project of commissioning the sled tester, an explanation of its position relative to previous work and future developments needs to be made clear. The purpose of this study was: to analyse the dynamics of the sled and piston during the acceleration stage; extract data from and investigate the existing model of the deceleration stage; and use the information from the two stages to analyse the response of the rail system and sled. At the start of this study: the designs of the pneumatic and hydraulic system were complete; construction had begun on the rail system; the specifications and a

rough concept of the sled design were available and a model of the deceleration stage had been created by the suppliers.

Completion of this thesis resulted in: a model of the response of sled dynamics to the input parameters for the acceleration stage, which was combined with the deceleration stage model for convenience; using the outputs from this combined model the structural response of the rail system and a workable conceptual sled design had been analysed using a finite element model.

Apart from being able to predict the sled and piston dynamics over the entire duration for any test conditions, the structural weaknesses in the rail system were highlighted and modifications were suggested. The conceptual design of the sled was improved to the point where only minor details needed improvement to result in a structurally sound design which satisfied the specifications. Figure 1-3 breaks down the project using a flow chart.

In the chapters that follow the background to the development of the sled design and a study of theory relevant to the model of the pneumatic system take the place of a traditional literature review. The creation of the Acceleration Stage Model is then detailed. This is followed by an investigation into the Deceleration Stage model and the combining of this with the existing Acceleration Stage Model is explained. A description of the finite element model and how it was constrained and loaded is then given. The results of the different simulations are presented and analysed. Finally the important points about the results are discussed and concluding remarks are made.

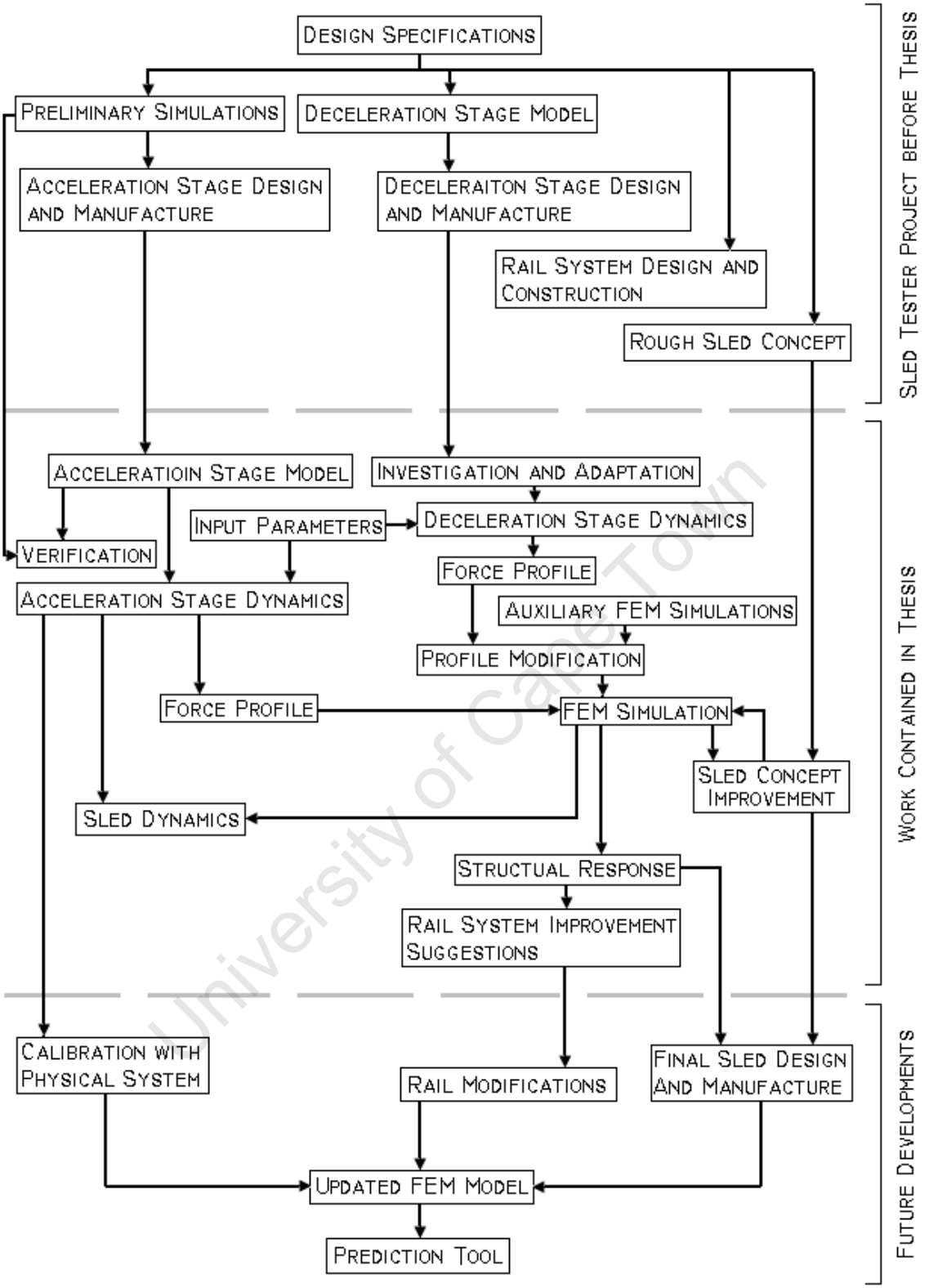

FIGURE 1-3: FLOW CHART SHOWING WHAT WORK WAS COMPLETED FOR THIS THESIS

2 BACKGROUND TO THE DEVELOPMENT OF THE SLED TESTER DESIGN

At the Blast Impact and Survivability Research Unit methods of protecting humans and equipment from blast and impact loads are investigated. Part of this research deals with the human response to these loading conditions. Impact loading occurs over a very short period, normally less than 100 ms. These situations normally occur as the result of an unexpected event like a motor vehicle collision.

In an actual collision the vehicle either collides with another vehicle or a barrier. This causes a change in the vehicle momentum called an impulse. As long as the mass remains constant, the momentum change is proportional to the change in velocity of the body and is equal to the integral of the force experienced by the body with respect to time. Thus the effects of many of these collisions can be simulated by using an external force to slow down the moving subject extremely quickly.

2.1 OVERVIEW OF THE BISRU SLED TESTER

The Sled Tester has been designed to apply large decelerations to the sled which holds a test specimen. Examples of the test specimen are: a human surrogate like the Hybrid III anthropomorphic test dummy, a surrogate of a specific part of the human body, a prototype of a design which has to withstand high levels of acceleration or a combination of these.

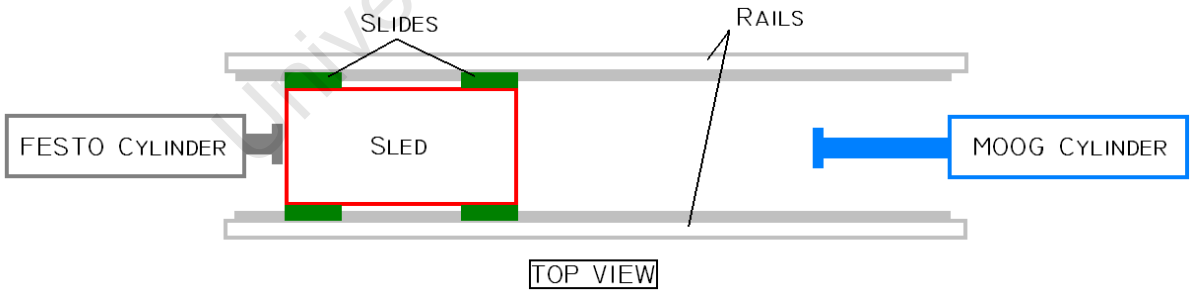

FIGURE 2-1: SCHEMATIC OF THE BISRU SLED TESTER

Figure 2-1 shows a schematic of the BISRU Sled Tester. For a combined sled and payload mass of 300 kg the FESTO's cylinder is capable of accelerating the sled at 10g, up to a velocity of 17 m/s(1). To avoid damage to the cylinder, cushioning air is compressed into the front chamber once the piston has passed the midpoint of the stroke. The cushioning air decelerates the piston eliminating any contact between the piston and the cylinder's end

cap. The pressures on either side of the piston eventually find an equilibrium point and the piston becomes stationary. After the pneumatic cylinder's cushioning air starts to decelerate the piston the sled continues along the rails losing contact with the end of the piston. It travels along the rails until it reaches the MOOG hydraulic cylinder.

As the sled approaches the hydraulic cylinder its control system starts to retract the piston at the same velocity as the sled. Once the sled has made contact with the piston, the control system regulates the effective pressure of the cylinder to the prescribed set point. This results in a deceleration of the sled, bringing it to rest. The cylinder is capable of decelerating the sled at up to 59 g(1).

2.2 LIMITING SPECIFICATIONS OF THE DESIGN

The tightest constraint on the design was that the space available in the BISRU lab was limited. An area 14 m long and 5 m wide was allocated to the project. Problems that arose from this were two fold. Firstly all the components of the design needed to fit in to the area without obstructing the motion of the sled and secondly that the distance available to accelerate the sled to the maximum velocity was extremely short. The latter meant that the acceleration during the initial stage would be relatively high (10 g)(2). This had the potential to effect the desired positioning of the test specimen if not secured carefully.

Due to the high deceleration of the sled during the final stage of the test special considerations for the method used to anchor the deceleration unit needed to be made. The anchoring system needed to withstand the inertial forces created by the deceleration as well as rigidly hold the cylinder in position to allow the control system to accurately calculate the difference in the sled and piston velocities. For this reason the hydraulic cylinder was mounted via a rigid bracket to a specially cast concrete slab. By reinforcing the slab into the exiting building structure the effective mass of the deceleration system was increased enormously. This resulted in there being negligible movement of the cylinder during the deceleration phase.

2.3 DECELERATION METHODS CONSIDERED

A few different methods to decelerate the sled were investigated during the initial stages of the project. After careful consideration the hydraulic cylinder used in the final design was chosen.

Although not the most cost effective solution the hydraulic cylinder concept had many desirable features.

Once installed the system would not need any physical adjustment or change parts. The control system would attempt to keep the effective pressure of the cylinder at a user inputted set point. By changing the set point, the pressure in the cylinder during the deceleration stage could be adjusted; changing the magnitude of the deceleration.

The control system ensured repeatability. For similar input parameters the sled would be exerted to a deceleration of the same magnitude. Another benefit of the control system was that it allowed the deceleration to be kept constant over the duration of the stage. Furthermore as the control system included a number of sensors, some basic information from the deceleration stage including chamber pressures and the sled's dynamics were available.

Although the design and installation of the control system required specialised skills, local contractors possessed the expertise. Local support teamed with the superior results attained by the control system lead to the decision to implement the hydraulic cylinder concept.

Other methods considered where a magnetic eddy current concept, a polyurethane tube and olive method and the plastic deformation of steel bar.

The magnetic eddy current concept consisted of a set of magnets arranged in parallel and a matching set of metallic fins. Either the magnets or the fins could have been fixed to the sled and the other grounded. The system would have been arranged so that the fins passed through the magnetic fields during the deceleration stage of the test. As the fins moved through the magnetic field a force described by Lenz's law would have resisted the movement of the material and decelerate the sled. By utilising materials with a range of different magnetic properties the sled could have been decelerated at varying rates

depending on: the strength of the magnet used; the type of material used to make the fins and the number of magnet fin pairs in parallel(3).

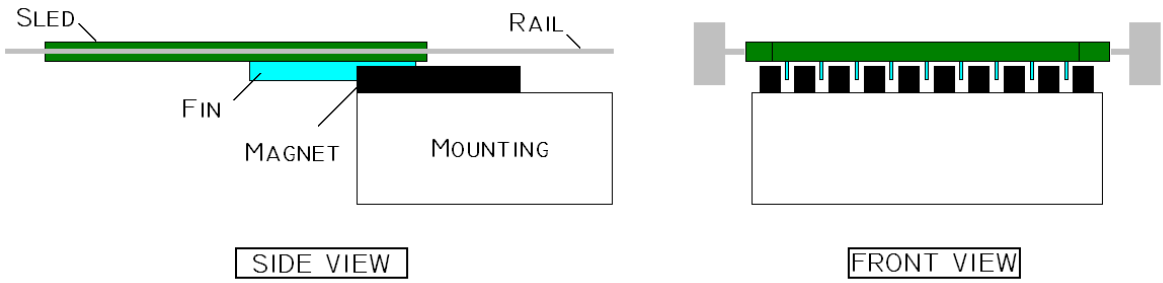

FIGURE 2-2: SCHEMATIC OF THE EDDY CURRENT BRAKING METHOD

After an investigation, by German company InTraSys(3), into this method it was found that a range of different decelerations were possible using this method. As the fins entered the magnetic fields the decelerating force was exerted on the sled. This force increased as the sled progresses as it is proportional to the area of the fin interacting with the magnetic field(3). Although not constant the deceleration of the sled could have peaked at 50 g as long as the initial velocity of the sled is high enough.

The method was discarded because it would have required parts to be changed to achieve different decelerations and these would not be constant over the deceleration stage. Other contributing factors were that: only discrete deceleration values would have been achievable; there was a lack of local support as the only supplier was based in Germany; and the equipment was relatively expensive(4).

Another method that was considered used friction. In this method a steel olives would have been connected to the sled, which would slide into a polyurethane tube at the beginning of the deceleration stage. Depending on the number of tubes engaged by the olives the force exerted on the sled could be varied, varying the degree of deceleration.

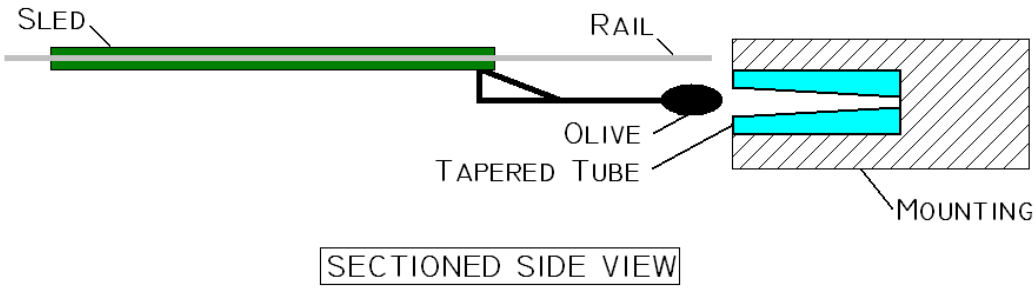

FIGURE 2-3: SCHEMATIC OF THE BRAKING METHOD USING PLOYURETHANE TUBES

The variety of decelerations possible with this system was limited to the number of recesses in the mounting. By adding or removing tubes from the recesses the number of engaging olives could have been altered. The tubes were designed for the used in full scale motor vehicle collision experiments. This meant that the deceleration force created by the engagement of one tube was relatively large; reducing the resolution of the achievable decelerations. As the magnitude of the decelerating force was dependent on the mechanical properties of the polyurethane fluctuations in room temperature would have altered the achievable magnitudes(4).

As with the magnetic eddy current concept, the polyurethane tube and olive concept could only achieve discrete deceleration values. It was also dependent on the temperature of the tubes and hence the room temperature. No local suppliers of the tube were found, increasing cost and lead times on the consumable components(4). For these reasons the concept was abandoned.

Using strain energy to dissipate the velocity of the sled and create the deceleration was also considered. A protruding lance from the front of the sled would have made contact with steel bar held across the sled's path. The kinetic energy of the sled would have been converted into strain and plastic deformation energy in the steel which would have decelerated the sled. Depending on the section dimensions of the steel and the number of bars held in front of the sled, the deceleration could have been changed.

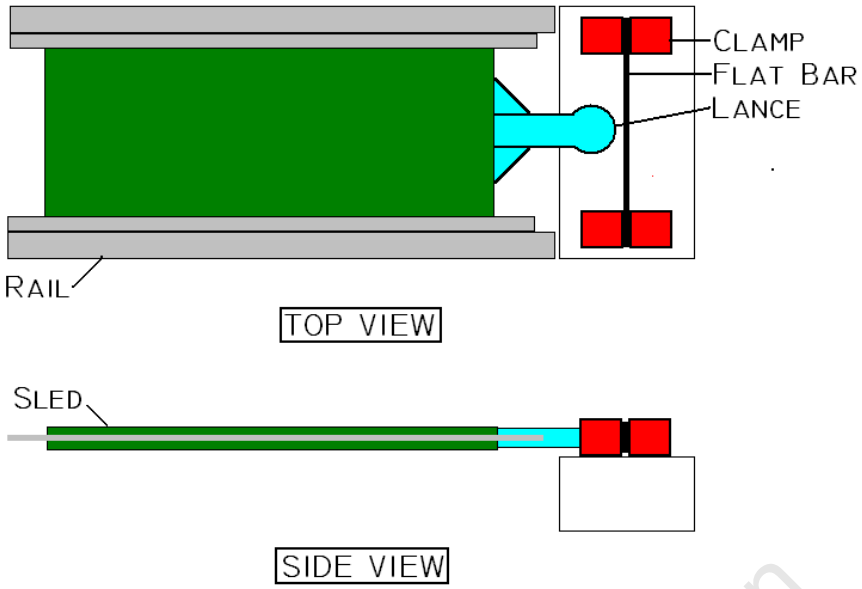

FIGURE 2-4: SCHEMATIC OF THE BRAKING METHOD USING STEEL BAR

The steel used in each run would have to have been scrapped after each run. As the deceleration would have been highly sensitive to the mechanical properties of the steel, the inconsistency of the material properties of low carbon steel could have affected the resulting deceleration. Another issue would have been clamping the ends of the bars rigidly enough so that there was no slippage of the steel through the clamps. A device which repeatedly held the steel bars in a rigid and consistent manner would have had to be devised.

This concept was discarded due to the use of sacrificial steel bars and the uncertainty surrounding the repeatability of the decelerations. The consumable cost and the incontrollable inconsistency outweighed this low cost alternative.

2.4 CENTRAL CONTROL SYSTEM

A central control unit (CCU) allows the acceleration and deceleration systems to communicate as well as managing the different interlock mechanisms to ensure safe operation of the sled tester. All operator input is captured by the CCU and instructions are then relayed to the necessary components.

The unit collects operator input via a SCADA system. This interface prompts the operator to perform safety checks and asks for input regarding the acceleration and deceleration events. In the case of the deceleration system, which has its own control system, the CCU merely relays the pressure set point and the control parameters to the MOOG system and waits for confirmation that the system is ready to receive the sled.

The SCADA system interprets the user input and controls the acceleration system directly via a PLC. The PLC also monitors the states of numerous pressure, proximity and safety interlock signals. Using this input in a logic sequence the PLC can either decide to allow the sled to be fired when requested by the operator or highlight an error which must be corrected before this is allowed. Figure 2-5 show a schematic of the communication connections.

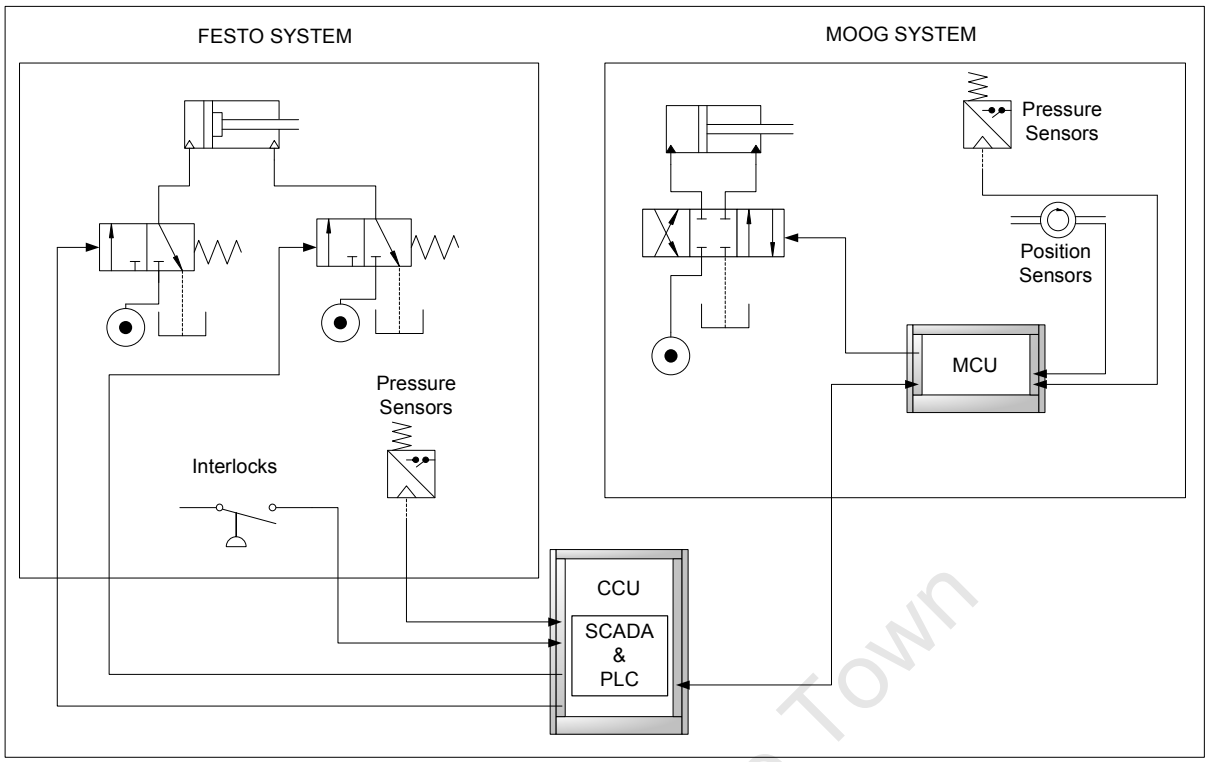

FIGURE 2-5: SCHEMATIC OF THE CONTROL SYSTEM

As the CCU is a crucial component in ensuring the safe operation of the entire system it has been fitted with uninterruptible power supply to safeguard against power cuts. The UPS also powers the PLC board which holds the two DC power supplies which energise the solenoid valves and other electronic components in the system. Multiple DC power supplies were specified to allow for redundancy, each power supply can provide enough power to run all the components connected to the board safeguarding against equipment failure(5).

2.5 MOOG CONTROL SYSTEM

2.5.1 OVERVIEW

The entire deceleration unit was designed and installed by outside contractors. The unit consists of a hydraulic cylinder whose motion is controlled by a high speed servo valve, a set of accumulators, a hydraulic power pack and a control unit. A pressure of 380 bar is achievable from the power pack(1).

The high speed servo valve, MOOG D665-4009, coupled with the control unit governs the velocity, position and pressures of the cylinder(1). Before the sled is fired the hydraulic cylinder is extended to the end of its stroke. After the sled is set in motion by the acceleration unit, the control system tracks the position and velocity of the sled via a servo operated potentiometer. Figure 2-6 shows some of the systems components.

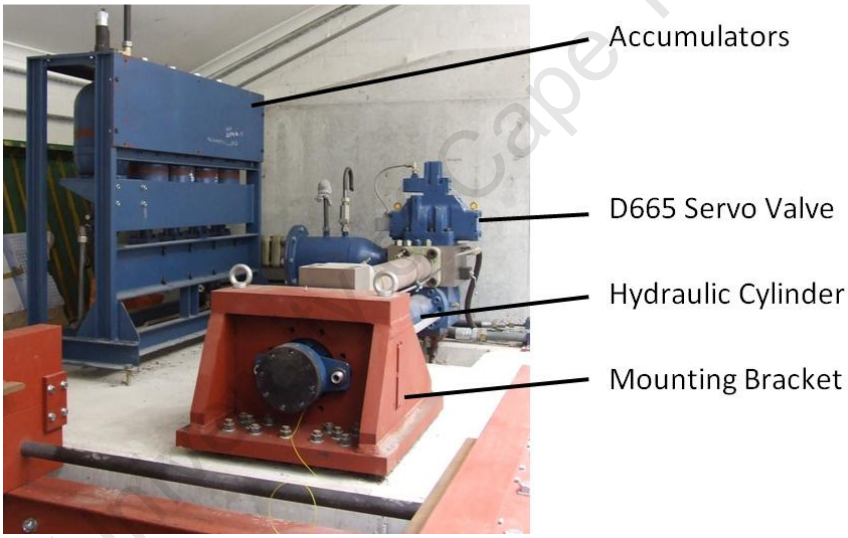

FIGURE 2-6: LABELLED PHOTOGRAPH OF THE DECELERATION SYSTEM

Depending on the control parameters, which are set before the test, a pre-acceleration distance is prescribed. When the distance between the sled and the end of the piston reduces to the pre-acceleration distance the piston is set in motion to match a velocity of the sled minimising the impact when the sled contacts with the end of the piston(1). Once the sled has made contact with the piston the control unit attempts to keep the effective pressure of the cylinder equal to the prescribed set point pressure(1).

The accuracy and speed to which the set point pressure is matched by the actual pressures is dependent on the control parameters and gains prescribed to the controller. The input

and control parameters selected by the operator would be sent to the hydraulic unit before the firing sequence is initiated. As well as the parameter input a series of electronic handshakes need to be performed to ensure that the hydraulic system is prepared for the impact(5). After these have taken place the central unit will initiate the test. All user input is entered via the central control unit's touch screen.

After the completion of the test, data from the hydraulic control unit can be sent back to central unit. These data include the cylinder pressures and the sled position with time, from which the velocity and acceleration can be calculated. This can then be combined with other information collected and a test log can be compiled.

2.5.2 CONTROL PARAMETERS

By taking into account the cylinder's bore and the mass of the sled and its payload the required set point for a specific deceleration can be calculated. Three control parameters need to be set to their optimal values which depend on the set point pressure, the contact velocity of the sled and the mass of the sled and piston rod. Optimised values of the parameters can be estimated from the Parameter Adjustment Equations supplied by MOOG in their model operation documentation(6). Below are the equations and an explanation of each.

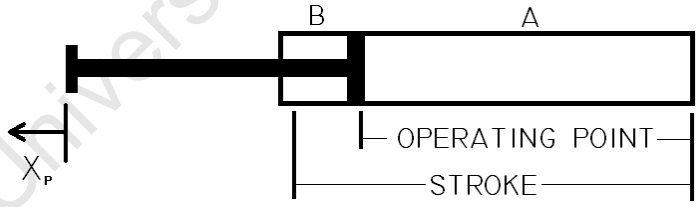

FIGURE 2-7: LABELLED SCHEMATIC OF MOOG CYLINDER

The no flow stiffness of the cylinder is the equivalent spring stiffness of the cylinder at a position, while the valves are sealed. Note that the extra volume of any piping etc between the chamber and the sealed valves must be taken into account when calculating the volumes(6). For this simulation the stiffness of the cylinder when it is extended to it operating point, is of interest. Equation 2-1(6) shows how the stiffness can be calculated.

EQUATION 2-1:

$$K = \beta\left(\frac{A_a^2}{V_a} + \frac{A_b^2}{V_b}\right)$$

Where β is the bulk modulus of the hydraulic fluid

The displacement necessary to create the target pressure can be calculated by Equation 2-2(6). X_n is needed to calculate the pre-acceleration distance and validate if the specified deceleration is attainable.

EQUATION 2-2:

$$x_n = \frac{P_t \cdot A_a}{K}$$

For cases where the sled has a low kinetic energy but a high deceleration is required, the system might not possess enough energy to compress the cylinder to the required target pressure(6). The achievable displacement at the no flow stiffness is given by X_e in Equation 2-3(6) and should be larger than X_n to ensure that the target pressure is attainable.

EQUATION 2-3:

$$x_e = \sqrt{\frac{m \cdot v^2}{K}}$$

Initially while the sled is approaching the cylinder the valve is held fractionally open, the extent to which it is a proportional to the target pressure and the contact velocity of the sled(6). By using the values from an optimised set of parameters a new value for the parameter set in question can be predicted. A_t is given as a voltage, which corresponds to an area, as this is what the control system reads this parameter as. The relation is given in Equation 2-4(6).

EQUATION 2-4:

$$A_t \propto \frac{v}{\sqrt{P_t + P_s \cdot \frac{A_b}{A_a}}}$$

As the sled approaches the cylinder and reaches a certain distance from its extended end, the piston is accelerated to try and match the speed of the incoming sled. Successful control

of the deceleration of the sled is sensitive to the pre-acceleration distance between the sled and the end of the piston rod. Thus the pre-acceleration distance needs to be changed when there is a change in the contact velocity. Equation 2-5(6) helps predict a suitable distance to prescribe related to an optimised parameter set.

EQUATION 2-5:

$$\left(x_{pre} + x_n\right) \propto v^2$$

Lastly the valve closing time needs to be specified. It is proportional to the mass of sled and the piston rod assembly and the target pressure. This parameter is also predicted from an optimised parameter set and is proportional to the mass and target pressure as shown in Equation 2-6(6).

EQUATION 2-6:

$$t_c \propto \frac{m}{P_t \cdot A_a}$$

The relations above highlight the need for the parameters set from a simulation that has been optimised to a satisfactory accuracy to be found. In the MOOG controller documentation(6) such a set has been put forward. The parameter set has been tabulated below in Table 2-1.

TABLE 2-1: OPTIMISED CONTROL PARAMETERS PROPOSED BY MOOG(6)

System Specifications		
Supply Pressure (Ps)	350	bar
Bore Diameter	100	mm
Rod Diameter	75	mm
Stroke	1100	mm
Cylinder Operating Point	1000	mm
Rod Side Additional Volume	8	litres
Bore Side Additional Volume	2	litres
Fluid Modulus	0.7	GPa
Input Parameters		
Target Effective Pressure (Pt)	100	bar
Sled Contact Velocity (V)	17	m/s
Sled and Rod Mass (M)	340	kg
Control Parameters		
Stiffness (K)	5372.5	N/mm
No Flow Displacement (Xn)	14.6	mm
Valve Ramp Start Area (At)	9	V
Pre-acceleration Distance (Xp)	80	mm
Valve Ramp Rate Closing Time (Tc)	0.105	ms

Gains in the PID controller can be adjusted to optimise the control of the system even further. This will be necessary for tests which input parameters differ largely from the parameter set for which the system is tuned.

MOOG performed a case study for a 250 kg sled where, the control parameters were tuned according to Parameter Adjustment Equations(6). In some cases the PID gains were also tuned. Velocities of 17, 10 and 3 m/s were considered with target pressures of 36, 100, 207 bar. The latter translates to decelerations of 10, 28 and 57 g respectively(1).

At higher loads apart from changes to the control parameters which are found from the equations described in this section, the damping in the PID controller needs to be increased to achieve satisfactory control(1).

The pre-acceleration position decreases with both decreasing contact velocity and increasing target pressure due to the increase of the no flow displacement, X_n, necessary to create the desired pressure. As seen when the contact velocity was set to 3 m/s, to achieve the target pressure a negative pre-acceleration position is found. This means that the piston

is only retracted after the sled has made contact with and displaced the piston. For the 3 m/s case in the study the kinetic energy of the sled was not high enough to compress the fluid to 207 bar and just managed to reach 100 bar. Thus showing that, the contact velocity not only determines the length of the deceleration but also the ability of the system to achieve the desired deceleration. Comparing the results of Equation 2-2 and Equation 2-3 would highlight if this were the case for a particular test.

2.6 STROKE CUSHIONING

In a pneumatic cylinder as the piston nears the end of the cylinder's stroke there is the possibility of the piston colliding with the end cap of the cylinder. If nothing is done to slow down the advance of the piston it will collide into the end cap with a high kinetic energy damaging the piston and the end cap. Depending on the mass and velocities of the cylinder components varying levels of protection are needed.

For small light cylinders the kinetic energy possessed by the piston is generally very small and a simple damping method, like lining the impact area of the end cap with a shock absorbing rubber, is sufficient(7). As the mass of the components increases more severe damping is required(8). Larger external damping equipment can be used to absorb the shock but can increase the size of the component's footprint dramatically, typically space is at premium and internal damping is a more attractive option(7).

By the damping mechanism being contained inside the cylinder the components footprint can be kept to a minimum saving valuable space and simplifying the mounting procedure. Although different manufacturers' detailed design may vary the basic principle remains the same. Figure 2-8 shows a diagram of the typical concept.

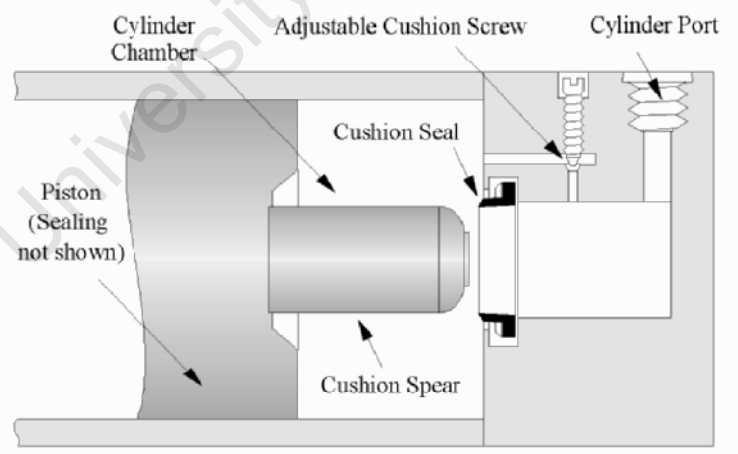

FIGURE 2-8: SCHEMATIC OF AN ADJUSTABLE CUSHIONING SYSTEM(8)

As the piston nears the end cap the cushioning spear, a rod protruding from the centre of the piston, passes through the cushioning seal blocking the cylinder's exhaust path. The remaining air is now trapped between the piston and the end cap creating an air cushion

between the components. A small amount of air is allowed to exhaust via the adjustable cushioning screw.

Adjusting the cushioning screw changes the size of the orifice that the trapped can escape through allowing the cylinder to be tuned to its exact application. Trapping the air in front of the piston creates an air cushion, which due to the compressibility of air this acts as a spring. This results in the air cushion and the mass of the piston and the rod becoming an oscillating spring-mass system(8) thus the ideal setting of the cushioning screw is a function of the piston velocity as the spear enters the cushioning seal and the mass of the rod and the piston. Where these parameters vary significantly a setting where adequate cushioning for all cases is achieved might be impossible(8). When cushioning is needed on the rod side of the piston the same method may be used by incorporating the spear into the design of the piston rod.

The cushioning seals operation is twofold, is acts as a seal and a check valve. When the spear has passed the seal and the piston is moving towards it, it simply seals the exhaust path. When the supply pressure is switched and applied to the cylinder port at the cushioned end, the seal allows the air to flow between the spear and itself(8). This allows a quicker build up of pressure in the main chamber than if the flow was restricted to only flowing passed the cushioning screw.

In the past the cushioning seal was nothing more than metal-on-metal contact between the spear and the recess. A second larger port, similar to the one holding the cushioning screw, was machined and fitted with a check valve to allow for a quicker return stroke(8).

3 THEORY

To be able to create the simulations of the acceleration stage it was necessary to consider the theory used to describe such systems. As the acceleration of the sled was provided by a pneumatic cylinder theory and models which described similar systems were investigated. The affect of friction on the dynamics of the piston and consequently the sled were important and methods of describing this complex phenomenon were also looked into.

3.1 PNEUMATIC THEORY

To be able to predict the pressures and flow rates in the different parts of pneumatic systems simulations need to be run which are grounded in pneumatic theory. The theory used is dependent on assumptions made about the nature of the system. By assuming that a system is isothermal or adiabatic the models can be simplified and less has to be known about the environment that the system resides in.

3.1.1 THE IDEAL GAS LAW

Using an equation of state allows the various properties of the gas to be linked together. The simplest of these equations which account for pressure, temperature, volume and mass is the Ideal Gas Law. The law assumes that the gas acts like an ideal gas which, has been found to be an acceptable assumption if the gas is at high temperature or low pressure compared to the critical values of these properties for the gas in question(9). The Ideal Gas Law can be used to predict the state of air at temperatures well below 0°C as its critical temperature is -147°C(9). The Ideal Gas Law equation of state is shown below(9):

EQUATION 3-1:

$$PV = mRT$$

The gas constant, R, is unique to a specific gas and in calculated from the universal gas constant and the molar mass of the gas. The gas constant for air is 0.2870 kJ/kg·K(9).

3.1.2 FRICTION FACTOR

Frictional losses in pipe flow are dependent on the diameter and roughness of the pipe and the Reynolds number of the flow (10)(11). To account for the frictional losses, friction factors based on these parameters were developed.

Depending on the type of flow in the pipe the calculation of the factor differs. During laminar flow the friction factor is only a function of the Reynolds number while during fully developed turbulent flow the factor is a function of the diameter and roughness of the pipe. In Figure 3-1 a Moody Chart is shown. Friction factors can be read off the chart for a range of combinations of the relative roughness of the pipe and the Reynolds number of the flow.

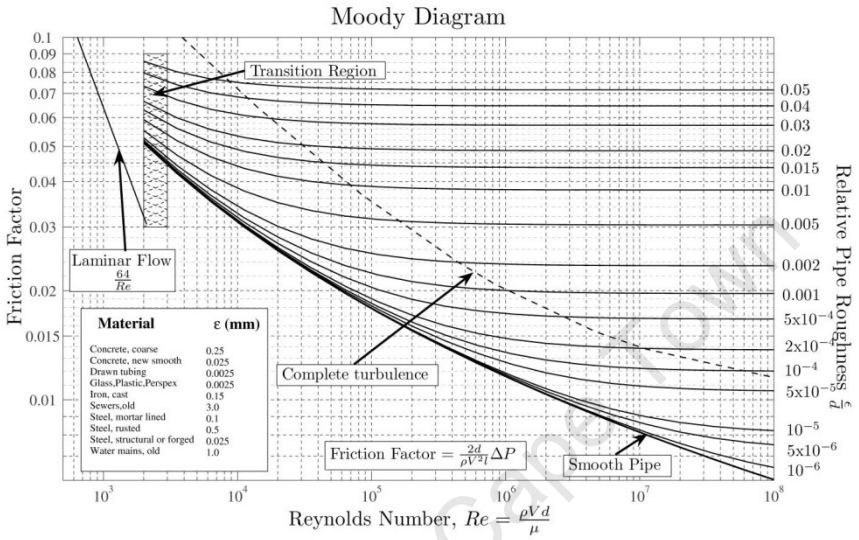

FIGURE 3-1: MOODY DIAGRAM SHOWING DARCY FRICTION FACTORS(12)

Two common friction factors exist, namely the Darcy and the Fanning factors. The two factors give similar profiles to each other, with the Darcy factor being four times greater than the Fanning factor (11). Care should be taken when using formula involving these factors to establish which factor has been used. The Darcy factor is commonly used in American texts (11).

An acid test for determining the friction factor is to consider the expression for the factor at laminar flows. Equation 3-2(11) shows the expression for the Fanning factor at laminar flows while Equation 3-3(10) shows the same for the Darcy factor.

EQUATION 3-2:

$$f_f = \frac{16}{Re}$$

EQUATION 3-3:

$$f_d = \frac{64}{Re}$$

Laminar flow is characterised as flow where the Reynolds number is less than 2320(10). The Reynolds number is defined for pipe flow cases as:

EQUATION 3-4:

$$Re = \frac{\rho v D}{\mu}$$

Where μ is the dynamic viscosity of the fluid

Once out of the laminar flow region the friction factors are described by the Colebrook-White equation. The equation was used by Moody to produce the Moody Chart(11). Two versions of the equation are shown below. Equation 3-5(11) is used to calculate the Fanning factor and Equation 3-6(10) for the Darcy factor. Examples of the absolute roughness of some commonly used pipe materials are given in Table 3-1

EQUATION 3-5:

$$\frac{1}{\sqrt{f_f}} = -4\log_{10}\left(\frac{e}{3.71D} + \frac{1.26}{Re\sqrt{f_f}}\right)$$

EQUATION 3-6:

$$\frac{1}{\sqrt{f_d}} = -2\log_{10}\left(\frac{0.269e}{D} + \frac{2.51}{Re\sqrt{f_d}}\right)$$

Where *e* is the absolute roughness of the pipe

TABLE 3-1: ABSOULTE ROUGHNESS OF SOME COMMONLY USED PIPING MATERIALS(13)

Material	e (m)
PVC, plastic, glass	0
Commercial Steel or Wrought Iron	4.50E-05
Galvanized Iron	1.50E-04
Cast Iron	2.60E-04
Asphalted Cast Iron	1.20E-04
Riveted Steel	9.0e-4 to 9.0e-3
Drawn Tubing	1.50E-06
Wood Stave	1.8e-4 to 9.0e-4
Concrete	3.0e-4 to 3.0e-3

Solving for the friction factor in the Colebrook-White equation requires a trial and error approach. This is not a problem when using a computer program but if the factor needs to be found by hand it is not practical. In these situations a Moody Chart is more helpful as the friction factor can be read off the chart directly.

3.1.3 ACCOUNTING FOR SYSTEM LOSSES

As a gas moves a long a pipe network there are friction and separation losses. The frictional losses are created by friction at the interface between the inside of the pipe and the gas flowing through it. When the flow passes an obstacle such as an orifice or a bend in the pipe, the flow is separated from part of the pipe wall. Both these types of losses result in a pressure loss, which can be described as an energy loss per unit volume (11). To model a pneumatic system these losses need to be quantified and their effect on the flow taken into account.

Frictional losses can be quantified using the friction factors discussed in section 3.1.2. Both Equation 3-9 and Equation 3-10 include the friction factor and take the effect on the pipe friction into account. When trying to calculate *f* for a pipe at a specific flow velocity, not in the laminar region, the absolute roughness is needed. For most commonly used piping materials the internal roughness are known and can be found in fluid textbooks.

Most piping used in modern pneumatic are made from polymers and have very smooth inner surfaces. So unless very long distances are covered by the piping the frictional losses normally are insignificant compared to the separation losses(11). Major separation losses occur at valves, sharp bends and changes in pipe diameter.

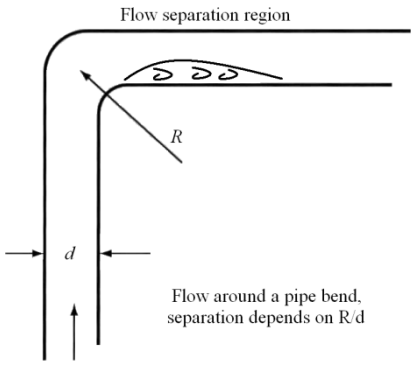

FIGURE 3-2: SCHEMATIC SHOWING THE SEPARATION REGION IN A 90° BEND(11)

A method of equivalent lengths is sometimes used to quantify separation losses. In this method the pressure loss due to the component in question is experimentally tested under controlled conditions. The loss is then converted into an equivalent length of piping used in the system. By adding the equivalent lengths of all the components in a pipeline to the actual length of the piping the separation losses can be accounted for.

From experimental investigation a separation loss coefficient can be calculated which allows the equivalent length of the component to be found for any pipe no matter what the friction factor or diameter is. Equation 3-7 (11) shows the relation between equivalent length and the separation loss coefficient, *k*.

EQUATION 3-7:

$$l_{eff} = \frac{kD}{f_d}$$

Where *k* is the separation loss coefficient

Some coefficients for common components are listed below.

TABLE 3-2: TABLE OF SEPARATION LOSS COEFFICIENTS(11)

Component	**K**
Open Gate Valve	0.25
Open Globe Valve	10
U-Bend	2.2
90° Bend	0.9
45° Bend	0.4
T-Junction	1.8
Sharp Pipe Entry	0.5

3.1.4 FLOW RATE CALCULATIONS

Knowing the flow rate of gas through different parts of the pneumatic system allows the mass of gas in different areas of the system to be calculated. This can be used in conjunction with the Ideal Gas Law to find the values of other properties of the gas.

For incompressible flow the Darcy equation can be used to calculate the velocity of the flow through a pipe. The flow rate is dependent on the length, diameter and friction factor of the pipe, the density of the flowing fluid and the pressure drop over the length of the pipe. The Darcy-Weisbach equation is shown below (11):

EQUATION 3-8:

$$\Delta P = \frac{64 f_f l \rho Q^2}{2D(\pi D^2)^2}$$

$$\Rightarrow Q = \sqrt{\frac{\Delta P \cdot 2\pi^2 D^5}{64 f_f l \rho}}$$

Equation 3-8 shows that the flow rate is highly dependent to a change in the diameter of the pipe. A reduction in the pipe diameter will severely reduce the flow rate. Gases may be modelled as incompressible if the relative change in density is less than 2%(10).

The change in the density with the change in pressure of the fluid being analysed needs to be taken into account when the fluid cannot be assumed to be incompressible. Depending on the assumption of how the to treat the velocity of the fluid two different equations for compressible flow can be developed. If the change in the fluid velocity due the density change is ignored Equation 3-9(11) is found from combining the continuity equation and equations of state. Equation 3-9 is for isothermal flow. The isothermal assumption is made when it is reasonable to assume that any gain in internal energy of the fluid is lost rapidly, leaving the fluid temperature constant(11).

EQUATION 3-9:

$$v_1 = \sqrt{\frac{(P_1^2 - P_2^2) \cdot \frac{D}{4} RT}{f_f P_1^2 l}}$$

A more complete version of this equation is shown in Equation 3-10 (10). Notice that Equation 3-10 uses a different friction factor to the equations shown before. This is the Darcy friction factor, f_d, and is mainly used by American texts (11). It is four times greater than the Fanning factor, f_f, used before. Either friction factor may be used in both equations as long as the multiple of 4 is accounted for.

EQUATION 3-10:

$$\frac{P_1^2 - P_2^2}{2P_1} = \frac{f_d l \rho_1}{D} \times \frac{v_1^2}{2} \times \frac{T_1 + T_2}{2T_1}$$

Equation 3-10 is not limited to isothermal cases. The final term on the right hand side accounts for linear changes in temperature along the length of the pipe. From the principle of the conservation of mass it follows that the mass flow rate must stay constant along the length of the pipe. So for a pipe with a constant cross sectional area an increase in the density of the compressible fluid will decrease the fluid velocity keeping the mass flow rate constant(11).

All aforementioned calculations solve for the flow through a pipe of constant diameter, this means that any component fitted in the line have to be accounted for using the equivalent length method or a similar approach. When it is necessary to model the flow rate through a valve with varying pressures on one or both sides of the valve the sonic conductance method is useful.

By specifying four parameters the valve's flow rate can be completely described. The sonic conductance gives the maximum flow rate for a given supply pressure while the critical pressure ratio accounts for a drop in flow rate as the delivery pressure rises.

Adding the valve transients for the opening and closing of the valve to the model allows the effects of the events to be accounted for in the simulation. The times are measured from when the event signal is initialised to when the valve is fully open or closed. Flow through the main ports of a two stage valve is only initiated in about the last 10% of the transient time as the time taken to energise the solenoid and activate the pilot air which moves the main spool(8).

EQUATION 3-11:

$$\dot{m} = \begin{cases} P_1 C \rho_0 \sqrt{\frac{T_0}{T_1}} \sqrt{1 - \left(\frac{\frac{P_2}{P_1} - b}{1 - b} \right)^2} & for\ \frac{P_2}{P_1} > b\ (subsonic\ flow) \\ P_1 C \rho_0 \sqrt{\frac{T_0}{T_1}} & for\ \frac{P_2}{P_1} < b\ (choked\ flow) \end{cases}$$

Where: The zero subscript designates the ISO 6358 standard conditions

b is the critical ratio.

Equation 3-11(8) shows the relationship used to find the mass flow through a valve using the sonic conductance method. If the mass flow rate through a valve is plotted against the pressure ratio across the valve a curve similar to the one shown in Figure 3-3 is found.

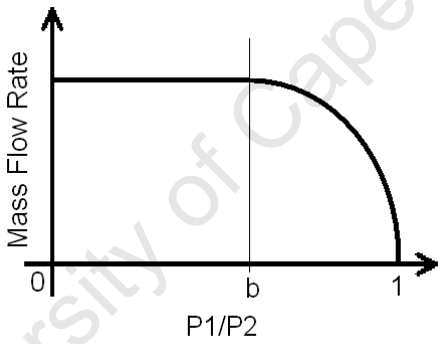

FIGURE 3-3: TYPICAL PLOT OF MASS FLOW RATE VS PRESSURE RATIO FOR THE SONIC CONDUCTANCE MODEL

Figure 3-3 shows how a maximum mass flow rate is reached when the pressure ratio is less than the critical pressure ratio. This region is called choked flow(8). The critical pressure ratio is a function of the supply pressure and is not dependent on the delivery pressure. As the delivery pressure increases, increasing the pressure ratio above the critical value, the mass flow rate decreases. The profile of the curve is modelled as an ellipse described by the subsonic flow part of Equation 3-11. This region is known as subsonic flow(8).

Modelling errors have been shown to be minimal when using this method. When compared to theoretical fluid mechanics equations the errors were found to be below 0.33%(8). Comparing the model to measured data the error was found to increase as the pressure

ratio neared unity. A method to correct this by adding a laminar flow region is suggested by Beater(8) and is incorporated by his model discussed in section 3.2.1.

The values of sonic conductance, C, and the critical pressure ratio, b, are valve dependent and are normally available from the valve manufacturer. Methods for determining the coefficients are detailed in the standard ISO 6358(8). The standard also states the reference conditions as shown in Table 3-3(8).

TABLE 3-3: TABLE OF ISO 6358 STANDARD CONDITIONS

Temperature	T_o	293.15 K
Pressure	P_o	100kPa
Gas Constant	R_o	288 J/(kg·K)
Relative Humidity	-	65%
Density	ρ_o	1.185 kg/m³

3.2 PNEUMATIC SYSTEM MODELS

In pneumatic systems in which events happen very quickly a cylinder chamber might never settle at a constant pressure. To predict values like the speed and acceleration of the piston and its load, a numerical simulation of how the flows and pressures change with time need to be programmed. Even the time that a valve takes to open fully can affect the predictions(8). These models are typically discretised in time and the variables are numerically evaluated at time steps throughout the event.

3.2.1 BEATER MODEL

In his book, *Pneumatic Drives*, Beater(8) proposes a model based on the conservation of mass and energy. The mass flow rate between components is determined by using the sonic conductance of the valve separating them, which was explained in section 3.1.4. By making some assumptions and using the conservation of energy, the temperature of the air in a chamber with a changing volume and a mass of air can be calculated. As pressure is the only state variable of the air not accounted for this can be found using the ideal gas equation, discussed in section 3.1.1.

To be able to apply the Beater model the air in a volume is treated as a continuum. This means that the pressure, density and velocity of the gas are assumed constant across the volume, ignoring the fluid dynamics occurring within each volume of interest(8). The volume and mass of the gas are found from the cylinder position and mass flow rate. After which the ideal gas law to be applied to entire volume of interest to calculate the gas pressure. It is also assumed that the air utilised in the system has been adequately filtered and dried, meaning that no condensation can cause an unexpected deviation of the physical gas state from the gas law predictions(8).

As mentioned before gases in a state far from their critical point can be treated as ideal gases(9), Beater calculated the relative error of the density predicted by the ideal gas equation to tabulated data from a thermodynamic reference to show the effectiveness of the ideal gas equation. His results over the region applicable to pneumatic drives ($200\ K < T < 800\ K$; $1\ bar < P < 100\ bar$) showed a maximum error of 5%(8).

By tracking the mass in each chamber and mass flow rate in and out of them of it is not necessary to relate the state that the gas was in to its new state when analysing a flow. From the principle of the conservation of mass, the mass of a certain amount of the air is independent of its state(9). In the interest of computational ease the Beater model monitors the mass of air in each chamber of interest and the mass flow in or out of these chambers.

Directional Control Valves

Four constants are needed to model a directional control valve using the Beater model: the sonic conductance, critical pressure and the open and closing transients of the valve. These values can be found experimentally or sourced from the manufacturer(8).

Once the sonic conductance and critical pressure ratio of a valve or restriction are known the mass flow rate through the fully open component can be predicted by using the calculation shown inEquation 3-11. Beater suggests modifying Equation 3-11 to avoid a numerical spike in the flow rate to include a laminar flow region. The modified model is shown in Equation 3-12.

EQUATION 3-12:

$$\dot{m} = \begin{cases} 1000C\rho_0 \sqrt{1 - \left(\frac{0.999 - b}{1 - b}\right)^2} \cdot P_1 \left(1 - \frac{P_2}{P_1}\right) \sqrt{\frac{T_0}{T_1}} & for\ \frac{P_2}{P_1} \geq 0.999\ (laminar) \\ P_1 C\rho_0 \sqrt{\frac{T_0}{T_1}} \sqrt{1 - \left(\frac{\frac{P_2}{P_1} - b}{1 - b}\right)^2} & for\ 0.999 > \frac{P_2}{P_1} > b\ (subsonic) \\ P_1 C\rho_0 \sqrt{\frac{T_0}{T_1}} & for\ \frac{P_2}{P_1} < b\ (choked) \end{cases}$$

The mass flow rate represents the rate at which the gas moves between the chambers connected by the valve; moving from a high pressure region to a low pressure region. By using the duration of the time step used in the dicretisation, the mass of gas that moved during the time step can be found. The mass of the gas in the chamber can be adjusted using this value.

Modelling the valve transient is slightly more complicated, as the events which occur within the valve are not easily measurable. A detailed model of the entire valve can be created which, incorporates the input current as in the physical case and then simulates each event from the energising of the coil to the movement of the main stage spool. This approach results in needing to measure many more constants which are not available in regular datasheets(8), complicating the model.

A simpler approach is used by Beater, who analysed the flow rate through a valve as the control signal is changed. In a typical two stage solenoid valve the gas only starts to flow during the last 10% of the opening transient(8).

Pneumatic Cylinders

In the case of a fast moving double acting pneumatic cylinder the state of the gas on either side on the piston needs to be analysed. As the cylinder extends the volume of the front decreases at such a rate that the pressure in the chamber can build up and retard the movement of the cylinder.

The force provided by the cylinder is found by comparing the forces created by the pressures on either side on the piston. To calculate the pressures the temperature, volume and mass of the gas in the chamber need to be known.

From the principle of the conservation of energy the temperature can be predicted by accounting for energy lost due to: air leaving the chamber, the change in volume, and heat transfer to the cylinder material and energy gain from air entering the chamber.

EQUATION 3-13:

$$\frac{d}{dt}U = \dot{m} \cdot c_v \cdot T + m \cdot c_v \cdot \dot{T}$$

EQUATION 3-14:

$$\frac{d}{dt}U = c_p \cdot T_{in} \cdot \dot{m}_{in} - c_p \cdot T \cdot \dot{m}_{out} - P \cdot \dot{V} - h \cdot A_{cyl} \cdot \Delta T$$

EQUATION 3-15:

$$\dot{m} \cdot T + m \cdot \dot{T} = \gamma \cdot T_{in} \cdot \dot{m}_{in} - \gamma \cdot T \cdot \dot{m}_{out} - \frac{P \cdot A_{bore} \cdot v}{c_v} - \frac{h \cdot A_{cyl} \cdot \Delta T}{c_v}$$

Where T_{in} is the temperature of the incoming mass flow

T is the temperature of the gas inside the control volume

ΔT is the difference in temperature between the gas and the cylinder casing

A_{bore} is the bore area of the cylinder

A_{cyl} is the area of the casing exposed to the gas in the chamber

h is the heat transfer coefficient between the gas and the casing

γ is the ratio of the specific heat capacities (C_p/C_v)

By combining Equation 3-13(8) and Equation 3-14(8), Equation 3-15(8) is derived. Equation 3-13 is derived from the fact that the internal energy of a gas is equal to the product of the mass of the gas, its specific heat and the temperature of the gas. The time derivative of this gives Equation 3-13.

Equation 3-14 is the result of analysing the possible gains and losses of internal energy. Factors that are accounted for are the introduction of energy with mass flow into the cylinder, the loss of energy to mass flow out of the cylinder, the loss of energy due to an increase of volume and lastly a loss of energy to heat convection from the gas to the cylinder casing(8). Potential and kinetic energy contributions of the air have been ignored as they were found to be negligible(8)(14).

From Equation 3-15 the value of time derivative of the temperature can be found. This can be assumed constant over the time step, provided that the duration is short enough, and

the actual temperature change can be calculated. The heat transfer coefficient, *h*, has units $\frac{W}{m^2 \cdot K}$ and describes the heat transfer rate between the cylinder casing and the air inside it. In cases where the event is over in less than two seconds the system can be assumed to be adiabatic(15), making the value of *h* zero. A very large value of *h* would effectively make the simulation isothermal(8).

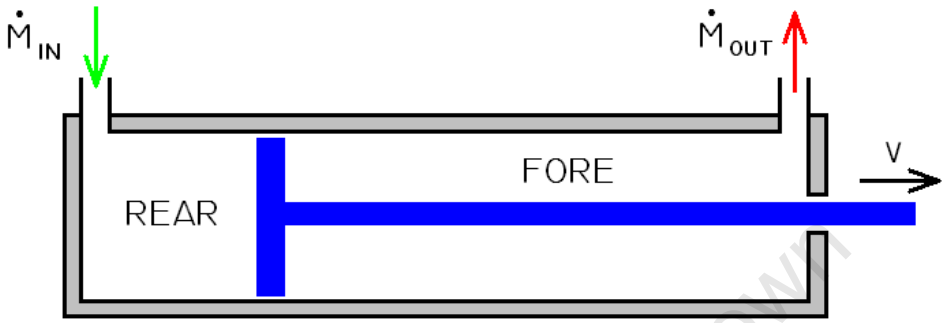

FIGURE 3-4: A LABELLED SCHEMATIC OF A CYLINDER

Calculating the volumes of the chambers is done by adding the contributions of their respective dead volumes to the current working volume of each chamber. Hence by knowing the dead volumes of both the cylinder's chambers, its stroke, the width of the piston and its position both chamber volumes can be calculated. As the model is implemented in a time discretised simulation the position of piston is known at the end of each time step and can used to find the volumes for the beginning of the next step.

The dead volumes of cylinder are widely varied and are not normally part of the datasheet information(8). To accurately model the cylinder this volume needs to be measured in some way or obtained from the manufacturer.

As the mass of the gas in each chamber is tracked by monitoring the mass flow in or out of them, the mass at the end of each time step is known. Using the Ideal Gas equation, Equation 3-1, the pressures in both the chambers can now be found.

To predict the force that the cylinder will provide the forces on either side of the piston need to be found using the relevant pressures and areas. Any retarding forces or damping can also be included to improve the prediction. The most common of these is friction between the piston seals and the inner surface of the cylinder casing(8).

Using Newton's II Law, the acceleration of the piston over the time step can be found. By lumping the mass of the piston, rod and load being moved and assuming that acceleration is constant over the period of the time step allows the velocity at the end of the step to be calculated and thus the displacement over it as well. Equation 3-16(8) shows how the time derivative of velocity, the acceleration, is calculated.

EQUATION 3-16:

$$\dot{v} = a = \frac{P_{rear}A_{bore} - P_{fore}A_{annulus} - F}{m_{lumped}}$$

All the parameters necessary to analyse the response of the cylinder to a range of different excitation pressures and flow rates are attainable by using the model described above. These include the state of the gas in both chambers and the dynamics of the piston and load.

3.2.2 MARE MODEL

Mare et al published a paper(14) detailing an improved dynamic model for pneumatic actuators. The study was primarily aimed at the modelling of pneumatic jacks, which consist of a directional control valve and double acting, double rod actuator(14). The piston velocities in these applications are only a few metres per second(14).

A more strict mathematical approach towards the conservation laws is taken in this study, arriving at similar conclusions to the Beater model. An investigation into compressible flow through an orifice yields a relation which does not account for the geometry of the orifice(14). The geometry considerations are what create the critical pressure ratio and the reduction in flow at subsonic flows(14). Mare settles on the use of the ISO 6358 standard, the sonic conductance method described in section 3.1.4.

Three conservation laws are applied to the control volumes, the conservation of mass, energy and momentum. As the kinetic energy of the gas is ignored by Mare the conservation of energy results in the same relation as shown by the Beater. Conservation of mass simply states that the change in mass of gas inside the control volume is the difference between the mass flows in and out of the volume(14).

EQUATION 3-17:

$$\dot{m} = \dot{m}_{in} - \dot{m}_{out}$$

Using the conservation of momentum the average velocity of the gas in the volume can be related to the flow velocities of the entering and leaving gas(14). But as the kinetic energy has been deemed negligible this serves no purpose in this model(14). For completeness the relation is shown in Equation 3-18(14) below.

EQUATION 3-18:

$$m\dot{v} + v\dot{m} = \frac{d}{dt}\int_V \rho v \, dV + v_{in}\dot{m}_{in} - v_{out}\dot{m}_{out}$$

Model Validation

Mare validates his model using an instrumented cylinder. A LVDT is used to calculate the piston position while high response strain gauges record the pressures in the chambers(14). Comparisons of the simulated and actual results for the piston position and velocity showed good correlation between the two. The simulated and actual cylinders were ordered to extend, retract, extend again and finally retract at the same time intervals. From Figure 3-5 it can be seen that the simulation tracked the variations closely with only local deviations from the measured values(14).

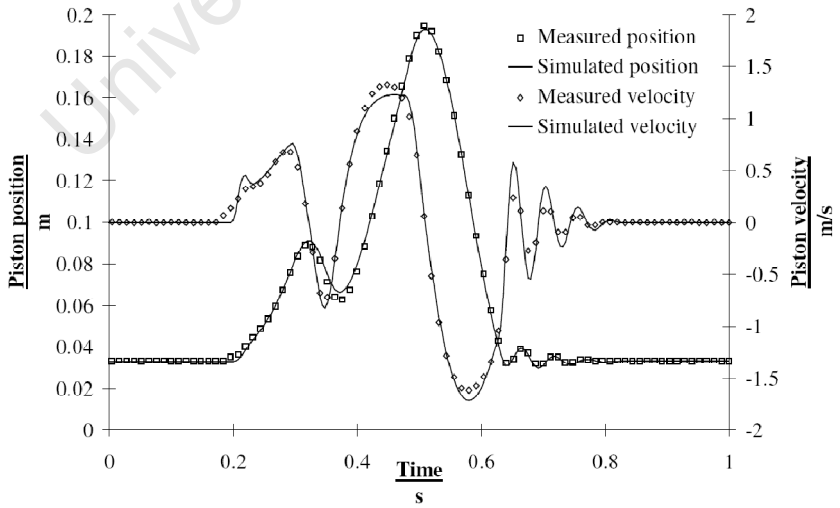

FIGURE 3-5: PLOT OF SIMULATED AND ACTUAL PISTON DISPLACEMENTS AND VELOCITIES(14)

Simulations using adiabatic and isothermal assumptions were also performed to highlight the effectiveness of the inclusion of convection heat transfer between the gas and the cylinder casing. A plot, shown in Figure 3-7, of the error between the simulations' values and the measured readings were used to compare the chamber pressures to the experimental results. The pressure history inside the chamber is plotted in Figure 3-6 showing the rise and fall of the chamber pressure.

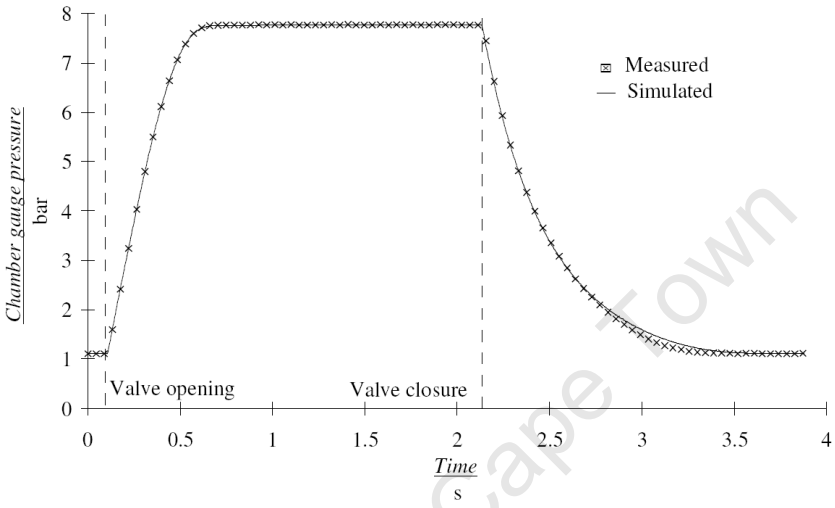

FIGURE 3-6: PLOT OF CHAMBER PRESSURE TIME HISTORY FOR VALIDATION TEST(14)

All the simulations performed well while the chamber was at constant pressure. Both the adiabatic and isothermal simulations deviated during the charging stage of the experiment. During the charging stage, the Mare model's error was very small. After the valve is closed it was slightly larger but still much smaller than either of the other simulations. Both the adiabatic and isothermal simulations underestimate the chamber pressure as it decreases back to the atmospheric pressure, the adiabatic simulation more so than the isothermal one.

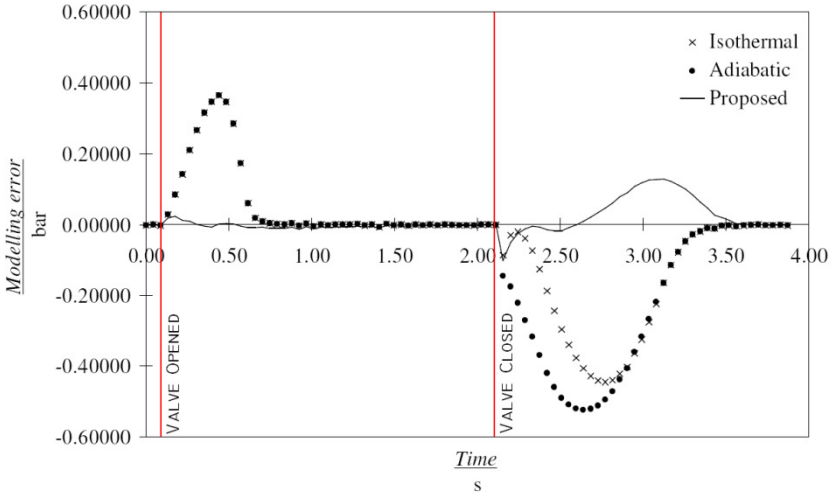

FIGURE 3-7: PLOT OF DIFFERENCE BETWEEN THE SIMULATED AND EXPERIMENTAL RESULTS(14)

Comparisons of the results using a mean relative error, shown in Equation 3-19(14), are tabulated in Table 3-4. This also highlights the effectiveness of the addition of the convection temperature model.

EQUATION 3-19:

$$\varepsilon = \sqrt{\frac{\sum_{data}(P_{measured} - P_{simulated})^2}{\sum_{data} P_{simulated}^2}}$$

TABLE 3-4: TABLE OF SIMULATION ERRORS

		Adiabatic	Isothermal	Mare
Charging	**Min**	0.94	0.94	0.95
	Max	2.82	2.82	1.22
Discharging	**Min**	6.10	4.64	1.14
	Max	13.08	8.87	2.01

3.3 FRICTION MODELS

To model and control mechanical systems the forces on the components of these systems need to be analysed. Various frictional forces act on all moving components of a system. While some are very small and can be neglected in modelling calculations others need to be quantified and taken into account when resolving forces on the components.

The classical friction models that are taught in elementary physics courses greatly simplify the phenomena that cause friction forces to occur. Depending on the application these models can suffice. More complicated models are continually being developed, which take into account varying degrees of the phenomena (16).

Adding lubrication to a contact area increases the number of phenomena that are involved in causing the friction forces to occur. Depending on the velocity, the extent of the lubrication varies as does the magnitude of the lubrication's shear strength(16).

In a situation where two dry surfaces are in contact the friction can be adequately described by a friction coefficient related to the materials of the two surfaces. It can be shown that the coefficient is not dependent on normal load or the relative velocities but of the shear strength of the surfaces(16). Typically in simple cases of dry contact the friction can be modelled using only Static and Coulomb frictions, shown in Figure 3-8.

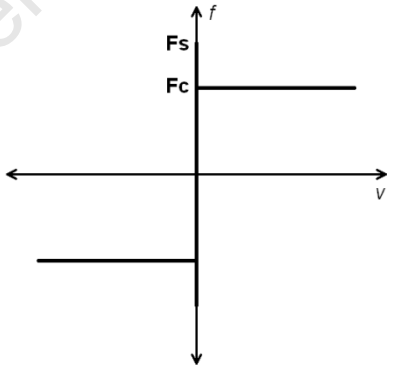

FIGURE 3-8: CLASSIC FRICTION MODEL SHOWING STATIC AND COULOMB FRICTION

For there to be any relative motion between the surfaces the Static friction (Fs), also known as the Break Away friction, must be overcome by the external forces. After relative movement of the two objects has been initiated the frictional force drops to the Coulomb

friction value (Fc). Both the Static and Coulomb frictions are constant for a given contact pair.

Two other components which make up the friction model are Viscous and Stribeck frictions. Viscous friction describes the change in the frictional force with velocity. Typically viscous friction is modelled as a linear relationship between frictional force and the relative velocity of the surfaces. Experimental data can often be better fitted by using a nonlinear relationship(16).

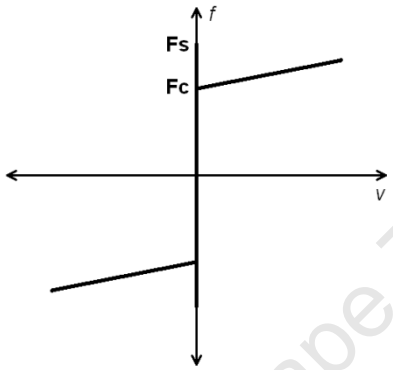

FIGURE 3-9: FRICTION MODEL SHOWING STATIC, COULOMB AND VISCOUS FRICTION

Viscous friction occurs in lubricated contacts and is due to a combination of shear strength of the lubricant and the hydrodynamic effects created by the relative velocity. Generally the shear strength of lubricants decreases with an increase in velocity which would suggest a decrease in frictional forces(16). The Stribeck effect causes an increase in the frictional force with velocity. This is where the hydrodynamic effects in the fluid film become more significant than the reduction in shear strength increasing the frictional force between the surfaces(16). For the Stribeck effect to take effect the thickness of the film needs to be sufficient to completely separate the surfaces.

Physically the transition from the Static friction state is not discontinuous as shown in Figure 3-9 but drops smoothly to the Coulomb friction value. This transitional friction is called Stribeck friction and is often modelled using an exponentially decaying function(16). In a lubricated contact the two surfaces are initially in contact, as the velocity increases the film begins to be built up separating the surfaces until both surfaces are only in contact with the fluid. Viscous friction then takes over. Figure 3-10 shows how the Stribeck curve smoothes the transition between Static and Viscous friction. The domain over which the Stribeck

friction acts is small and very close to zero velocity. This makes its inclusion in control algorithms where low velocities are concerned important(17). Controlling an object where the velocity passes through zero velocity requires the system to anticipate the abrupt change in frictional force when nearing zero velocity(17).

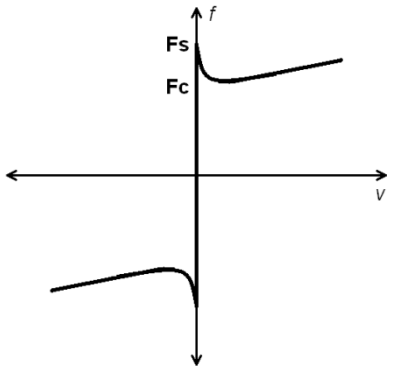

FIGURE 3-10: FRICTION MODEL INCLUDING STRIBECK FRICTION

The classical models discussed so far apart from the Stribeck transitional model do not take into account the hydrodynamic effects of the lubricant. Dynamic models which account for some of these effects do exist. Their development has been driven by the necessity in high precision control for more accurate friction compensation.

Constructing a generalised model from first principles to account all the different phenomena has been deemed impossible(16). Instead models have been developed which approximate the friction in certain applications. Investigations into the effects of increasing or decreasing velocity(18)(19), the rate of the external loading(20)(21) show how frictional forces are effected by many aspects not considered by the classical models.

Johannes et al. showed that the breakaway force and hence the Static friction coefficient are decreased with an increase in the application rate of the external force(20). This was confirmed by Richardson et al(21). A hysteresis effect where the friction at a certain velocity is greater while the relative acceleration is positive compared to where the acceleration is negative was found by both(18) and(19).

Dynamic friction models range in complexity including more effects of the different phenomena as complexity increases. The Dahl Model which was originally developed to describe friction in ball bearing applications(16) is a relatively simple model which captures

the hysteresis but not the breakaway friction or the Stribeck effect. The model describes friction as being only displacement dependent and is based on the stress-strain curve concept from solid mechanics(16). Bilman and Sorine extended the Dahl Model to have a velocity dependent term but it fails to describe the true Stribeck effect(16).

Another approach is to model the asperity contacts as bristles with a spring constant. The LuGre Model(22) is an extension of this approach. The bristles act as springs, once the deflection is sufficiently large the springs start to slip. The model is a function of the separation and the relative velocity of the surfaces allowing the rate dependent phenomena to be described.

None of the models mentioned above model all friction behaviour perfectly and the model which meets the best compromise of computational efficiency and accuracy for the given application should be implemented. In the case of the acceleration stage model a combination of a Coulomb fiction value and a Stribeck curve, created from data received from FESTO is used.

4 MODELLING OF SYSTEM DYNAMICS

4.1 INTRODUCTION

A computational model of the pneumatic acceleration stage was written to predict the velocity profile of the sled during this stage. The suppliers of the cylinder, FESTO, had run simulations and provided BISRU with plots of the results. As these were of preliminary simulations they did not provide a comprehensive prediction. They were only performed for isolated cases and details such as the friction between the sled and the rails had not been accounted for.

Apart from constants which describe the specifications of the cylinder, input variables describing the test conditions of the particular test being simulated need to be taken into account. Input variables consist of the mass of: the sled and its payload; the number of acceleration valves opened during the test and the pressure of the air in the storage vessel. These variables make up the "recipe" which results in a particular sled velocity. Also of importance is the acceleration of the sled to its final velocity. This is due to the fact that it has an effect on the loading experienced by the sled during the acceleration stage and the securing of the test specimen.

Test data will be collected from the test specimen, during the deceleration stage of the run, making this the key focus area. MOOG supplied BISRU with a computational simulation of the deceleration cylinder and its control system. The mass of the sled and its payload, the desired set point pressure, the contact velocity and the control parameters are the input parameters required for this simulation for each particular test. Apart from the set point pressure, these input variables are dependent on the results of the acceleration stage simulation. For this reason the models were linked.

By linking the models, the input variables for a particular test are entered once via a common interface. When this code is run the variables are set and the different simulations are performed in the correct order while passing on the necessary information. The pertinent data from both simulations is reported by plotting the results and creating a text file containing both the velocity and force histories. These results can then be used in the analysis of the system's behaviour.

4.2 DEVELOPMENT OF THE ACCELERATION STAGE MODEL

The initial attempt of creating at simulation of the acceleration stage was implemented in MatLab using a time discretised approach. After a number of revisions the final model was achieved. Some of the elements that were revised and included during the process were the prediction of the flow rate into and out of the chambers, the method used to determine the cylinder friction, the dead volumes of the different chambers and the thermodynamic assumptions made over the system.

Revision I:

Initially the nominal flow rate of the valve quoted in the manufacturer's datasheet was used to describe the flow rate through the valves. An isothermal assumption was used for simplicity and because Douglas(11) reported that any increase in temperature can be assumed to be lost through pipe walls of copper piping.

A viscous frictional term was used to describe the cylinder friction, while simple Coulomb friction was used for the rail friction. To account for the inertia of the system the masses of the piston, rod, sled and its payload were lumped and treated as one large mass with a centre of mass at the same position as the piston. Once the sled had been released the mass was reduced to that of just the rod and piston. The sled was assumed to have been released as the cushioning air was activated.

As the diameters of the bore and piston rod were known the cross sectional areas of both chambers could be calculated. From the piston's position the volumes of the two chambers could be found using their respective areas.

The dynamics of the cylinder were tracked by resolving the force created by the pressures in the cylinder chambers, the rail and cylinder frictions. The acceleration was found using Newton's second law. The assumption that the acceleration is constant over each time step allowed the velocity at the end of the step to be calculated and thus the piston position.

An isothermal assumption had been made which meant that the chamber pressures could be predicted using Boyles Law.

The result of this simulation was an over estimation of the pressures in the chambers. Possible causes were the use of the nominal flow rate and the initial volume of the rear chamber being zero.

Revision II:

To try to solve the problem encountered in the initial model various improvements were made to the model as follows. A compressible flow relation replaced the manufacturer's nominal flow rate value. The initial volume of the rear chamber was increased by altering the initial position of the piston.

The resistance created by the valves was estimated from typical discharge coefficients found in *Fluid Mechanics*(11). An equivalent lengths method was used to account for the separation losses as well as the pipe friction of the system. Once the equivalent length of the system was known the flow velocity could be calculated using the compressible flow equation, shown in Equation 3-10, ignoring the temperature term because of the isothermal assumption. The modified equation is shown below in Equation 4-1.

EQUATION 4-1:

$$\frac{P_1^2 - P_2^2}{2P_1} = \frac{f_d l \rho_1}{D} \times \frac{v_1^2}{2}$$

$$v_1 = \sqrt{\frac{P_1^2 - P_2^2}{P_1} \times \frac{D}{f_d l \rho_1}}$$

Before the compressible flow equation was chosen an investigation into the difference between flow rate predicted by the incompressible Darcy equation and the compressible flow equation was performed. Two comparisons were run: one where the pressure difference across a pipe was 1 bar and another where the difference was 6 bar. While there was only a 2.6% change in flow rate for the 1 bar experiment; in the 6 bar experiment there was a 20% deviation. This warranted the use of the more complicated compressible relation.

To implement the compressible flow relation, shown in Equation 4-1, a friction factor needed to be calculated. As the friction factor is dependent on the Reynolds number a

subroutine was programmed to calculate the factor during every time step using the Colebrook-White equation, Equation 3-6. The model was kept isothermal.

While improving the results there was still a discontinuity in the pressure as the cushioning air was activated. It was also noticed that when the pressure in a chamber reached the supply pressure the model became unstable.

Revision III:

The instability of the model was addressed. A varying flow rate similar to the one used to model the flow into the rear chamber was applied to the flow of the cushioning air into the front chamber. The curves then started to become more reasonable as they were continuous and the magnitudes of the chamber pressures and piston velocities were realistic.

It was noticed that the chamber pressures did not reduce if they increased above the supply pressure. To solve this; code was added to assess if the chamber pressure was higher than the supply pressure, in which case the flow would change direction and leave the chamber.

Apart from a few minor details and effects mentioned above, the Mk III version of the model worked reasonably well.

Revision IV:

As the duration of the entire event was so short, the effects of the valve transient were thought to be of importance. Code was added to throttle the flow over the opening and closing periods of the valves. Values of the opening and closing transients were taken from the manufacturer's datasheet (which was later found to be incorrect). The factor was varied exponentially over the transient times.

Another contribution to the instability of the model was found to be the reduction of one of the chamber volumes to zero. This happened as the piston moved to the end of the cylinder. In reality the volume would never become zero as the ports and recesses in the end caps create a dead volume between the piston face and the valve. To account for this, dead volumes were added to both chambers. This was achieved by adding an addition

volume to the existing volume calculation to ensure that the volume did not drop below the dead volume value regardless of the piston position.

The sizes of the dead volumes were calculated from the engineering drawing of the end caps and the piston. The areas of the cavities, which created the dead volumes, were calculated using simplified geometry and the volumes found by multiplying the areas by their arc lengths.

Doubts about the validity of the isothermal assumption were addressed. Instabilities highlighted the briefness of the event and the importance of small but significant detail like the valve transients. The extremely short period of the event meant that there was very little time for any heat dissipation to occur; meaning Douglas' reasoning for his isothermal assumption did not apply. A decision to use polymer piping meant that the heat transfer between the compressed air and atmosphere would be reduced even further. These observations suggested that a temperature dependent simulation with either a heat transfer consideration or adiabatic assumption would be more suitable.

A simple adiabatic orifice model was found and investigated(11). It was found that the model could be used to predict the flow, but the valve characteristics would have to be estimated. It was also noted that the simulation would have be modified to account for varying temperature.

Another consequence of the use of polymer piping was the removal of pipe friction. Due to the smoothness of the piping, friction losses over networks of reasonable length can be ignored. The absolute roughness of plastic or PVC piping is taken as zero compared to that of copper at 1.5 µm.

The releasing of the sled was also revisited. Up to this point the sled was assumed to have been released as the cushioning air was activated. Practically there would be a delay between the activation of the cushioning air and a reduction in the piston velocity. The code was adapted so that the sled was released when a reduction in velocity had been predicted. By monitoring the difference in velocity of the current and previous steps the simulation could predict more accurately when the sled would be released.

Additional code was written to provide tabular data of the velocity profile of the acceleration stage. The data was saved to a text file to allow the profile to be easily stored and transferred to the finite element model.

Revision V:

The results produced by FESTO from their simulations could at this stage be reproduced by the acceleration stage model. Problems lay in the fact that although the result could be reproduced the actual cylinder friction and varying flow rate of the valves were not known. By varying the resistance of the valve to the flow and the value of the friction between the piston and the inside of the cylinder; a wide range of solutions were possible. The actual values of these parameters needed to be found.

Without the use of specialised equipment, which was not available at BISRU, experimentally determining either of these values would have been unreliable. After contacting the manufacturer, FESTO, the sonic conductance, critical pressure ratio and transient times of the MFH-3-3/4-S solenoid were obtained. As well as a plot of the cylinder's frictional force with piston speed. Table 4-1 shows the values for the solenoid valve and Figure 4-1 shows the plot of the cylinder friction received from FESTO.

TABLE 4-1: VALVE PROPERTIES FOR THE FESTO MHF-3-3/4-S SOLENOID VALVE(15)

Valve Property		Value	Unit
Sonic Conductance	C	32	l/(bar s)
Critical Pressure Ratio	b	0.35	-
Open Transient		29	ms
Closing Transient		40	ms

After receiving the valve properties from the manufacturer, a flow model which incorporated sonic conductance and critical pressure ratio was found. This method is the basis of the ISO 6358 standard for pneumatic fluid power(8). The model is an adaption of choked flow through converging nozzles for valves with lower critical pressure ratios(8). The properties received also highlighted an error in the datasheet; the values of the opening and closing transients had been mistakenly swapped as mentioned in MkIV. This was confirmed by a FESTO representative(15).

The flow model that was found was part of the Beater model(8) described in section 3.2.1., using this model meant that simulated flow was calibrated from experimental investigations carried out by valve manufacturers. Apart from the sonic conductance of the valve and critical pressure ratio, mass flow was dependent on the temperature and pressure of supply air as well as the delivery air pressure. The combination of the flow model and the property constants allowed a reliable simulation of the mass flow to be achieved.

An attempt was made to incorporate the new flow model into the existing code but it was decided that recoding the simulation from scratch would lead to a more efficient and understandable code. The main reasons for this were: that the isothermal assumption was deeply ingrained into the original code; and that the accumulation of all the modifications mentioned above had disorganised the program.

A new code was therefore written. A few other ideas gained from Beater's model(8) were included into the creation of the simulation. While many of the methods used by Beater were similar to ones used in the original model, his temperature model based on the conservation of internal energy and his mass tracking method were welcomed improvements.

Beater's temperature model included a heat transfer coefficient which described the heat convection between the air inside the chambers and the cylinder casing. The change in the air's temperature was proportional to the surface area of the casing, which was exposed to the air in the chamber, as well as the difference in temperature between the air in the chamber and the casing.

Setting the value of the heat transfer coefficient to zero made the simulation adiabatic(8); as no energy would be lost to the atmosphere via heat transfer. In the simulation allowances were made for the convection term by including it in the temperature models and creating a constant for the coefficient. The coefficient constant was set to zero. This was done because of the short duration of the event and slightly insulating nature of the polymer pipes. Making this assumption was supported by one of FESTO's simulation engineers. FESTO's simulators assume no losses to convection during events with a duration of under two seconds(15).

The friction profile received from FESTO also needed to be incorporated into the simulation. Figure 4-1 shows the plot received from FESTO; after which the inclusion of curve into the simulation is explained. The English translations of the German titles are given on brackets.

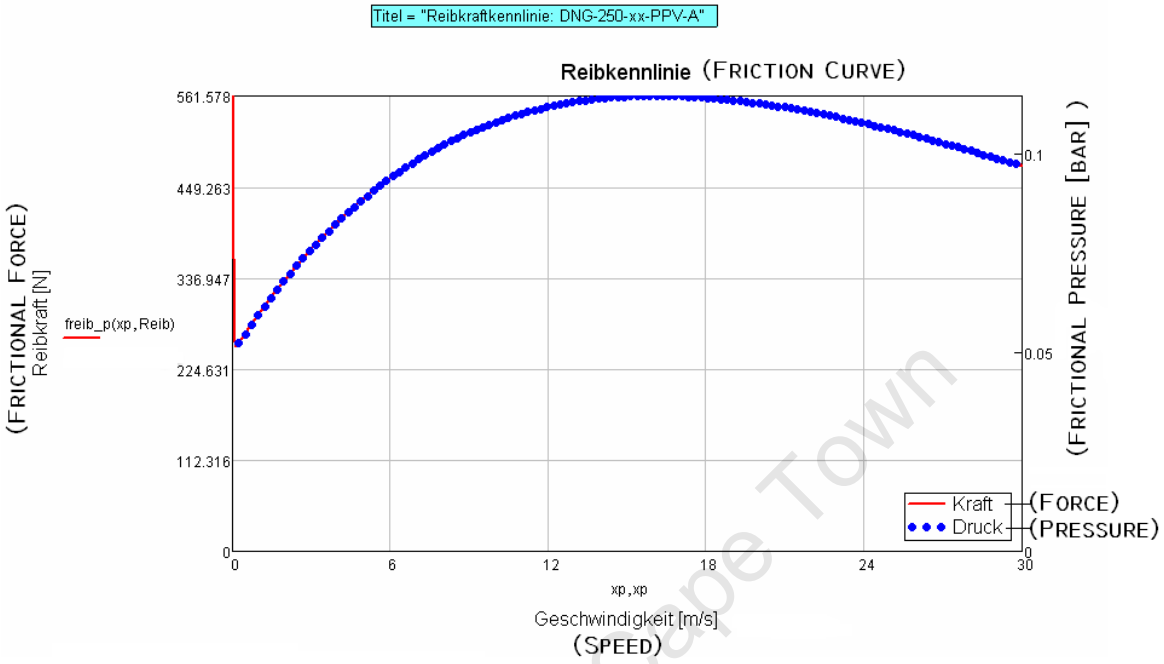

FIGURE 4-1: PLOT OF THE FRICTION BETWEEN THE PISTON AND THE CYLINDER CASING FOR FESTO'S DNG-250-PPV CYLINDER(15)

The plot was received as a graphic file so the data could not be extracted computationally from the file. The plot was enlarged and printed after which points on the graph were manually read off using a ruler and set square.

The frictional force, the red line, shows an initial spike which represents the breakaway or static friction of 561.6 N. The effect of the Stribeck friction can hardly be seen as the frictional force decreases to the Coulomb friction value of 253 N. After this the viscous friction effects of the high speed grease dominate. FESTO incorporate the frictional effect into their simulation using an effective pressure; these values are represented by the blue dots plotted on the right hand axis in bar.

When reproducing the friction relationship a static friction of 561.6 N was assumed. There was a possibility that this value could have been higher as the graph's range did not exceed 561.6 N, but as no further information was known this value was used. The Coulomb friction was read off to be 257 N. The Stribeck friction was ignored due to its negligible effect and the viscous friction curve was estimated using two quadratic functions. The

domains from zero to the maximum point at 14.44 m/s and from the maximum point to the end of the plot at 30 m/s were used. The piston velocity was not expected to reach 20 m/s so the domain over which the friction is described was adequate. The quadratic functions are shown in Equation 4-2 and plotted in Figure 4-2. The static friction was simply programmed into the code by keeping the piston velocity zero until the force had overcome the static friction value.

EQUATION 4-2:

$$F = \begin{cases} \dfrac{257 - 561.6}{14.44^2} \times (v - 14.44)^2 + 561.6 \quad for\ 0 < v \leq 14.44 \\ \dfrac{479 - 561.6}{(30 - 14.44)^2} \times (v - 14.44)^2 + 561.6 \quad for\ 14.44 < v \leq 30 \end{cases}$$

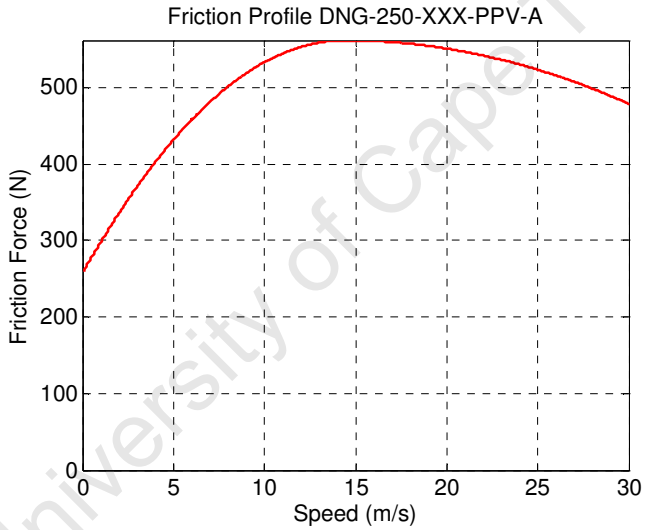

FIGURE 4-2: PLOT OF THE QUADRATIC FUNCTIONS REPRODUCING THE CYLINDER FRICTION CURVE

Values at velocities of 9 and 24 m/s were compared to values from the original plot and were found to be within 1 %. Further refinement of the curve was deemed unnecessary.

A subroutine was added to the code which calculated the friction force at each time step. The force was then incorporated into the calculation of the resultant force exerted on the lumped mass. Friction opposes motion, so the direction of the frictional force was taken to be opposite to that of the lumped mass' velocity.

Final Version:

No fundamental changes were made from the Mk V version of the simulation. After correcting a number of trivial programming errors the simulation realised satisfactory results. The plots from preliminary simulations run by FESTO were used as a benchmark. Comparisons were made between the preliminary results and the final version of the simulation. The effects of the differences between the two simulations were taken into consideration.

Factors not considered by FESTO's preliminary simulation were: the friction between the sled and the rails; the option of sealing the rear chamber once the cushioning air was fired; and the releasing of the sled once the cushioning air had taken effect.

The code could now be used to predict the acceleration stage velocity profile for any combination of test conditions. It could also be combined with MOOG's deceleration stage simulation to create an overall model.

4.3 SIMULINK MODEL OF THE DECELERATION STAGE

The designers of the deceleration system created a simulation of the deceleration stage using Simulink. Simulink is integrated into MatLab and can be used to model dynamic systems. Simulations of a system are built up using block models of subsystems. Information from each block can be fed to other blocks by connecting output and input ports of the various blocks. As the model is discretised in time the values of the different variables can be logged over the duration of the simulation and post processed in MatLab.

Included in the simulation created by Moog Controls Limited are models of the control system as well as hydraulic system. The simulation predicts the dynamics of the sled and the piston during the deceleration stage.

It was desirable to link the Deceleration and Acceleration Stage models. To achieve this, the Deceleration Stage model needed to be investigated in order to find the values that needed to be linked to the results of the Acceleration Stage.

Main Window:

The simulation is split into two main blocks: one holding the control model and the other a model of the deceleration stage equipment and the sled. Figure 4-3 shows the Graphical User Interface (GUI) from the main window of the simulation. The large block on the left holds the control system. On the right is the model of the hydraulic system and the sled.

The connectors show how signals are fed back to the controller. Readings of the distances of the sled and piston from the zero position; as well as the pressures of each of the two chambers are fed back to the controller. The block marked *Sensors* merely converts the readings to voltages. This represents the output of the physical sensors.

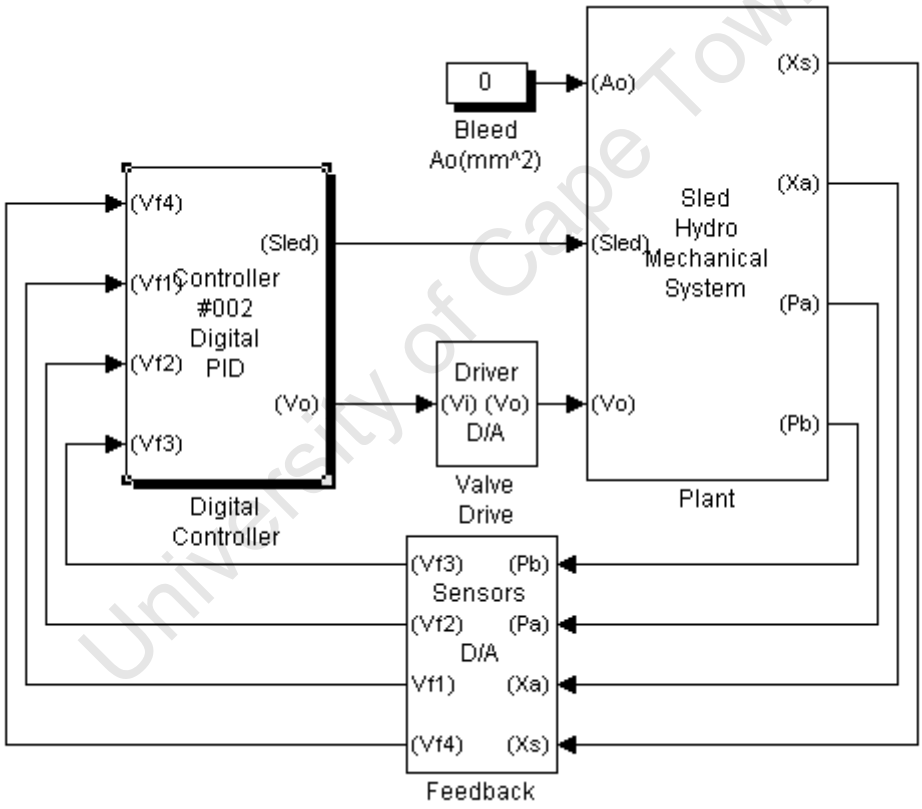

FIGURE 4-3: SCREENSHOT OF THE MAIN WINDOW OF SDS_5.MDL(23)

The value of the Bleed, A_o, represents the area of a turbulent orifice between the two chambers. This port is used for the pressure tuning of the control system when the piston is against the end stop(1).

The driver block represents the digital to analogue converter which ultimately drives the valve spool. The control system decides how to drive the valve so as to continue to achieve

the set point pressure. A signal is then sent to the valve drive which adjusts the pilot valve in such a way as to achieve the desired movement of the main spool.

4.3.1 DIGITAL CONTROLLER

The makeup of the controller unit that is shown in Figure 4-3 is displayed in Figure 4-4. The controller unit receives inputs from the sensors regarding the state of the sled and hydraulic cylinder. Depending on the prescribed set point pressure and the control parameters; the required valve drive signal is calculated. The switches highlighted in orange switch the system into manual mode. Manual mode is used for tuning of various control loops and is described in the model operation documentation(6).

Inputs to the control system which are dependent on the test conditions are: the contact velocity, set point pressure and the control parameters. The contact velocity is determined by the acceleration experienced by the sled through a combination of the pneumatic cylinder and the friction effects of the rails. While the set point pressure is chosen by the user, it is test specific because it determines the extent of the sled's deceleration. The control parameters, which were discussed in section 2.5.2, are dependent on a range of conditions including: the sled mass, set point pressure, operating point and contact velocity.

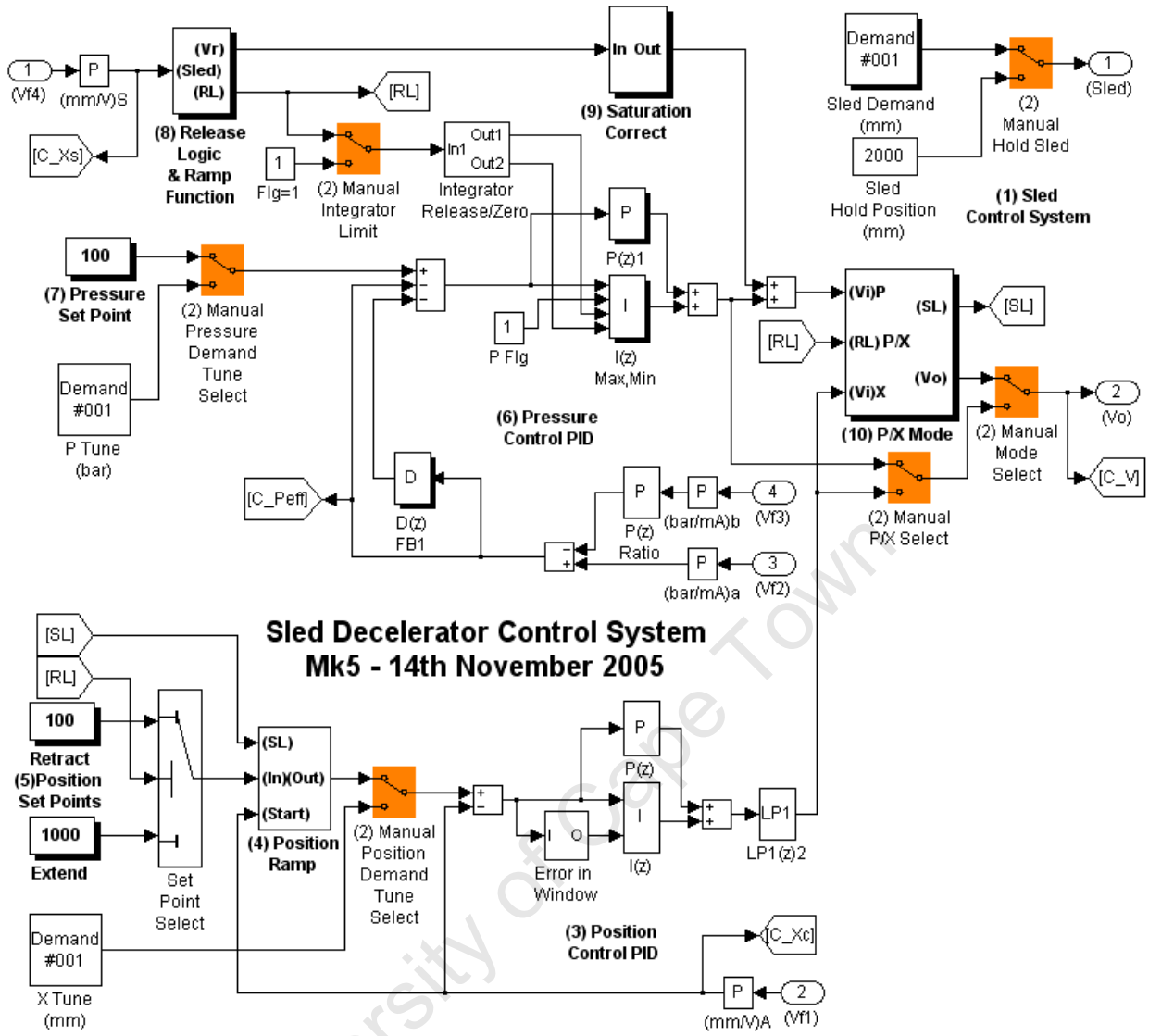

FIGURE 4-4: SCREENSHOT OF THE CONTROLLER UNIT WINDOW(23)

(1) Sled Demand:

The output from the controller unit marked *Sled*, in the top right hand corner, is an artificially created position profile of the sled. In the actual system this is a signal from the sled's position sensor.

Depending on the position of the switch marked *Manual Hold Sled*, the sled is either held at a position of 2000 mm from the zero position or moved along the profile described by the *Sled Demand*. Essentially the *Sled Demand* produces a profile of the sled position by creating a square wave with a falling edge which has a gradient equal to the contact velocity of the

sled. As velocity is the derivative of displacement, the position profile correlates to that of the sled moving at the prescribed contact velocity.

The wave generator used in the *Sled Demand* is controlled by four variables. These are amplitude, offset, frequency and rate. Figure 4-5 shows the input dialog for creating the Sled Demand. The default offset was set to 1000 mm. This represented the operating point of the cylinder.

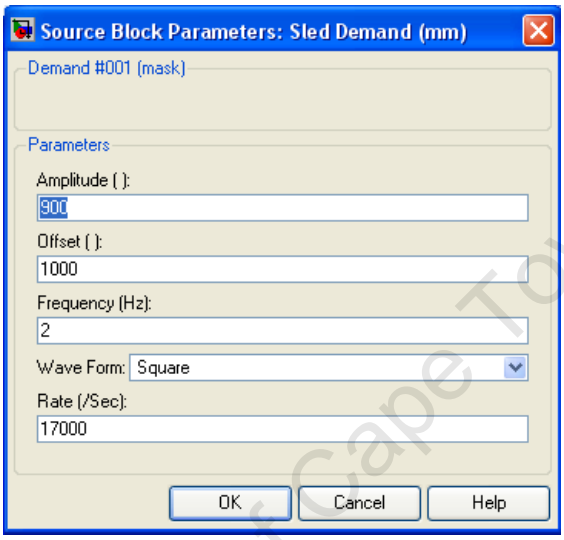

FIGURE 4-5: SCREENSHOT OF THE INPUT DIALOG FOR THE SLED DEMAND(23)

Both the values of the amplitude and frequency are somewhat arbitrary. While the amplitude dictates the distance that the sled approaches from; the frequency of the wave sets the point at which the position of the sled returns to its initial value. These values were set at 900 mm and 2 Hz respectively. The value of 900 mm allows the sled to be seen approaching the end of the piston during the simulation. A frequency of 2 Hz results in a period in which the entire event can be completed before the sled's position is reset.

The default value of 17000 per second was set for the rate. As the units of amplitude and offset are in millimetres this represents a velocity of 17 m/s, the nominal maximum contact velocity provided in the design specifications.

(3) Position Control:

The position drive signal moves the piston to, and holds it at the position set points. Depending on the state of the Release Logic (*RL*) signal either the *Retract* or *Extend* set points are used. When the *RL* signal is high the retract set point is used. Figure 4-6 shows the part of the control window relevant to the position control.

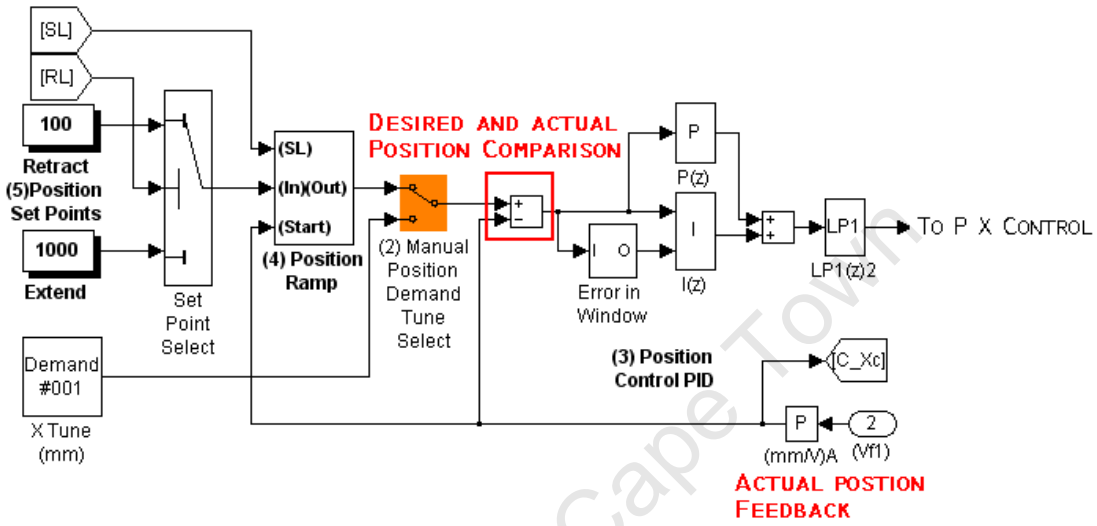

FIGURE 4-6: EXTRACT OF POSITION CONTROL PID FROM THE CONTROLLER WINDOW(23)

The *Extend* position set points relate to the operating point of the cylinder. The operating point is the position that the end of the piston rod is held at while the sled approaches the cylinder. The *Retract* set point is the position that the piston rod end is held at after the deceleration of the sled.

By comparing the feedback signal of the piston's position to the desired position outputted by the *Position Ramp* block; the remaining distance that the piston needs to be moved is calculated. After this, proportional and integral gains are applied to the signal. Finally the drive signal is passed through a low pass filter to filter out any noise in the signal before sending the drive signal to the P, X Control. Without the filter, any noise in the signal would cause the end of the piston rod to oscillate instead of remaining stationary at the position set point.

(6) Pressure Control:

The set point pressure is set by editing the value inside the box marked *Pressure Set Point* on the left hand side of Figure 4-3. This value is sent to the Pressure Control PID where the set point pressure is compared to the effective pressure of the cylinder. The blocks containing the calculation of the effective pressure of the cylinder and the comparison of it to the set point pressure have been highlighted in Figure 4-7.

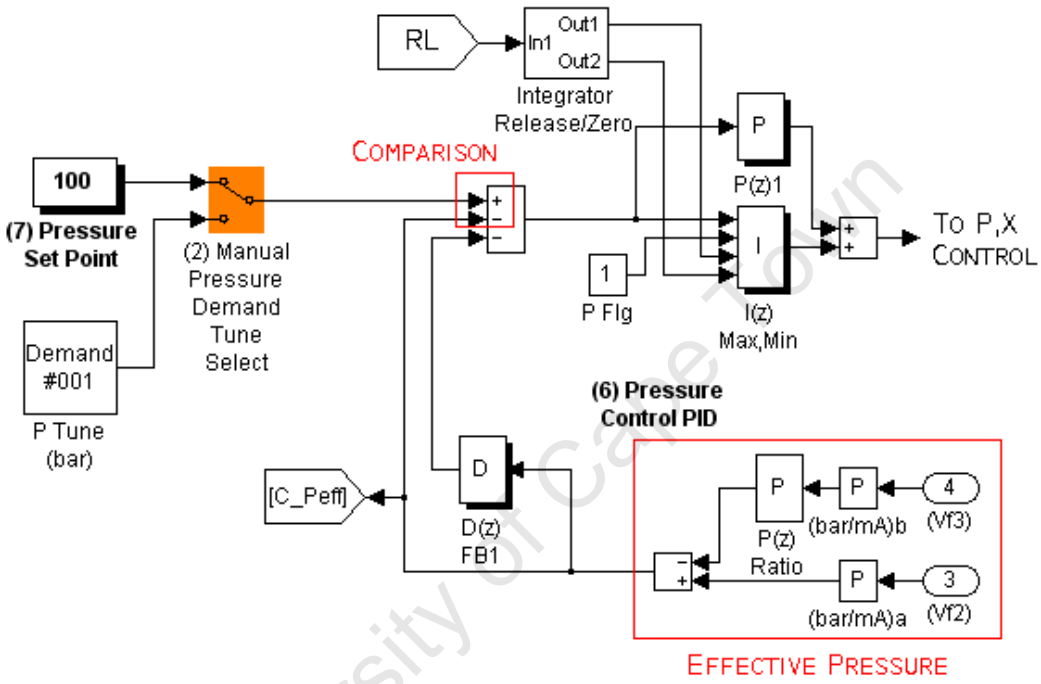

FIGURE 4-7: EXTRACT OF THE PRESSURE CONTOL PID SECTION FROM THE CONTROL WINDOW(23)

After the comparison, the various components of the PID control are applied to the difference between the values. Finally a drive signal is sent to the P, X control.

The effective pressure is the pressure that, if present in the rear chamber, would create an equivalent force to the combination of the two existing chamber pressures. In the effective pressure calculation, the signals from the pressure transducers of each of the cylinder's chambers are first converted from voltages to pressure readings. The pressure reading from the front chamber is then multiplied by a factor in the block marked *P(z) Ratio*. This ratio converts the pressure reading to a pressure which would create an equivalent force if it were applied to the bore area of the cylinder. The effective pressure is then given as the difference between these values. Equation 4-3 shows the method of calculating the

effective pressure used in the simulation. By multiplying the effective pressure by the bore area of the cylinder, the force exerted by the end of the cylinder can be calculated.

EQUATION 4-3:

$$P_{effective} = P_{rear} - P_{front} \times \frac{D_{bore}^2 - D_{rod}^2}{D_{bore}^2}$$

(8) Release Logic and Ramp Function:

By monitoring the position of the sled the block marked *Release Logic & Ramp Function* in Figure 4-4 creates two signals. The release logic signal marked *RL* is a binary signal. At the beginning of the simulation the signal is low; once the sled reaches the pre-acceleration distance the signal goes high. The RL signal is primarily used to trigger the pressure control regime.

The output marked *Vr* is the ramp function. The simulation uses this to account for an initial opening of the value and the closing transient of the valve. The simulation uses constants derived from the control parameter equations discussed in section 2.5.2.

(10) P/X Mode:

As mentioned before in section 2.5, the control sequence of the cylinder requires that the end of the piston rod be held at the operating point while the sled approaches. Once the sled reaches the pre-acceleration distance the cylinder is accelerated to match the velocity of the incoming sled; after which the effective pressure of the cylinder is regulated to the set point pressure. The block marked *P/X Mode* swaps between the two control regimes: position control and pressure control.

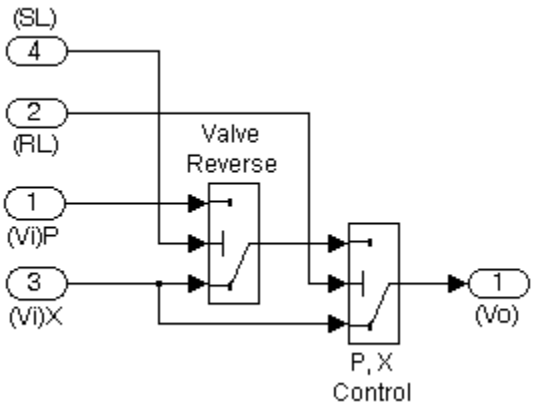

FIGURE 4-8: SIMPLIFIED SCHEMATIC THE P/X MODE LOGIC

Figure 4-8 is a schematic to help explain the logic contained in the P/X Mode block. The workings of the switches used in the diagram can be explained as follows: the middle input is the switching signal; while the switching signal is below the threshold the inputs and outputs are connected as shown in the diagram; if the switch signal increases above the threshold, the switch connects the other input to the output of the switch. Therefore while the *SL* and *RL* signals are false; their respective switches connect the circuit as shown in Figure 4-8. When they are true; their respective switches connect the other input to the output terminal.

From the schematic it can be seen that there are two possible states of the output, *Vo*. *Vo* could either be equal to *(Vi)P* or *(Vi)X*. *(Vi)P* and *(Vi)X* are the valve drive signals from the pressure and position PID controls respectively. The state of *Vo* depends on the states of the two switching signals *SL* and *RL*.

As mentioned above the *RL* signal is the Release Logic signal. It remains low as the sled approaches the end of the piston rod; once the sled's position reaches the pre-acceleration distance the *RL* signal goes high. The Sled Logic signal, *SL*, is only high while the sled is in contact with the piston rod.

There are three possible combinations of the *RL* and *SL* signals. While the sled's position is greater than the pre-acceleration distance both signals are low. Once the sled has passed the pre-acceleration distance, but not yet made contact with the piston rod, the *RL* signal is high and the *SL* signal low. After the sled has made contact with the piston rod both signals

are high. A truth table showing the resulting output from the signal combinations is given in Table 4-2.

TABLE 4-2: TRUTH TABLE SHOWING THE RESULTS OF THE P/X MODE LOGIC

RL	SL	Vo
0	0	X
1	0	X
1	1	P
0	1	N/A

From the truth table its can be seen that the control regime only changes to pressure control once the sled has made contact with the piston rod.

4.3.2 SLED AND HYDRAULIC MECHANICAL SYSTEM

The block marked *Sled Hydro Mechanical System* in Figure 4-3 contains a lumped parameter model of the sled and the deceleration system. The entire system is broken into seven blocks. Five of these represent the different components of the deceleration system and two describe the sled. A schematic of the contents of the Sled Hydro Mechanical System is shown in Figure 4-9 on page 64.

On the left hand side the valve drive signal, *Vo*, from the controller, enters the *D665_K15HAJ* valve block. From this block the flow rates of the hydraulic fluid into each chamber of the cylinder are given by *Qa* and *Qb* which are sent to the *Turbulent Cross Port Bleed* block. The effect of the cross port flow on the flow rates of the two chambers is accounted for in this block and the adjusted flow rates forwarded to the *Double Acting Cylinder* block. As mentioned before, the bleed is used during the pressure tuning of the control system and is otherwise sealed.

In the *Double Acting Cylinder* block the dimensions of the cylinder; the flow rates into the chambers; the velocity of the piston and its position are all taken into account. The calculations give the force exerted by the cylinder and the new chamber pressures. The inertia of the piston rod and the contact plate are accounted for in the *Cylinder & Plate Mass* block from this, the new position and the velocity of the piston are found.

The next block labelled *Contact Plate,* models the interaction of the sled and the end of the piston rod. Fixed to the end of the piston rod is a 25 mm thick rubber stopper whose

damping properties are accounted for in this block. The block uses the positions and velocities of the piston and sled as well as the properties of the rubber to calculate the force exerted on the Sled. The properties of the rubber stopper were described using a spring dashpot model. The spring constant was set at $2000\,\frac{kN}{mm}$ and the viscous damping coefficient at $10\,\frac{kN \cdot s}{mm}$. Using Equation 4-4 the and the dimensions of the stopper, the equivalent Young's modulus was found to be 1.97 GPa. This is a simplified model of the hyperelastic properties of the rubber. The model assumes that the material would behave linearly which is an acceptable assumption where strains are low(24).

EQUATION 4-4:

$$\frac{F}{A} = \sigma = E\epsilon = E\frac{\Delta l}{l}$$

$$\Rightarrow E = \frac{Fl}{A \cdot \Delta l} = \frac{Kl}{A}$$

Finally the effect of the force on the inertia of the sled is found in the *Sled* block. The new position and velocity of the sled are known and are fed back to the *Contact Plate* block to be used in the calculation for the next time step. The block marked *Sled Drive* is only used at the start of the simulation to initiate the approach of the sled. An interval test forces the value of the additional drive force to zero as the sled nears the end of the piston. This ensures that the *Sled Drive* does not affect the deceleration of the sled.

The values of the cylinder's chamber pressures and both the piston and the sled positions are fed back to the controller via the output port 1 to 4.

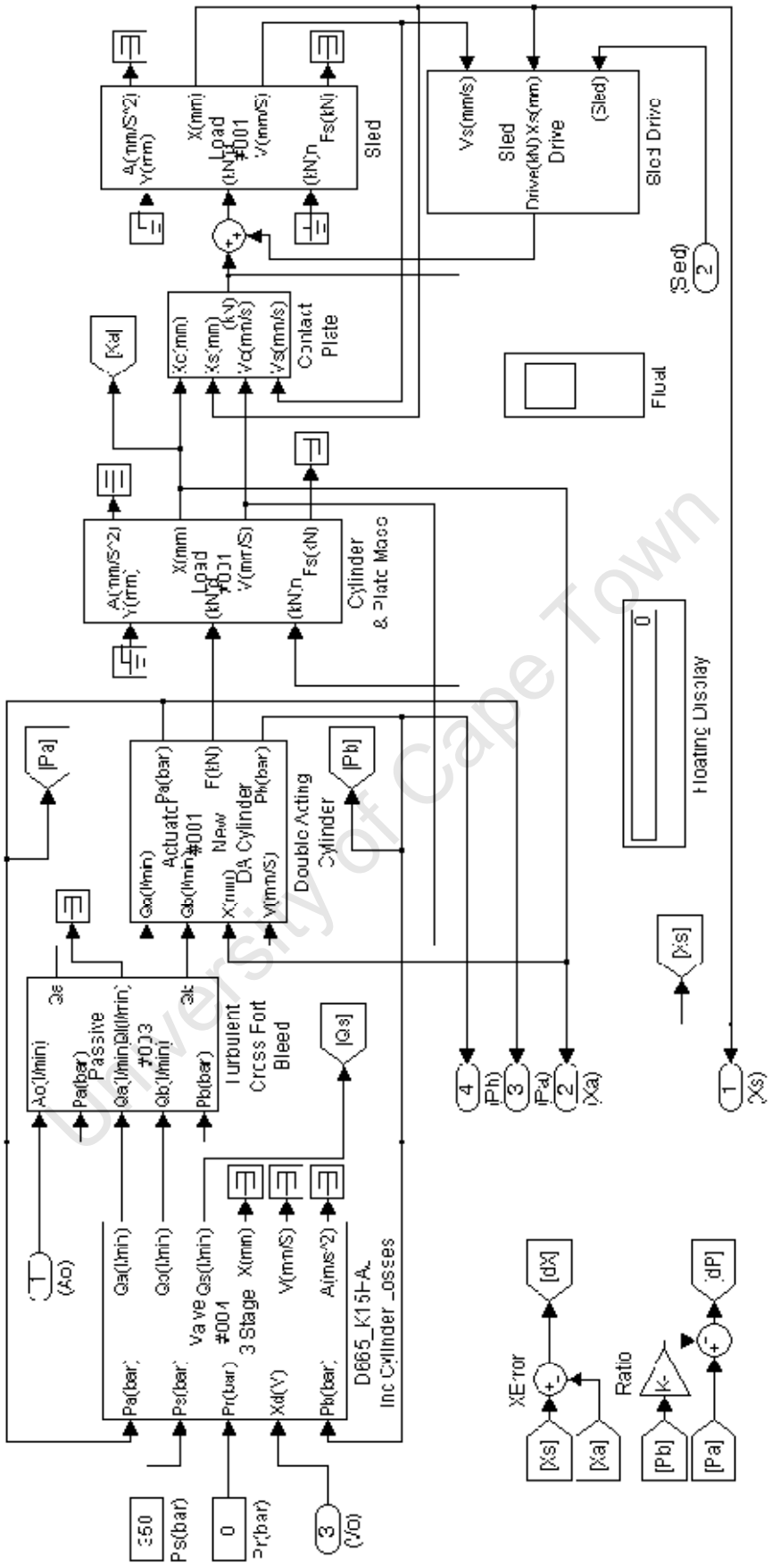

FIGURE 4-9: SCREEN SHOT OF THE SLED HYDRO MECHANINCAL SYSTEM WINDOW

4.4 COMBINING THE ACCELERATION AND DECELERATION STAGE MODELS

Combining the Acceleration and Deceleration stage models consisted of two phases. Firstly the effects of the free sliding section between the two stages on the contact velocity were accounted for and the adapted results sent to the Deceleration stage model. Secondly a script file was written which: accepted the required user input; ran the separate parts of the model in the correct order; accounted for the free sliding section and compiled the results of both simulations into plots and a TSV text file.

The main benefit of combining the simulations in this manner was convenience. After the models were combined, the user only had to specify the input data once and the relevant information was relayed to the necessary parts of the simulations. A secondary benefit was that it eliminated the possibility of deceleration stage results being paired with the incorrect acceleration stage results.

Another useful feature was the addition of a loop which enabled the user to run multiple deceleration stage simulations from one set of acceleration stage results. Although the plots from the different stages were not plotted on the same axes; the titles of all of the plots state the relevant input data to avoid the pairing of incorrect acceleration and deceleration profiles.

Separate TSV text file are created for each deceleration stage. Each TSV text file holds velocity and force data for both the acceleration and deceleration stages and is named according to the input parameters of the simulation.

The input parameters that can be changed from the script file are: the sled mass; pneumatic supply pressure; the number of acceleration values; the number of cushioning air valves and the deceleration pressure set point. On execution, the script file sets the values of the input parameters to those specified by the user after which the script file calls the acceleration stage model. Once this has been completed the *PlotOut* sub procedure is called. This creates plots of the acceleration stage variables over the duration of the acceleration stage.

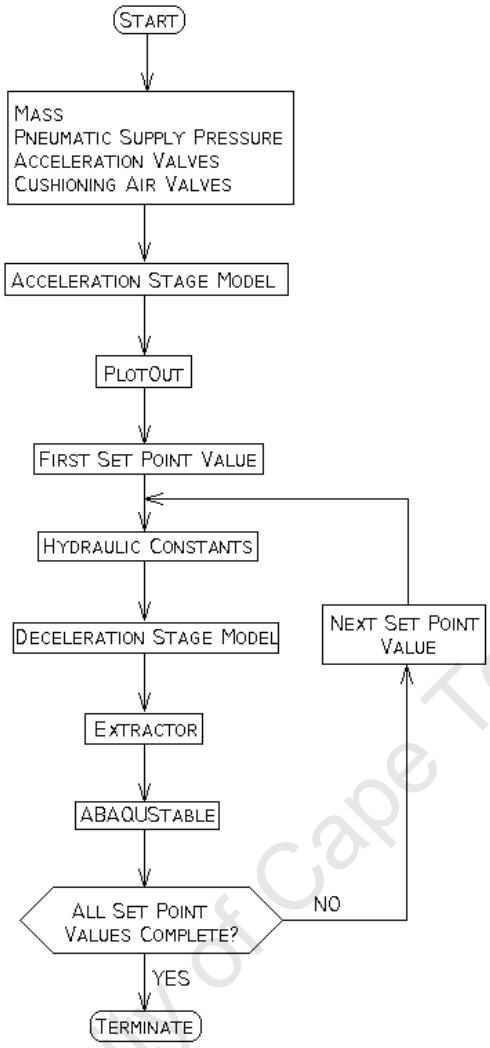

FIGURE 4-10: FLOW DIAGRAM OF THE COMBINED SIMULATION SCRIPT FILE

After the plots of the acceleration stage have been created the script file prepares to execute the deceleration stage simulation. The *HydraulicConstants* sub procedure is called which: defines the properties of the hydraulic cylinder; calculates the deceleration over the free sliding section (and thus the contact velocity); as well as calculating the control parameters using the Parameter Adjustment Equations supplied by MOOG(6). Some of the control parameters are dependent on the set point pressure which is why the sub procedure is incorporated into the loop.

The Simulink model created by the suppliers is called after the *HydraulicConstants* sub procedure. To be able to feed the relevant information to the Deceleration Stage simulation and retrieve the desired output, the original simulation had to be modified slightly. Values of user definable constants in the Simulink model were converted to variables. This allowed

the value of the variables to be set by the MatLab script prior to calling the Simulink simulation; allowing the values of constants to be easily adjusted. Minor changes to the block model diagram were made so that the values of the force experienced by the sled and its acceleration could be logged during the simulation.

Once the Simulink simulation is completed, the *Extractor* sub procedure is called. This sub procedure extracts the logged data from Simulink and creates plots of these values. As the data is logged over the entire duration of the simulation the initial values are irrelevant as they represent the approach of the sled. The only data of interest is that after the moment of impact. An algorithm which finds the moment of impact and collects the data from that point on was implemented to create plots of the data during the deceleration stage.

The final sub procedure, *ABAQUStable*, creates the TSV file. A file is created for each set point pressure specified by the user. Each file contains the velocity and force profiles for the acceleration and deceleration stages of the relevant simulation. The files are named according to the input parameters of the particular test. This means that if a test with the same input parameters is run, the old file will be over written.

After the loop has been executed for all the specified set point pressures the script file terminates. The resulting plots and TSV files for all the simulated stages are then available for the user to analyse or incorporate into other simulations.

4.5 OUTPUTS FROM THE ACCELERATION AND DECELERATION STAGE MODELS

Both the Deceleration and Acceleration Stage models log a number of variables at each time step over the duration of the simulation. Included in these are: the piston velocities, chamber pressures, piston stroke and the force experienced by the sled.

The main purposes of the models were to predict the maximum velocity and the deceleration experienced by the sled. A secondary purpose was to create loading profiles to be used in the finite element analysis of the entire structure. For this reason plots and tables of the variables which relate to these aspects were created by the script file.

As the finite element model was to be dynamic there were two obvious approaches towards the loading of the sled: either by exerting a load on the sled equal to the predicted force

history experienced by the sled or by enforcing the velocity profile predicted by the simulations. Both the velocity and force histories were written to the TSV text file. As ABAQUS could accept amplitudes in a tabular form, the format of the TSV text file was arranged to allow the data points to be easily copied and pasted out of the text file.

During both the acceleration and deceleration stages; values of different variables were recorded. The values recorded over the acceleration stage are listed below:

Piston Velocity
Piston Position
Force Exerted by the Piston
Both Chamber Pressures
Air Mass in both Chambers
Temperature of Air in both Chambers

These values are all recorded once for every time step, allowing them to be plotted over the duration of the simulation. The plots that were created in the *PlotOut* sub procedure are listed below:

Chamber Pressures vs. Time
Piston Velocity vs. Time
Piston Velocity vs. Piston Position

As mentioned before, the simulation received from the deceleration system suppliers was modified to output different variables to the original simulation. After the modifications the variables that were logged by the simulation are listed below:

Piston Position
Both Chamber Pressures
Sled Position
Sled Velocity
Sled Acceleration
Force Exerted on the Sled

From this data the following plots are created by the *Extractor* sub procedure:

Sled Velocity vs. Time - before illuminating data prior to impact

Sled Velocity and Acceleration vs. Time - after impact

Sled and Piston Position vs. Time - after impact

Effective Cylinder Pressure vs. Time - after impact

In the *ABAQUStable* sub procedure the sled's velocity profiles from both stages are plotted against time. Tables of the force and velocity profile coordinates for both stages are also written to a TSV file. As the force extracted from the acceleration stage was the force exerted by the piston, this force was reduced by a mass ratio to ensure that the acceleration of the sled was the same as in the acceleration stage prediction. If the force exert by the piston was applied to directly to the sled the final velocity of the sled would be much higher than that predicted. The mass ratio was found by equating: the acceleration created by the force exerted by the piston on the masses of the piston and the sled; to that of the force exerted on the sled on only the sled mass. A simple derivation is shown in Equation 4-5:

EQUATION 4-5:

$$\frac{F_p}{(m_{sled} + m_{pis})} = a = \frac{F_{sled}}{m_{sled}}$$

$$\Rightarrow F_{sled} = \frac{m_{sled}}{(m_{sled} + m_{pis})} F_{pis}$$

From these outputs the user can analyse the predicted dynamics of the sled, and assess the suitability of the resulting g forces before any physical tests are run. The tables written to the TSV file can easily be used in other simulations to analyse different phenomena not covered by this simulation. An example of this is the use of the data in a finite element analysis to assess the structural integrity of a proposed test specimen restraint system.

5 FINITE ELEMENT MODEL OF THE SLED TESTER

5.1 INTRODUCTION

To investigate the dynamic response of the rails and their support structure to the loading created by the interaction between the sled and the rails, a finite element model of the structure was created. By modelling the frictional contact between the slides of the sled and rails, the loading caused by the moving sled on the rail structure was predicted.

The finite elements model, created in ABAQUS, is described in the following sections. Methods used to constrain and load the system are also discussed.

5.2 MODEL DESCRIPTION

A finite element model of the rails, their supporting structure and the sled were created using ABAQUS. As the design of the rail structure was known, a model was created using the dimensions and materials of this design. In the case of the sled only preliminary conceptual designs had been put forward. The sled used in the model went through a number of revisions before a concept (which represented a possible solution and which met the specification of the sled design) was found.

A full 3D model of the system was used to allow the sled's movement to only be restricted by its interactions with the rails. If a half symmetry model was used, the boundary conditions would restrict the sled from being able to roll and or yaw. As it was possible that there would be a significant clearance between the rails and the sled's slides; these degrees of freedom were found to be of importance. Significant amounts of roll and yaw would result in localised loading of the slide and rails, which could lead to high frictional forces that could damage the structures.

5.2.1 MODEL GEOMETRY

5.2.1.1 RAILS AND SUPPORTING STRUCTURES

The design of the rails and the supporting structure consisted of the rails themselves, which were each supported by two long steel channels which ran the length of the track. The channels were bolted together in an over and under arrangement to form the rail supports. The bottom flanges of the lower channel sections were bolted onto cross members. These were made from shorter lengths of the same channel section bolted back to back to form an I-beam profile. The cross members were fixed to the concrete floor via threaded M20 chemical anchors. The photos in Figure 5-1 show the constructed rails system.

FIGURE 5-1: PHOTOS SHOWING THE CONSTRUCTION OF THE RAIL SUPPORT STRUCTURE

To ensure the rail supports remained equidistant along their entire length, each of the braces between the rail supports consisted of a length thick walled tubing through which a length of M20 threaded bar is passed. The threaded bar also passed through holes in the lower of the two long channels. By fastening nuts on either side of the threaded bar the

channels were abutted against the ends of the tubing. The lengths of thick walled tubing were carefully machined to be the same length; ensuring that the rails remained equidistant along the length of the track.

The dimensions of the rails, steel channel and the tubing used, are show in the sketches in Figure 5-2 (dimensions in mm).

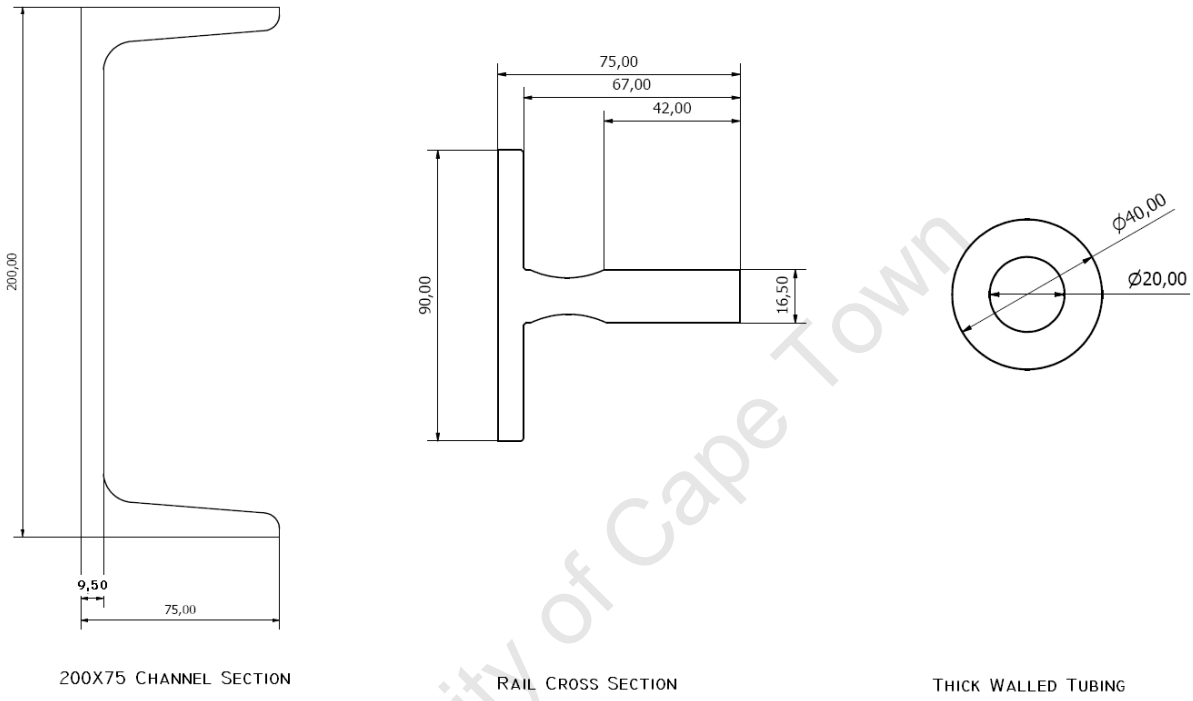

FIGURE 5-2: CROSS SECTIONS OF PHYSICAL RAIL COMPONENTS

As mentioned before shell elements were used to model the rail support structure. This required the channel section geometry to be simplified. In the final model three different parts were used to describe the geometry of the rail supporting structure. These were: the cross member and anchor bolts; the rail support; and the braces. The braces were extruded from the left hand side rail support.

In the case of both the rail supports and the cross members the bolts holding the channel sections together were not modelled. The assembled profile was simply used, and the thickness of the sections increased where the channels' faces overlapped. This could be done as it was assumed that the bolts created a tied constraint between the channel sections.

In Figure 5-3 (dimensions in mm) sketches of the dimensions of the extrusions used to model the cross members and the rail supports are given. The dimensions took into account the section thicknesses that were assigned to the extrusions. After the cross sections had been extruded, holes were cut in both parts at the points where the rail supports were bolted to the cross members. The holes were cut as squares to minimise their affect on the mesh quality. The square holes would introduce artificial stress concentrations; these were assumed to be insignificant when analysing the entire system.

The sections were extruded to the nominal length of the components used in the construction of the structure. The rail supports were extruded by 10825 mm and the cross members by 1600 mm.

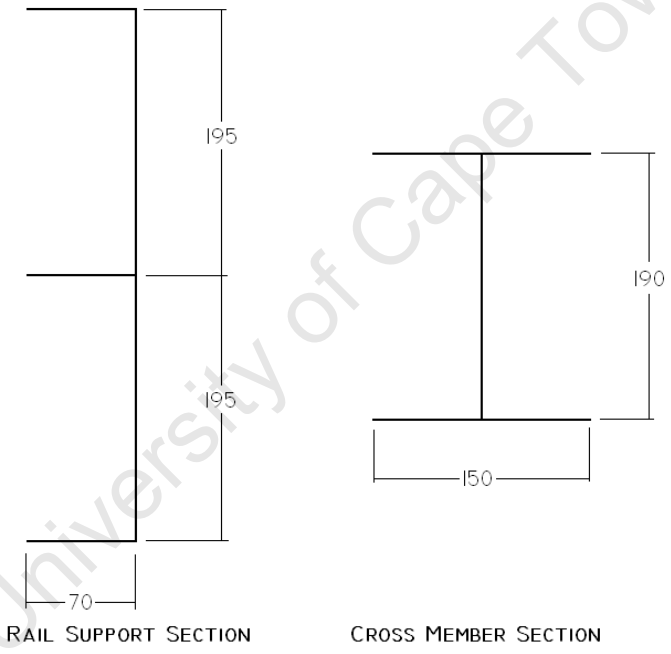

FIGURE 5-3: DIMENSIONS USED TO CREATE THE SHELL MODELS OF THE RAIL SUPPORTS AND CROSS MEMBERS

Four circular extrusions were made from the bottom face of the cross member part. These extrusions represented the anchor bolts, which grounded the entire structure to the concrete floor. Figure 5-4 shows an image of the complete cross member geometry.

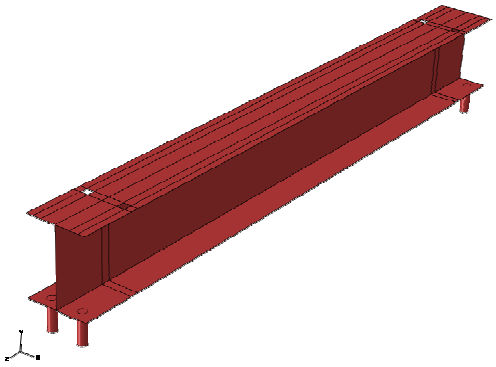

FIGURE 5-4: IMAGE OF THE CROSS MEMBER PART

As the cross members were not equally spaced along the length of the rail supports. The rail support geometry had to be mirrored to achieve the correct spacing on both the left and right hand supports; resulting in different parts for each of the supports.

A small extrusion along the length of each of the rail supports was made on which to mount the rails. These extrusions allowed the rails to be coupled to the rail supports using a shell to solid coupling. The extrusions were placed 124 mm from the top of the rail support section, along the length of the support where the rail was to be fixed.

In the initial models the braces between the two rail supports were omitted. The results of the simulations showed that both the rail supports deflected outwards. The effect of this on the braces would be to increase the tension in the thread bar sections. Modelling the thick walled tubing between the supports would involve computationally expensive contact interactions. Contact would have to be applied between the inner surface of the tubing and the threaded bar, as well as between the ends of the tubing and rail supports. As the loading of the braces would cause them to be in tension and the design only allowed the tubing to be loaded in compression; the tubes were not modelled.

Instead, the braces were modelled as 20 mm diameter bars, which joined the two rail supports. Circular extrusions, 1242 mm in length, were made from the left hand rail support. The right hand support was partitioned in the appropriate places to be able to tie the end of the braces to the support. It was noted that the 20 mm bars would not exhibit the same bending stiffness as the actual braces, as they were thinner.

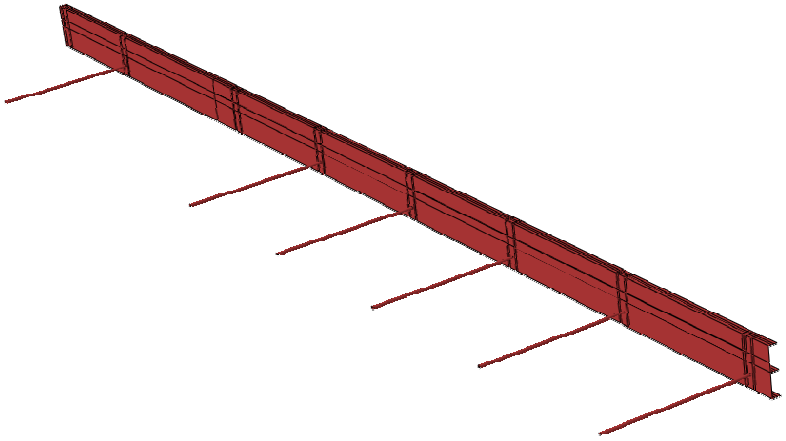

FIGURE 5-5: IMAGE OF THE ENTIRE LEFT HAND SIDE RAIL SUPPORT INCLUDING THE BRACES

Figure 5-5 shows the entire left hand side rail support including the extrusions representing the thread bars. The enlargements in Figure 5-6 show how the braces were placed in line with the bolt holes cut into the bottom flanges of the rail supports. The black lines in the images show the partitioning used to improve the mesh quality. The longitudinal line through the middle of the upper channel section is the extrusion used to couple the rail to the rail support.

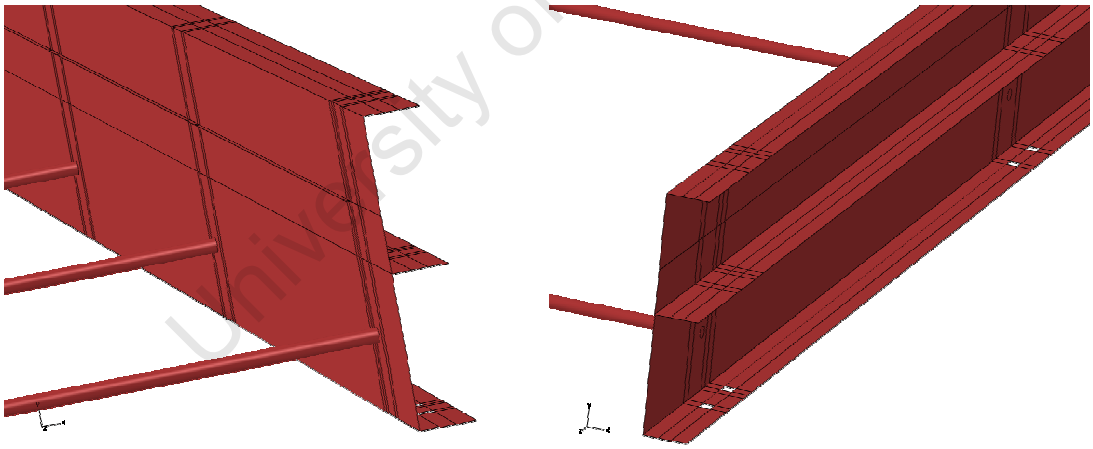

FIGURE 5-6: ENLARGEMENTS OF THE DECELERATION END OF THE LEFT HAND SIDE RAIL SUPPORT

The rail which was coupled to the rail support via the shell to solid coupling was modelled from continuum elements; hence the need for a shell to solid coupling. The rail section was simply modelled by an extruded rectangle, 16.5 mm thick and 67 mm wide. It was extruded by 7.5 m. Once this geometry had been coupled to the 5 mm extrusion it represented the rail's cantilevered length and thickness.

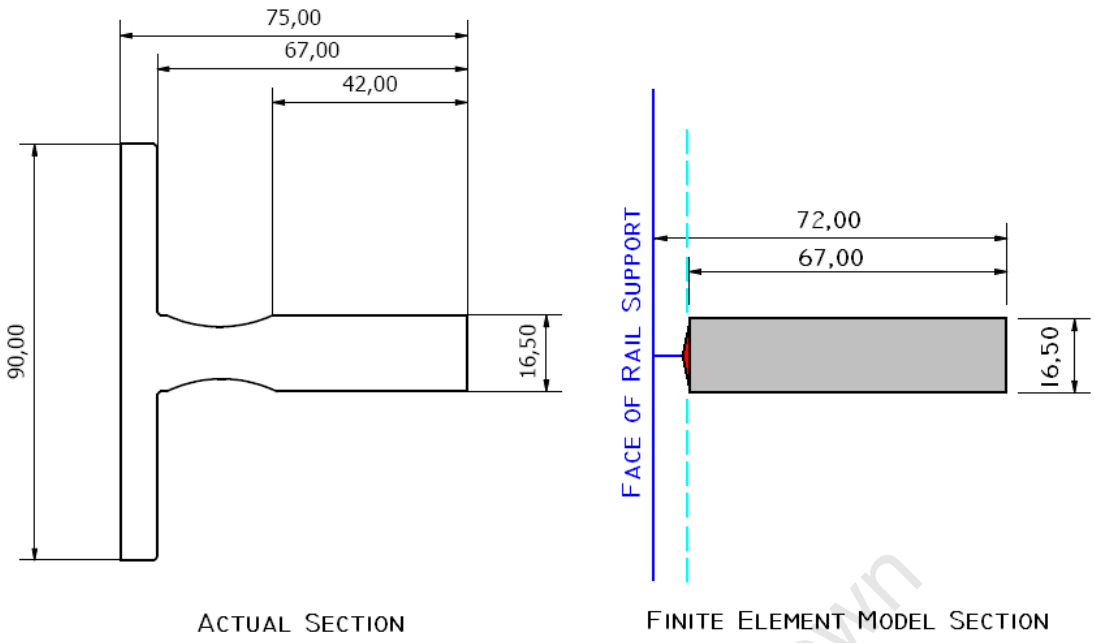

FIGURE 5-7: SKETCH SHOWING THE SIMPLIFICATIONS MADE TO THE RAIL GEOMETRY

In Figure 5-7 (dimensions in mm), the grey block represents the cross sectional geometry of the rail in the finite element model. The red triangle shows where the shell to solid coupling was applied. The dark blue line represents the shell elements of the rail support.

A width of 5 mm was chosen for the small extrusion to avoid over closure between each of the rail supports and the rails. Once the shell was assigned a thickness, the rail support material occupied the area up to the dashed light blue line.

5.2.1.2 SLED AND SLIDE STRUCTURES

As mentioned before only preliminary concepts of the sled design were available. To be able to realistically analyse the loading of the rails and their supporting structures a model of the sled and its sliding mechanisms was needed. After a number of revisions a conceptual model which met the sled's specifications was achieved. Issues surrounding the manufacturing of a sled based on this model were not considered; the detailed design concerning the attachment of components and adjustment allowances were not a part of this study.

To allow the sled to move freely along the rails it was decided that the sled would slide on a low friction polymer. The concept employed in this model was to mount the polymer blocks on to a steel structure, which could be fastened to the four corners of the main structure of the sled. The steel would give the slides strength and rigidity.

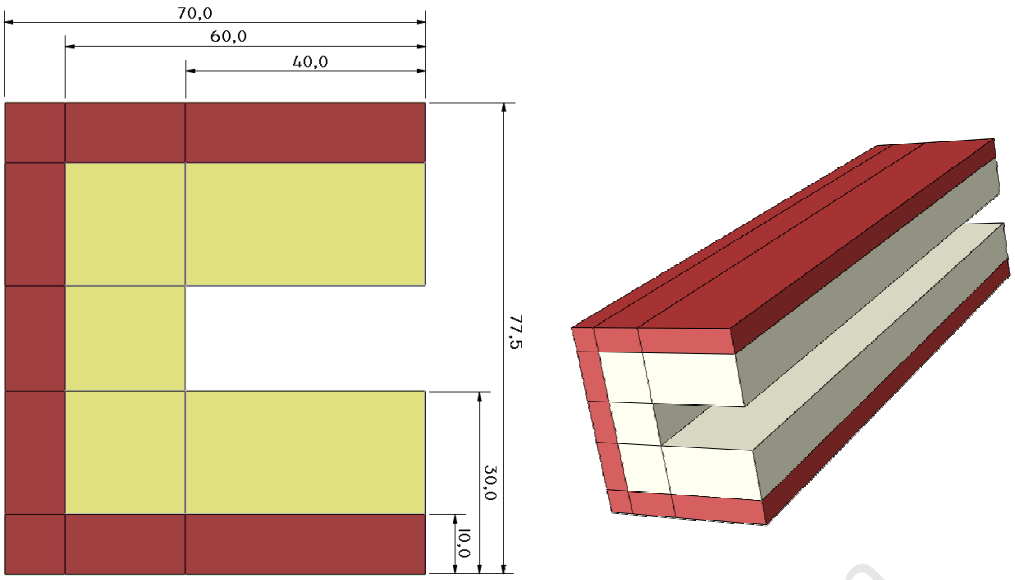

FIGURE 5-8: IMAGES OF THE MODELLED SLIDE GEOMETRY

Figure 5-8 (dimensions in mm) shows the geometry used to model the slide. A clearance of 1 mm in both the vertical and horizontal directions was assumed for each slide. In the images, the red sections show the steel sections while the cream sections represent the polymer. The slides were extruded to be 300 mm long.

The main specifications that the sled needed to satisfy were: mass, size and survivability of the structure. The designs of both the acceleration and deceleration systems had been based on the maximum mass of the sled and its payload being 300 kg. If this mass was exceeded, the achievable velocities and decelerations would decrease.

As the sled would have to hold test specimens and some instrumentation, the loading area was important. A nominal length of 2 m was decided on. This would allow a Hybrid III dummy to lie horizontally and leave space for the instrumentation. The width of the sled was determined by the distance between the rails and the width of the dummy. It was assumed that the dummy would be the largest test specimen used. To save weight the loading area did not need to stretch from rail to rail, but the mounting points for the slide would have to be sufficiently far apart so that the slides engaged with the rails. Using the slide model discussed above the mounting points needed to be 1036 mm apart. The width of a 50th percentile male Hybrid III dummy is 437 mm at the widest point.

Due to the high decelerations experienced by the sled, the inertial forces created by the mass of the dummy and restraint system created large bending loads in the structure. It was therefore important that the design of the sled was strong enough to handle these loads.

Initially the sled model consisted of a steel plate, reinforced by a box section and stiffened with gussets. This design was not intended to meet the mass specifications as it was a preliminary model which was used until the teething problems regarding the sliding contact between the sled and the rails were resolved.

The first revision of the design addressed the mass of the sled. In order to reduce weight the material was changed to Aluminium. The actual design was also changed. Four lengths of channel section were run parallel to the direction of the rails. Two sections were placed back to back along the middle of the structure. The remaining two sections were placed at the extreme edges.

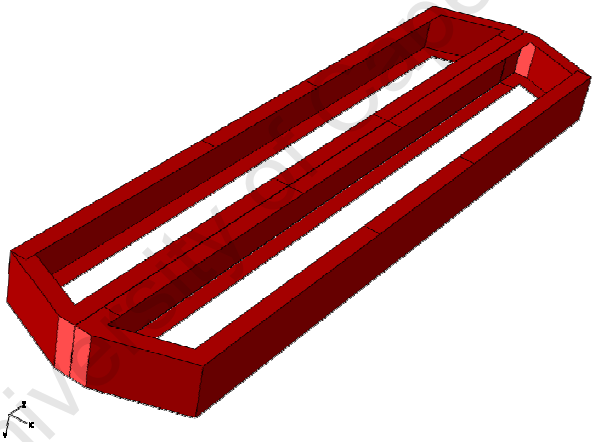

FIGURE 5-9: IMAGE OF THE FIRST REVISION OF THE SLED DESIGN

The channel sections were joined by more channel sections which formed impact regions on either end of the middle channel sections. The image in Figure 5-9 shows the assembly of the channel sections. Initial loading tests on the structure showed that although both the cylinders made contact with the sled in the middle, the main stress path was through the outer channels. This was due to the loading assumption that the restraint system would be bolted to the outer channels. This assumption was made because the preliminary concept had tapped holes along each of the outer edges of the sled for attaching the restraint system. This loading scenario meant that the channel section placed in the middle of the structure carried relatively no load. A new revision taking this into account was developed.

It was also seen that the flanges of the outer channel sections were deforming at the restraint system's attachment area. To strengthen the attachment areas the channel sections were replaced with box sections and the thickness of the restraint system attachment area was also increased.

An oval shaped structure built up from box sections was modelled and tested. Although the box section beams resisted the bending loading well, the forces transferred to the rails were large. This was a result of the reduced distance between the slides on each rail, which was due to the sharper impact cones.

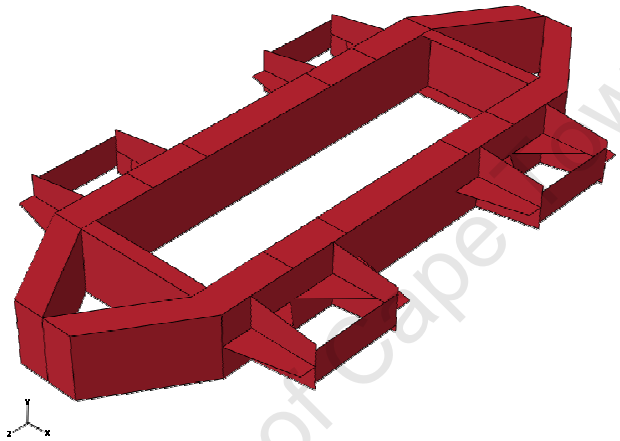

FIGURE 5-10: IMAGE OF THE SECOND SLED REVISION

It was also found that the lower elastic modulus of the Aluminium resulted in larger deflections of the mounting structures. As the slides were mounted onto the end of these structures their alignment with the rails was compromised as the mountings moved. The misalignment of the slides caused localised loading of the slide material, which resulted in high frictional forces and destructive deceleration levels.

To remedy these two issues another revision was made to the model. The slide mounting points were moved closer to the ends of the sled to minimise the forces applied to the rails. The deflections were minimised by adapting the design to improve its stiffness. The final version of the model is shown in Figure 5-11.

The final revision of the sled model employed a sharper impact cone in the front than at the rear, as the forces created in the deceleration stage were larger than during the acceleration

stage. A sharper cone avoided buckling of the structure, allowing the stress to flow through the load carrying members of the design.

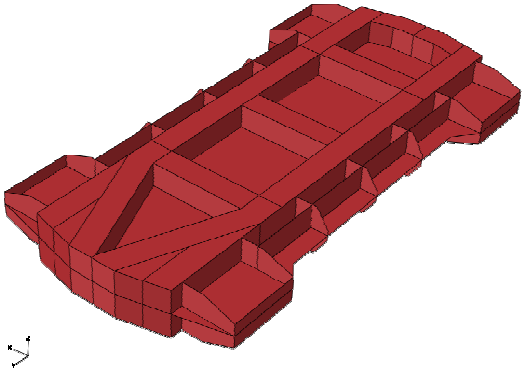

FIGURE 5-11: IMAGE OF THE FINAL REVISION OF THE SLED

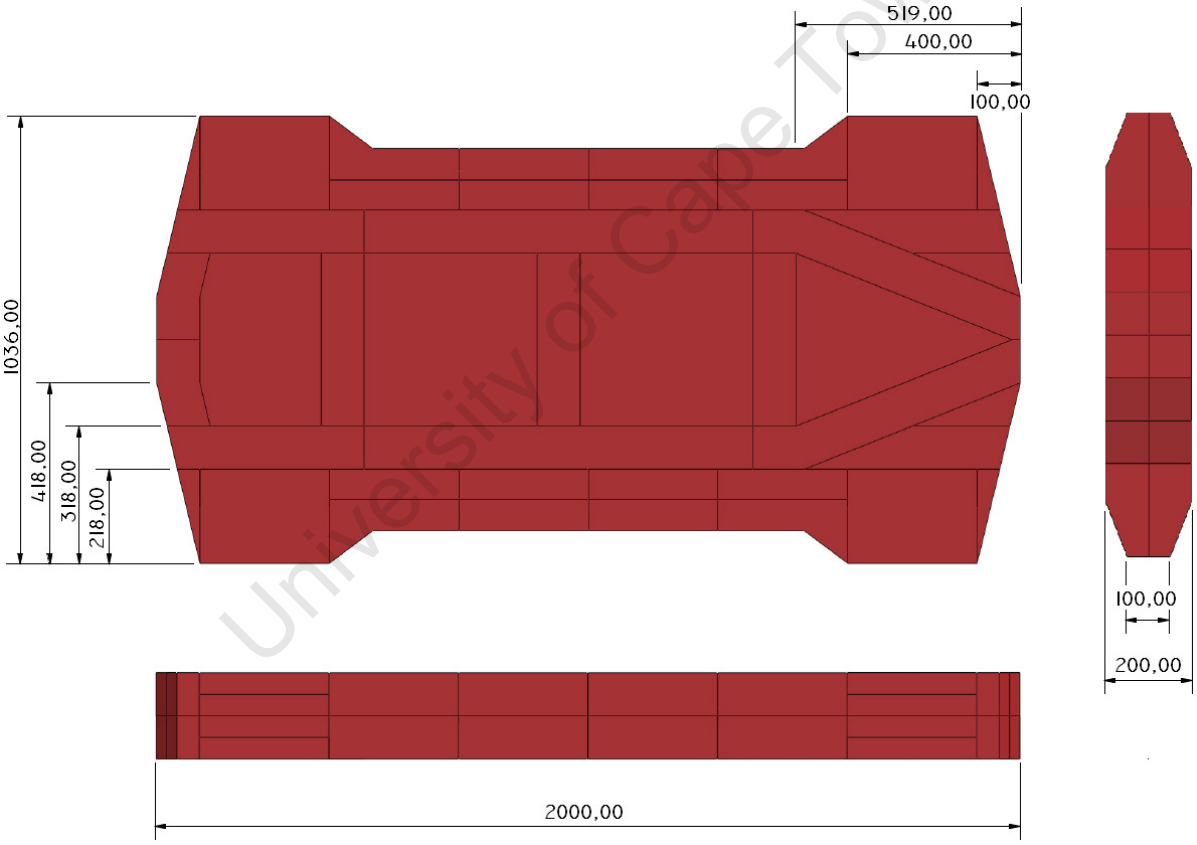

FIGURE 5-12: DIMENSIONED IMAGE OF THE FINAL REVISION OF THE SLED MODEL

The dimensions of the model's final revision are shown in Figure 5-12 (dimensions in mm). Notice that the front of the sled, the end which engages with the deceleration cylinder, is a more substantial structure in comparison to the other end. It was unnecessary to have a reinforced structure at the rear due to the lower forces applied by the acceleration stage.

5.2.2 MATERIAL PROPERTIES

As it was intended that the design of the components would result in reusable structures, the stresses in all the materials were kept below their yield points. This allowed simple material models to be used. Only data over the elastic region of the material had to be considered.

For the metallic materials, mild steel and aluminium the properties were described using their Young's Modulus, Poisson's ratio and density. The low friction polymer used in the slides was assumed to be ERTACETAL C. This material had already been specified as the low friction polymer and supplied before the start of this project.

ERTACETAL C is an Acetal Copolymer which exhibits: good sliding properties, excellent machinability, very good dimensional stability and high impact strength (25). Being a polymer the material exhibits viscoelastic properties. In the interest of simplicity – linear elasticity was assumed by using the tensile modulus of elasticity from the ISO 527 standard. ISO 527 defines the tensile modulus of elasticity as the gradient between the points on the stress strain curve at strains of 0.05% and 0.25%(26).

This modulus, the density and the friction coefficient between the polymer and steel were all available from the supplier's datasheet(27). The Poisson's ratio of the material was not available on the supplier's datasheet. Datasheets of two similar products from two different suppliers reported the Poisson's ration of their products to both be 0.35(28)(29). This value was assumed to be the same for the ERTACETAL C.

TABLE 5-1: MECHANICAL PROPERTIES OF THE MATERIALS USED

	Units	Steel	Aluminium	ERTACETAL C
Young's Modulus	GPa	207	71.7	3
Poisson's Ratio	-	0.3	0.333	0.35
Density	kg/m^3	7800	2660	1410

The coefficient of friction between ERTACETAL C and steel was reported as 0.25(27).

To monitor that the materials had not been strained beyond the elastic region, their yield stresses were compared to the maximum stresses produced by the finite element model. The steel and polymer had already been purchased so the values of their yield stresses were fixed. As the design of the sled had not been completed at the time of this investigation; the

material had not been purchased. For the sake of this investigation a high strength Aluminium alloy was assumed. The yield strengths of the material are given in Table 5-2.

TABLE 5-2: MATERIAL YIELD STRENGTHS

	Yield Strength	
ERTACETAL C	70	GPa
Mild Steel	250	GPa
Aluminium 7015-T5	315	GPa

5.2.2.1 SECTION ASSIGNMENT

To assign different materials to different areas of the model, sections were created which described the materials and assigned them to the different areas. For the sections involving shell elements the material and the thickness of the section needed to be assigned. The continuum element section only needed to have the material assigned.

The issues surrounding the shell normal orientations and offsets are explained in section 5.2.3.2.

Rail

The rail was a simple part, made only of steel and was modelled using continuum elements. For this reason the entire rail was assigned a homogenous solid steel section.

Slide

Although still modelled using continuum elements, the slide part contained two different materials. Two different sections were assigned to the part: a homogenous solid steel section and a homogenous solid ERTACETAL C section. The steel section was assigned to the outer cell and the polymer section to the inner cell.

Cross Member

As the cross member was modelled from shell elements, a thickness needed to be assigned as well as a material. Two different sections were created: a 20 mm thick homogenous shell steel section and a 10 mm thick homogenous shell steel section. The 10 mm section was assigned to the grounding bolts and the top and bottom flanges. The web between the

flanges was assigned the 20 mm section. The web was assigned the thicker section as the physical cross member was constructed from two channel sections placed back to back.

Rail Support

Also modelled from shell elements the rail supports consisted of three different sections. A 10 mm thick homogenous shell steel section was assigned to the outer flanges and webs of the two channel sections as well as the braces. The inner channel flanges which were modelled as one were assigned a 20 mm thick homogenous shell steel section. Finally the small extrusion used to attach the rail was assigned a 16.5 mm thick homogenous shell steel section.

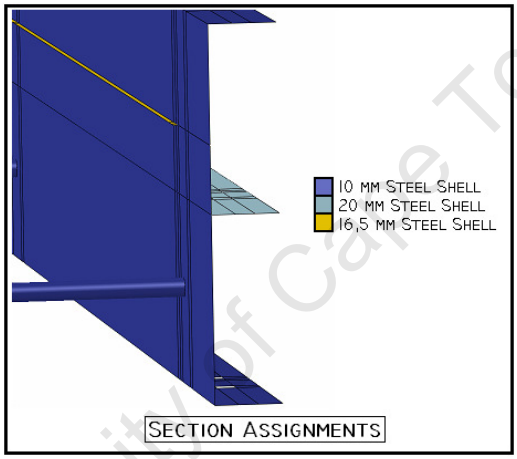

FIGURE 5-13: GRAPHICAL REPRESENTATION OF THE RAIL SUPPORT SECTION ASSIGNMENTS

Sled

The final revision of the sled had two different material sections. In areas where more strength was needed a 12 mm homogenous shell aluminium section was used. A 6 mm homogenous shell aluminium section was assigned to less critical areas.

Notice in Figure 5-14 how the area where the restraint system was assumed to be attached was thickened. This was done to increase the rigidity of the mounting area as well as incorporate the mass of the extra material which would be necessary to create the tapped connection points.

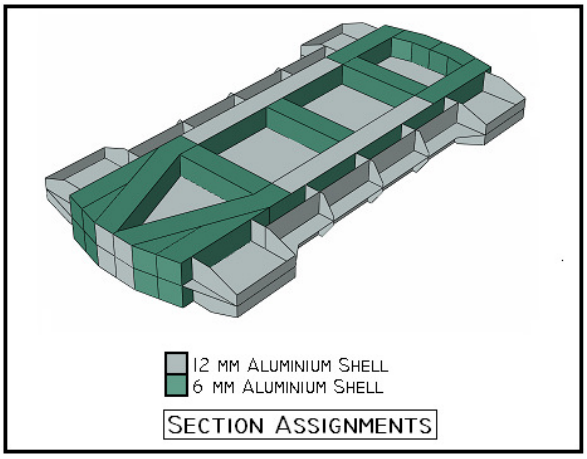

FIGURE 5-14: GRAPHICAL REPRESENTATION OF THE SLED SECTION ASSIGNMENTS

5.2.3 MESHING AND ELEMENTS

As an explicit solver was used to solve the finite element problem the mesh size and wave speed controlled the critical time step of the simulation. Wave speed though a material is a function of the materials elastic modulus and density; it describes the speed at which a stress wave travels through the material(30).

EQUATION 5-1:

$$c = \sqrt{\frac{E}{\rho}}$$

EQUATION 5-2:

$$\Delta t_{crit} \propto \frac{l}{c}$$

Where *c* is the wave speed

Refining the mesh increases the degrees of freedom in the simulation; lengthening the solving time. It also shortens the length of the element edges, which shortens the critical time step; thus increasing the number of time iterations taken to reach the end of the simulation duration.

To capture the stresses in the steel part of the slide at least three elements were needed through its thickness of the section. The resulting critical time step was the main cause of the long run times. This was accentuated by the size of the entire model.

Measures were taken to minimise the computational expense from the start. Shell elements were used over continuum elements wherever possible. Most of the physical structure was constructed from channels sections, which have a relatively thin thickness compared to their section dimensions. They leant themselves to be adequately modelled by shell elements. The only parts of the model which used continuum elements were the rail and the slides.

Initially the rail and slides were also modelled using shells. The contact interaction between the rail and the slides caused bull-nosing and visualisation of the interacting surfaces was poor. For this reason continuum elements were used.

Consistency between the meshes of some of the components had to be considered. The shell to solid coupling was not as robust as a tie constraint. This meant that to ensure coupling of all the nodes along the faces connecting the rails to the rail supports, the mesh spacing along the length of the part needed to be exactly the same.

Another consideration was the contact interaction between the rails and the slides. It was found that having the same node spacing in the perpendicular direction on both of the contact surfaces gave the most realistic interaction. If there was a large discrepancy it was found that the nodes on the upper surface fell through the lower surface. This caused the interaction's normal direction behaviour to be applied along the length of the rails, stopping the movement of the slide and causing the destruction of the sled.

Linear elements were used for both the shell and continuum elements. Although the use of quadratic elements theoretically increases the convergence of the finite element results, it also increases the memory necessary to find the solution. As there were very few curved surfaces in the model, the improved geometry description of the quadratic shape functions was not a benefit.

Although it would have decreased the computational expense, no reduced integration was used. Using reduced integration reduces the computational expense of performing the integration of the weak form of the partial differential equation. Thus can cause hourglassing of the elements, which is why it was not used.

5.2.3.1 MESH SIZE

The meshes used for each part in the model are shown next to their details in the blocks which follow. The convergence of the results was verified by refining the mesh of: the cross members, rail supports and the rails. As the refined mesh increased the already large computational expense of the model it was only run for the worst case scenario. The refinement was made by halving the size of the global element seeds of these parts.

PART: SLIDE	ELEMENT TYPE: C3D8: 3D CONTINUUM 8 NODED BRICK NUMBER OF ELEMENTS: 3360 STABLE TIME INCREMENT: 3,67 E-7 S MINIMUM EDGE LENGTH: 3,33 MM AVERAGE ELEMENT SIZE: 4,01 X 15 MM
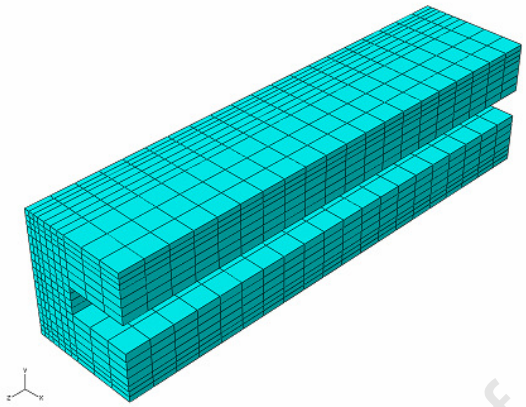	

PART: RAIL	ELEMENT TYPE: C3D8: 3D CONTINUUM 8 NODED BRICK NUMBER OF ELEMENTS: 3102 STABLE TIME INCREMENT: 6,15 E-7 S MINIMUM EDGE LENGTH: 4,12 MM AVERAGE ELEMENT SIZE: 4,12 X 38,5 MM
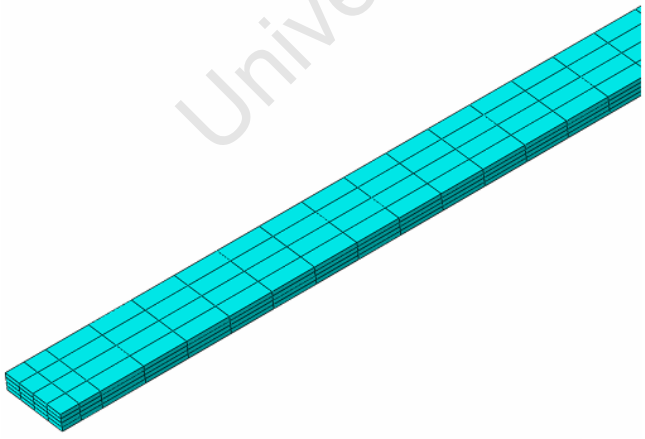	

PART: RAIL SUPPORT AND BRACES	ELEMENT TYPE: S4: A 4 NODED GENERAL SHELL NUMBER OF ELEMENTS: 13041 STABLE TIME INCREMENT: 6,75 E-7 S MINIMUM EDGE LENGTH: 2,27 MM AVERAGE ELEMENT SIZE: 16,9 X 21,5 MM

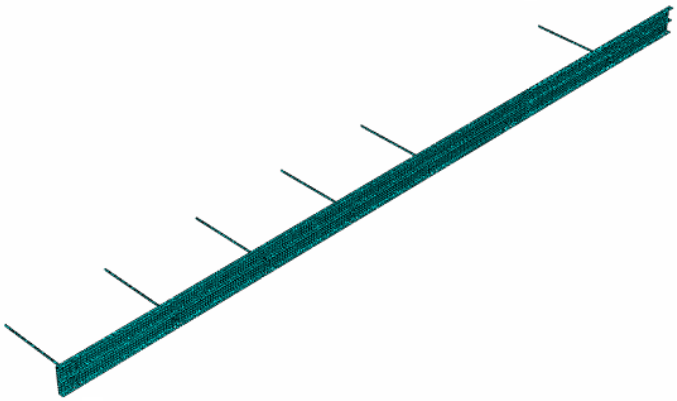

PART: CROSS MEMBER	ELEMENT TYPE: S4: A 4 NODED GENERAL SHELL NUMBER OF ELEMENTS: 1034 STABLE TIME INCREMENT: 5,65 E-7 S MINIMUM EDGE LENGTH: 3,60 MM AVERAGE ELEMENT SIZE: 21,5 X 29,7 MM

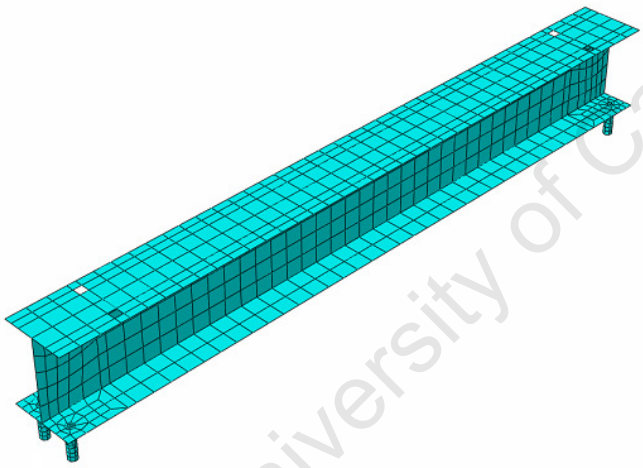

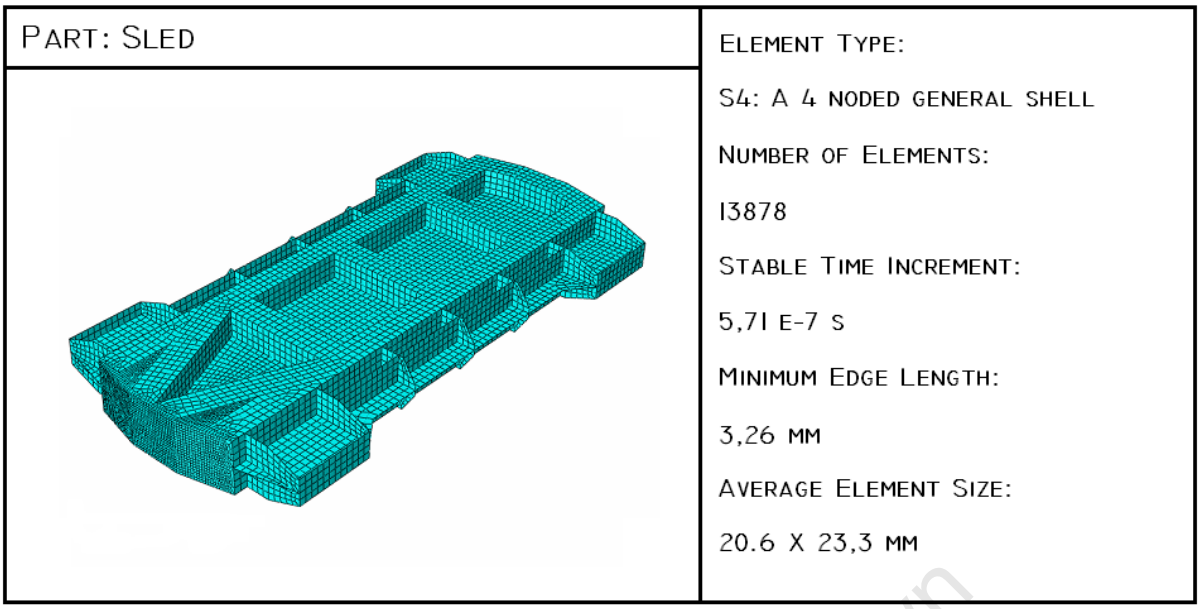

Notice the refinement of the mesh in the vicinity of the impact area in the front of the sled. This was done to better capture the effect of the deceleration stage loading.

5.2.3.2 SHELL ELEMENT NORMAL ORIENTATIONS

When using shell elements to create a finite element model, thicknesses need to be assigned to the elements. Where the material which makes up the element's thickness is in relation to the shell is described by the shell offset. The standard shell offsets in ABAQUS are: middle surface, top surface and bottom surface. These offsets are made relative to the shell normal, which assigns a positive and negative side to the shell.

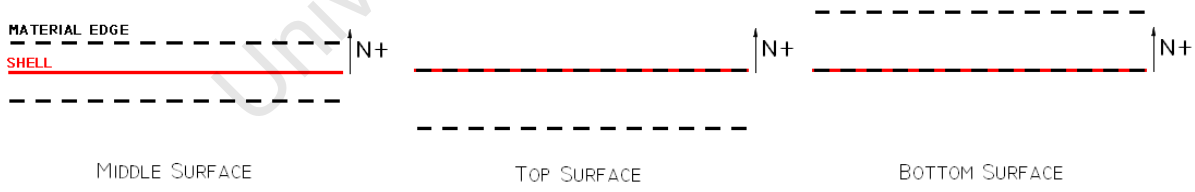

FIGURE 5-15: DEFINITIONS OF ABAQUS SHELL OFFSETS

In Figure 5-15 the differences between the three shell offsets are shown. The arrows marked N+ show the direction of the shell's positive normal. The dotted line represents the material thickness assigned to the shell, while the shell itself is shown by the red line.

Where a middle surface shell offset is used the direction of the shell normal has no effect. If one of the other offsets is used, the shell normal affects the overall dimensions of the part.

Incorrectly assigned normals can cause over-closures between part instances in an assembly where parts are in close proximity.

Middle surface offsets were used for all the shells except for those in the sled model and rod sections. Different offsets were used throughout the sled model making the orientations of the shell normals important. For the rod sections in the grounding bolts on the cross members and the braces between the rail supports: the same principle was used for all cases.

The principle used for the rod sections was to set the positive shell normal pointing outwards, away from the centre of the circular section. The shell offset was then set to be a top surface and the thickness set to be equal to the radius of the section. This resulted in a solid circular section being described.

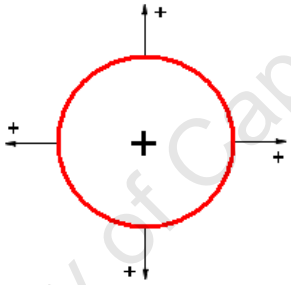

FIGURE 5-16: SKETCH OF NORMALS USED FOR CIRCULAR SECTIONS

In the model of the sled both middle and top surface offsets were used. The orientation of the shell normals, which were assigned top surface offsets, were important. In Figure 5-17 the direction of the shell normals are shown on the left and the assigned offset on the right. The normals and offsets are distinguished by the colours of the different shells.

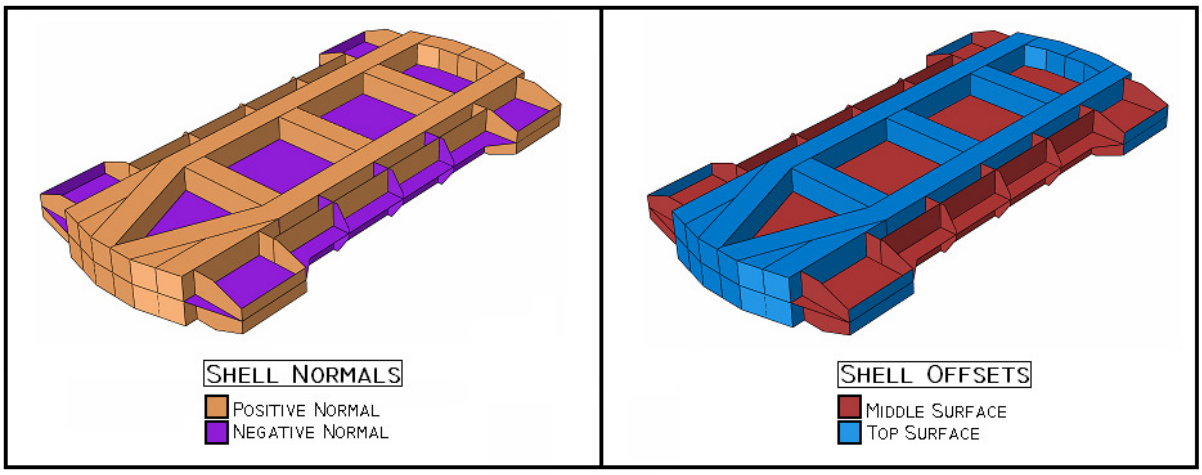

FIGURE 5-17: GRAPHICAL REPRESENTATION SHOWING THE SHELL NORMAL ORIENTATIONS AND SHELL OFFSETS

From Figure 5-17 its can be seen that the shell orientations are such that the material assigned to the shells was kept within the limits of the shells.

5.3 ASSEMBLY

The assembly of the model consisted of a number of instances of the each of the different parts. There were: 8 cross members, 2 rail supports, 2 rails, 4 slides and the sled.

The cross members were arranged perpendicularly to rail supports and bolt holes in the cross members aligned with their respective holes in the supports, see Figure 5-18 and Figure 5-19. The bolt holes made in the rail supports were made at the same intervals as in the physical supports.

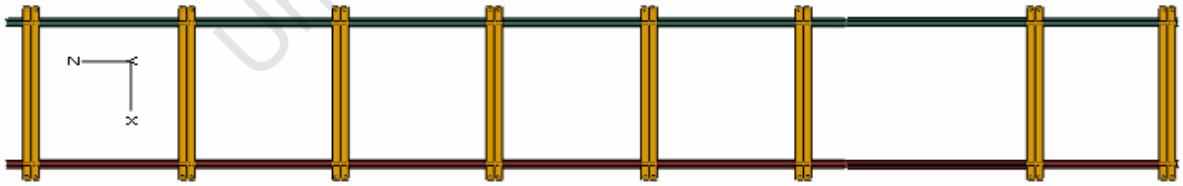

FIGURE 5-18: IMAGE OF LOCATIONS OF CROSS MEMBERS RELATIVE TO THE RAIL SUPPORTS

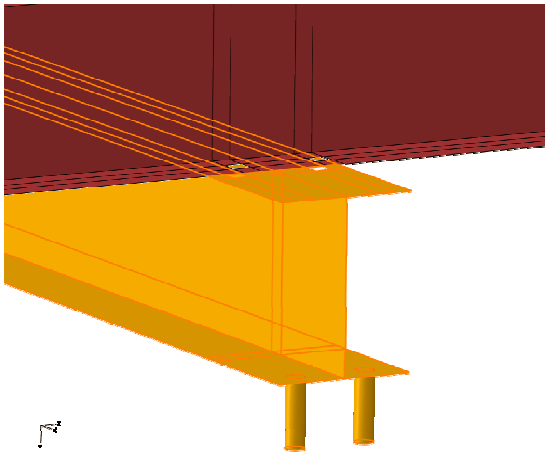

FIGURE 5-19: IMAGE SHOWING THE ALIGNMENT OF THE BOLT HOLES IN THE CROSS MEMBERS AND THE RAIL SUPPORTS

The rails were placed along the rail supports in such a way that the meshes, which had been manipulated to be identical, were aligned. The middle of the faces that were to be attached to the rail supports were aligned with the extruded mounting area as seen in Figure 5-20.

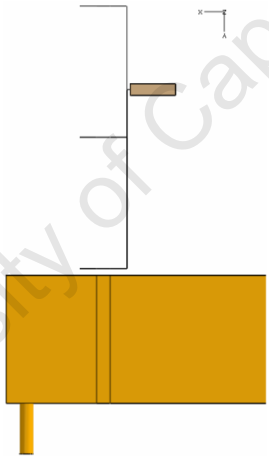

FIGURE 5-20: IMAGE OF SHOWING THE PLACEMENT OF THE RAILS RELATIVE TO THE RAIL SUPPORTS

The sled was positioned so that the rear end of the sled was in line with the beginning of the rails. Its vertical position was adjusted so that the rails were aligned with the middle of the sled. Finally the slides were abutted against their mounting points. This resulted in the rails fitting inside the slides. A view from the rear of the sled is shown in Figure 5-21.

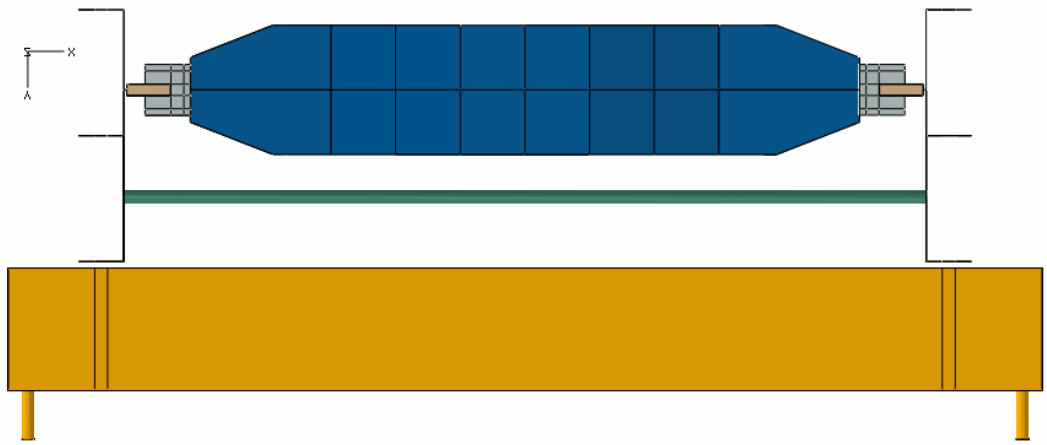

FIGURE 5-21: IMAGE SHOWING THE VERTICAL ALIGNMENT OF THE SLED, SLIDES AND RAILS

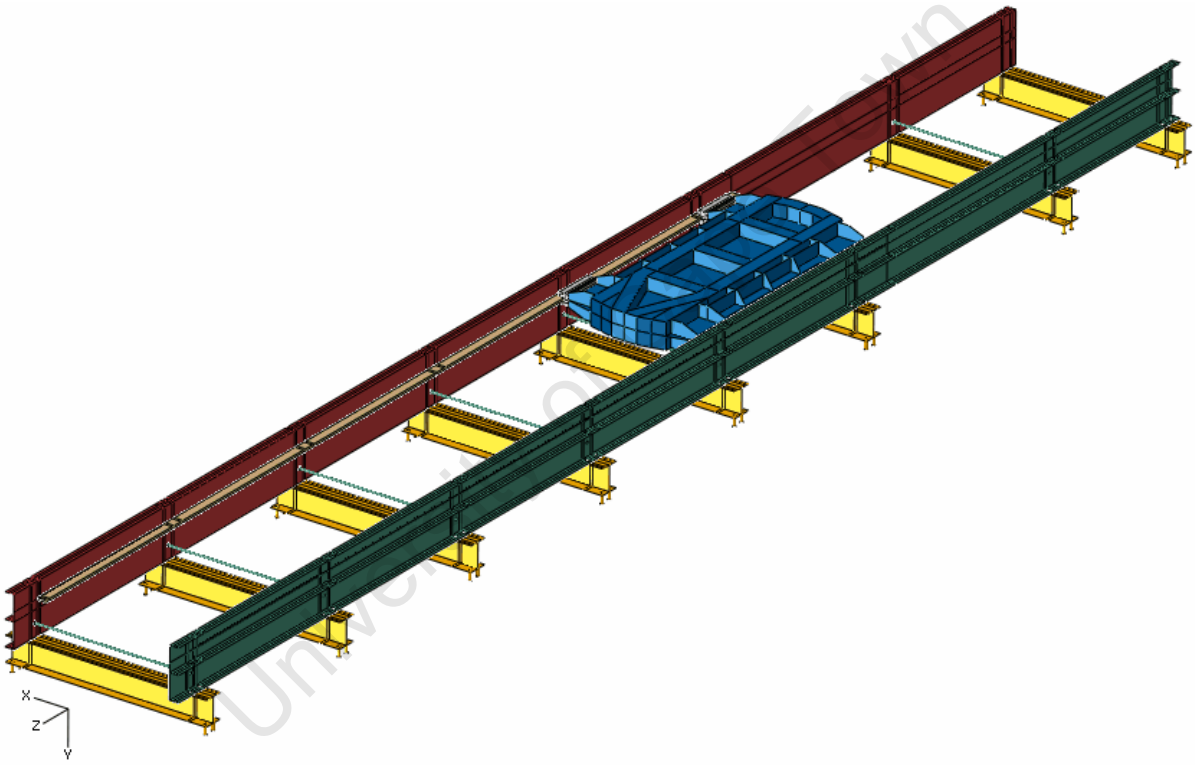

FIGURE 5-22: ISOMETERIC VIEW OF THE ENTIRE MODEL ASSEMBLY

In Figure 5-22 the entire assembled model is shown. Notice how the rails only begin at the third cross member from the rear. In the physical assembly, the pneumatic acceleration cylinder occupies the area behind the rails. The deceleration cylinder is mounted to a concrete block in front of the rail supports.

5.4 CONSTRAINTS

To model the connections between the different components a range of constraints were used. In the physical assembly, the different parts were bolted together. Depending on the number of bolts holding the components together the type of constraint to be used was chosen. Where many bolts were used and the pitch of the spacing was small, shell to solid couplings or tie constraints were assigned over the entire area of the connecting faces.

In the case of the cross member to rail support connections, there were only two bolts per connection. The bolt holes were cut in both components. To model the connections the edges of both holes were tied to each other. This method modelled the locality of the connections while still remaining computationally simple. The gap between the components was due to the shell thicknesses; the tie constraints accounted for these thicknesses. The constraints between the cross member and the rail support are represented by the small yellow circles Figure 5-23.

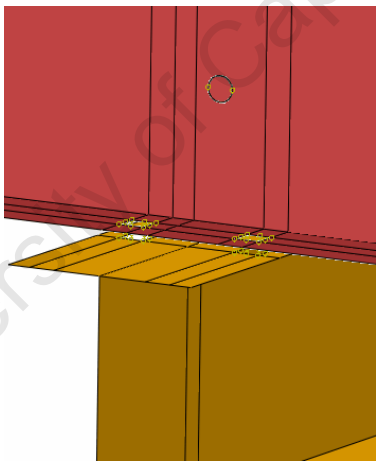

FIGURE 5-23: IMAGE SHOWING THE TIE CONSTRAINTS INVOLVING THE RAIL SUPPORTS

To connect the end of the braces to the right hand side rail support; a tie constraint was used. The circular sections were extruded from the face of the left hand side support, which meant the braces were already attached to this support. When fastened, the nuts on the ends of the threaded bar abutted the rail supports against the thick walled tubing of the braces. This provided a substantial connection between the rail supports and the braces. To model this connection a tie constraint was also used. The circular partition and the circle symbols representing the constraint, which connects the brace to the other side of the support, can be seen in Figure 5-23.

A shell to solid coupling was used to attach the rails to the rail supports. The physical rails were connected to the supports by over 75, M12 bolts spaced a maximum of 20 mm apart. The shell to solid coupling, coupled the shell element facets to the solid element facets within the position tolerance. By ensuring that at least two element facets in the longitudinal direction were within the position tolerance, the coupling transferred all rotations and displacement between the shell and solid elements. A photo showing the extent of the physical connection is given in Figure 5-24 below.

FIGURE 5-24: PHOTO SHOWING THE BOLTS ATTACHING A RAIL TO ITS SUPPORT

To be able to apply the loads created by the acceleration and deceleration stages, reference points were placed in the middle of both the areas which make contact with the pistons. These reference points were coupled to the impact areas using kinetic couplings. In a kinetic coupling all the elements in the coupling are treated as one; this affects the stress distribution in these elements. The coupling between the front impact area and the reference point, *RP-2*, can be seen in Figure 5-25.

A more realistic distribution is achieved using a distributed coupling. As the reference points did not have any mass assigned to them, distributed couplings caused an error. ABAQUS would assign an undisclosed amount of mass to the reference point to allow the solver to find a solution. As the simulation was highly dynamic this might have affected the results. For this reason kinetic couplings were used for the impact areas.

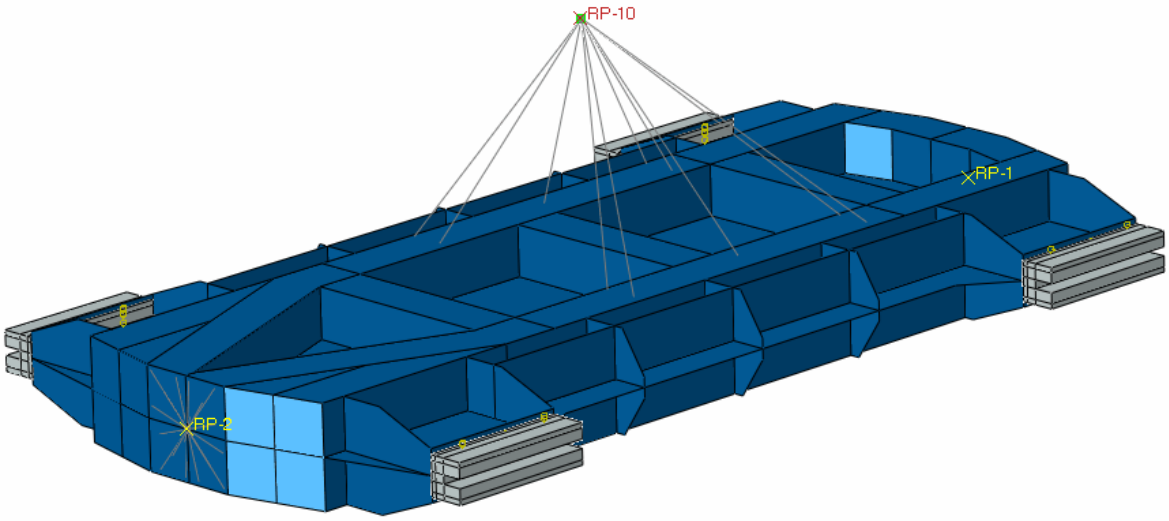

FIGURE 5-25: IMAGE SHOWING THE CONSTRAINTS INVOLVING THE SLED

To model the mass of the test specimen and its restraint system, a point mass was assigned to a reference point. The mass that was assigned was 109 kg, which was equal to the sum of the masses of a 50th percentile Hybrid III male dummy and the mass of a proposed restraint system. The mass was positioned at the combined centre of mass of the dummy and the restraint system. The reference point was placed over the middle of the sled, 433 mm above the top surface. To attach the point mass to the sled, a distributed coupling was used. As the reference point was assigned mass, the solver did not need to alter the mass to find a solution. The point mass was assigned to the reference point *RP-10* in Figure 5-25.

Finally the slides were tied to the sled's mounting points. The actual connection between the slides and the sled would have allowed for adjustments. As the method to be used for this was not known, a connection which could be modelled at a tie constraint was assumed. The yellow circle symbols show the tie constraint in Figure 5-25.

5.5 INTERACTIONS

To model the interaction between the slides and the rails, contact interactions between the relevant components needed to be created. The General Contact formulation was used to assign the contact properties. The formulation was more robust than the older surface-to-surface formulation. The more robust formulation was chosen initially when issues with the contact formulation were found. The issues resulted in the nodes of the upper slide's surface falling between the nodes on the rail's surface.

General Contact's default setting assigned the contact properties to any surfaces in the model whose nodes experience over-closure. This default was overwritten and contact pairs of the slides' inner surfaces and the relevant surfaces of the rails were created, resulting in the contact properties only being applied between these two contact pairs.

Contact was described by a combination of normal and tangential behaviours. The normal behaviour was set to Hard Contact. Separation of the surfaces after contact was allowed. In the tangential direction a penalty friction formulation was applied. The friction was described as isotropic with a friction coefficient of 0.25 – the reported friction coefficient between ERTACETAL C and steel(27).

5.6 BOUNDARY CONDITIONS

Only one boundary condition was used in the final model. An encastre condition was applied to the bottoms of all the grounding bolts to model the fact that they were chemically anchored into the concrete floor. An encastre condition fixes all the displacement and rotation degrees of freedom of the selected nodes to zero.

The grounding bolts were modelled by the circular sections, which were extruded from the bottom flange of the cross members. This boundary condition fixed the cross members in space, which through the constraints and interactions mentioned in sections 5.4 and 5.5 reproduced the same degrees of freedom as the physical model.

5.7 LOADING

For the predictions of the finite element simulation to relate to the physical dynamics of the system, loading which was as close to the actual loading of the sled needed to be applied to the model. One of the purposes of the Acceleration and Deceleration simulations was to use their outputs to load the finite element model.

The model could have conceivably been loaded in one of two ways. Either the predicted force exerted on the sled from both simulations could be applied to the sled at the correct time points, or the predicted sled velocities could be enforced. The pros and cons of both methods are discussed in section 5.7.1

In the final model, the sled was loaded using the forces exerted on the sled. The forces calculated in the acceleration stage simulation worked well, while a numerical anomaly in the deceleration stage force profile required an investigation into the forces created at impact. This investigation is discussed in section 5.7.2.

The finite element model was run for three scenarios. All the scenarios used the maximum acceleration force profile – resulting from all 12 acceleration valves being opened with the supply pressure set at 10 bar. Three different decelerating force profiles were simulated: an idealised 59g deceleration using a smooth step function; the force profile from the deceleration stage simulation ignoring the anomaly and a combination of the deceleration profile and the results of the impact investigation. Plots of the different loading profiles are shown in Figure 5-26 and Figure 5-27. Also plotted in Figure 5-27 is the force exerted by the hydraulic cylinder if the effective pressure was at 200 bar for the entire duration of the step.

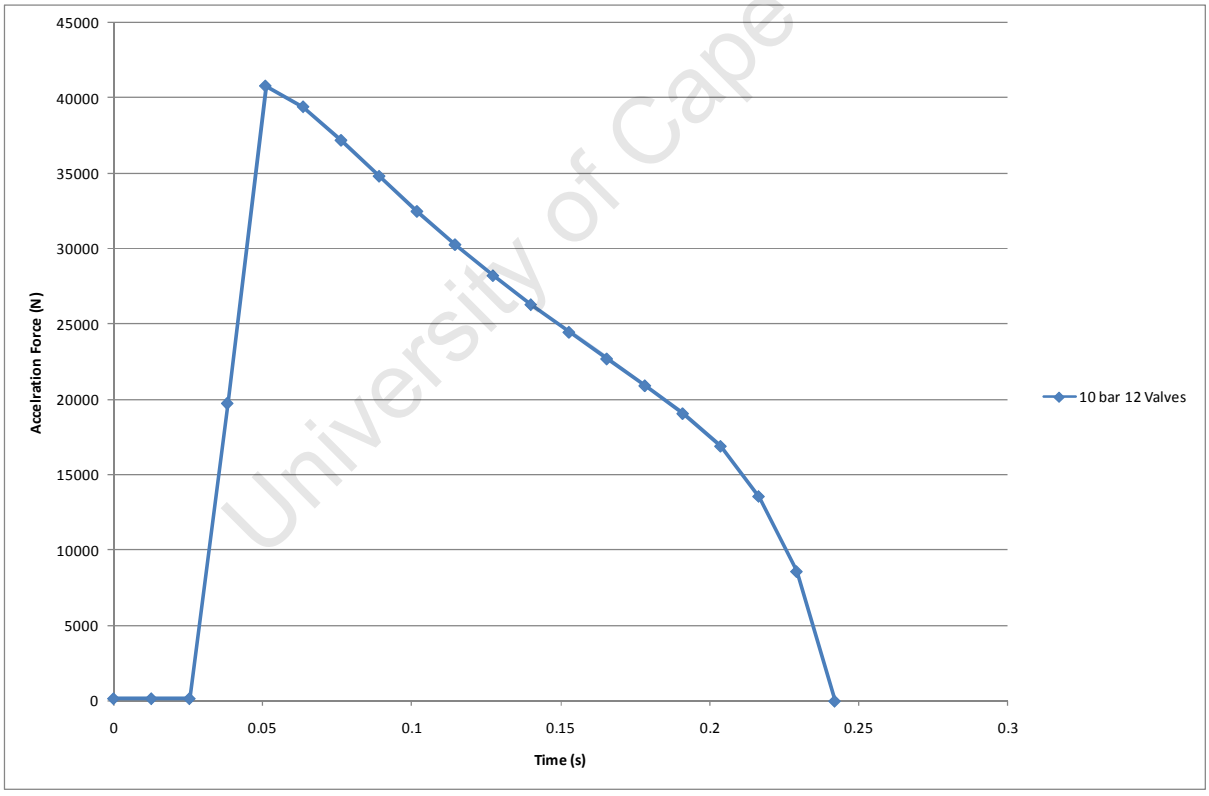

FIGURE 5-26: PLOT OF THE ACCELERATION FORCE PROFILE

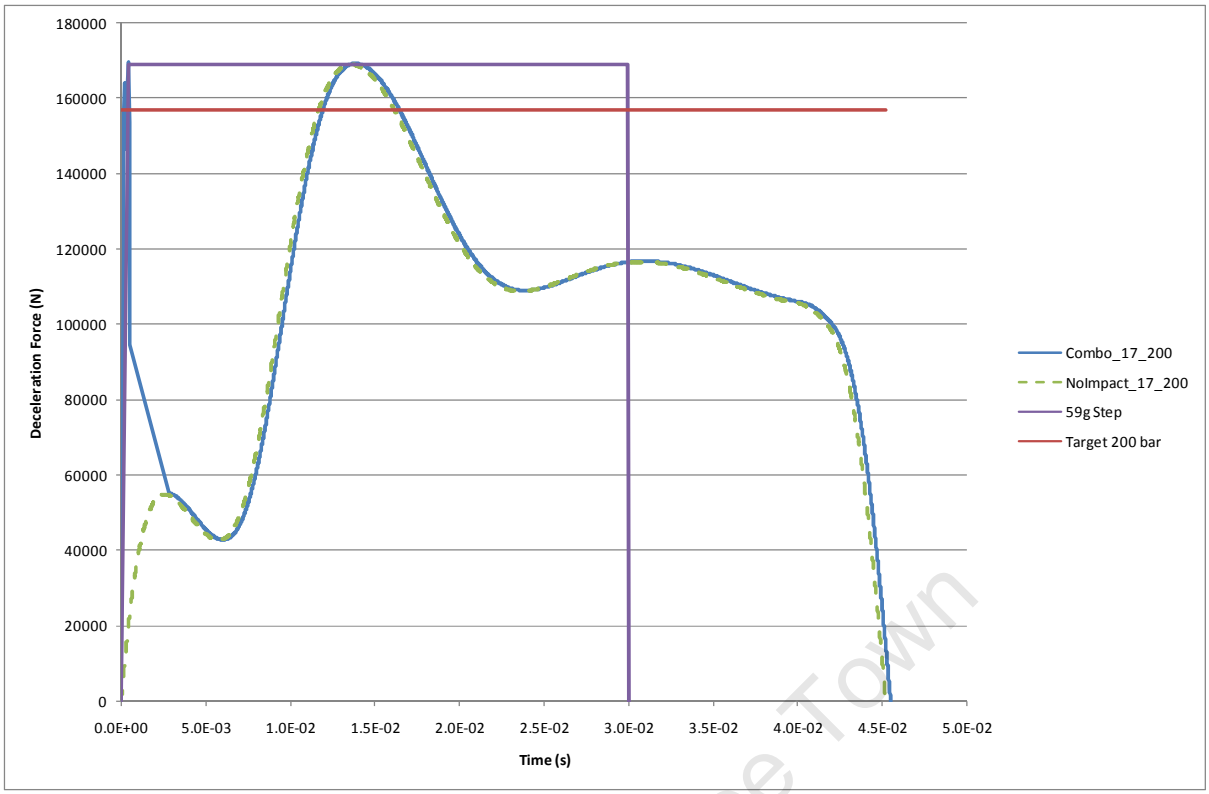

FIGURE 5-27: PLOT OF THE DIFFERENT DECELERATION FORCE PROFILES

The time domain of the finite element simulation was divided into three steps. The first, Step-1, was the same length as the domain of the acceleration load profile – the acceleration force profile was applied to the rear reference point over this step. Next, Step-2, the acceleration force was deactivated and the sled was allowed to coast along the rails to the point where the deceleration piston would have made contact with the sled – this duration had to be estimated using the equations of motion and then improved by trial and error. For the acceleration force profile shown in Figure 5-26 a duration of 0.1435 s resulted in the sled being in the correct position at the beginning of Step-3. Finally in Step-3, the deceleration force was applied to the front reference point – again the duration was determined by the domain of the force profile.

After the first model was run, changes were be made to the step times and the deceleration load profiles and the calculation restarted from a point in the simulation before the changes had an effect. This allowed a considerable amount of time to be saved when finding an appropriate duration for Step-2 and altering the deceleration profile in Step-3.

Mass scaling was considered to increase the stable time increment of the simulation and thus reduce the run time. However, due to the dynamic nature of the problem it was feared that the increase in density would significantly affect the inertial forces and hence the system's dynamics.

5.7.1 LOADING USING A VELOCITY BOUNDARY CONDITION VS FORCE

As mentioned above the loading to the system could have either been applied by a velocity boundary condition or a force. Initially it was thought that specifying the velocity would be the better option, as it was easier to extract the sled velocities from the deceleration stage simulation. Due to a number of issues (detailed below) it was found that loading the system using a force would be much more successful. The root of these issues lay in the way the different loading methods were enforced.

In both of the methods the loading was applied to the reference points coupled to the piston contact areas. The force was applied as a concentrated force, the magnitude of which was controlled by an amplitude. Similarly, the velocity was also controlled by an amplitude, but applied as a boundary condition as opposed to a load.

When the loading was described using the velocity method the sled was completely destroyed during the acceleration stage. The deformations were so extreme that the solver aborted the simulations. This was not realistic as the loading during the acceleration stage was relatively low and the only opposing force was due to the low friction contact between the rails and slides.

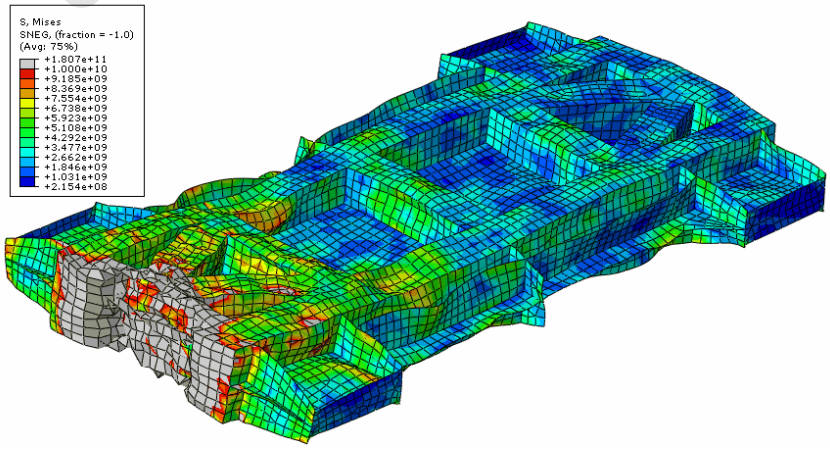

FIGURE 5-28: IMAGE OF THE SLED DURING THE ACCELERATION STAGE WHEN USING A VARYING VELOCITY BOUNDARY CONDITION

Velocities are constrained boundary conditions. This means that the displacements of the nodes assigned to the condition are not solved for, but enforced. Forces on the other hand are unconstrained boundary conditions. Their effect is accounted for by adding them to the force vector before the displacements are solved for a particular time step. The displacements of the nodes where the force is applied are not enforced to any value; their values are determined by the solver.

Although the friction coefficients between the slides and the rails in both the acceleration stage simulation and the finite element model were the same, the acceleration stage simulation assumed perfect contact between the slides and the rails at all times. In the finite element model the contact was much more realistic as the slides could move around. As a result the friction force would not be exactly the same in both cases. Due to this, the sled dynamics would not be identical in both models.

The constrained boundary condition enforced the displacements of the piston contact area nodes, which resulted in unrealistic deformations of the sled structure. The unconstrained force boundary conditions were much more accommodating as the displacements of the nodes were solved for while accounting for the applied force, structure stiffness and frictional damping. This gave a realistic result of the sled moving along the rails.

5.7.2 DECELERATION STAGE NUMERICAL ANOMALY

Once the deceleration force had been extracted from the Deceleration Stage simulation, the profile was plotted and analysed. It was found that at the moment of impact there was an extremely large spike in the force profile. Initially the spike was thought to be caused by a mismatch in the sled and piston velocities. This hypothesis was supported by a sudden drop in the sled velocity at the same moment.

On closer analysis it was decided that this could not be true. The extremely large magnitude and incredibly short duration of the spike were signs that it could have been caused by a numerical anomaly. A logarithmic plot of the deceleration force profile from the deceleration stage simulation is given in Figure 5-29. In order to deduce that this was in fact the case some auxiliary models were made.

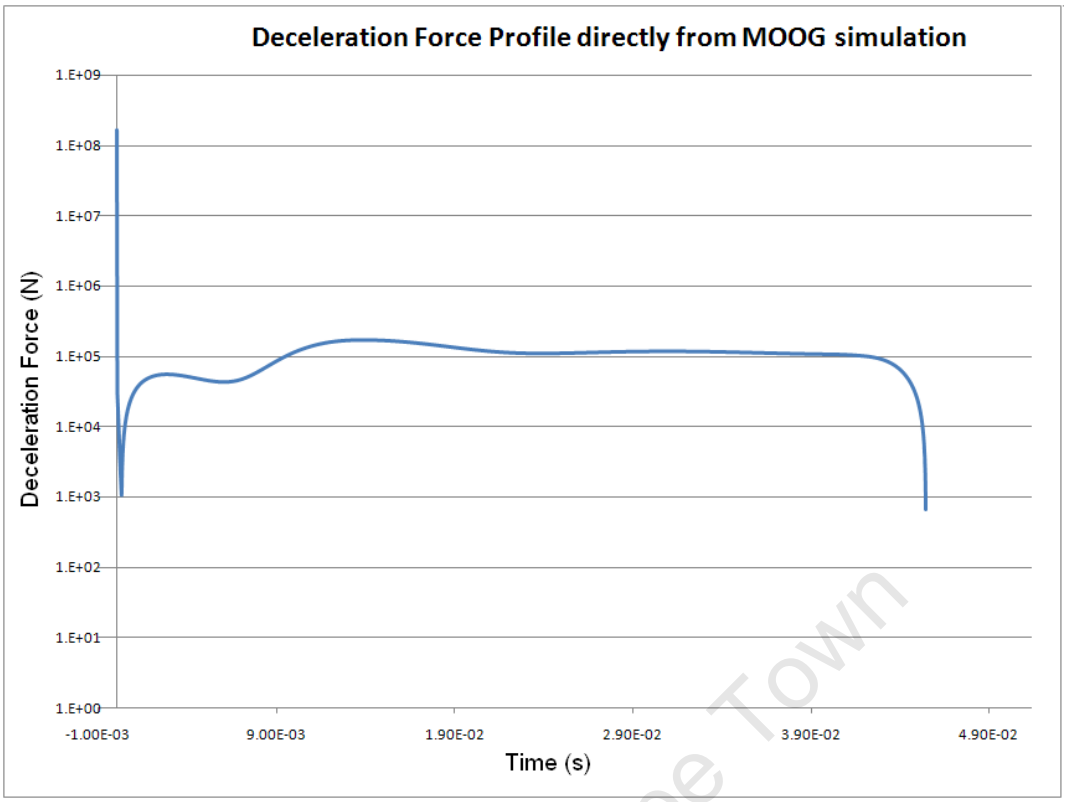

FIGURE 5-29: PLOT OF THE DECELERATION FORCE PROFILE DIRECTLY FROM THE DECELERATION STAGE SIMULATION

A model to address the extremely large magnitude of the spike was created in ABAQUS. The sled model was constrained by boundary conditions that imitated the rails and was given an initial velocity. By describing the contact between the impact area and the object which was impacted, the stresses created by the impact could be calculated.

The sled was made to collide with: a rigid surface; a model of the piston whose end displacement was fixed and a model of the piston connected to a spring which accounted for the bulk modulus of the oil. Impact velocities of 3 and 17 m/s were modelled. 3 m/s was the predicted drop in the sled velocity at the moment of impact. 17 m/s was the nominal maximum impact velocity. The plot in Figure 5-33 show how the force profiles change as impact velocity and the object are varied.

The value of the spring constant was taken to be the no flow stiffness of the cylinder at the operating point. The no flow stiffness was described in the deceleration systems documentation as: the equivalent spring stiffness of the oil in the cylinder if both chambers were sealed by their valves(1). The formula for the no flow stiffness is given in Equation 2-1. A derivation of the equation is given in Equation 5-3.

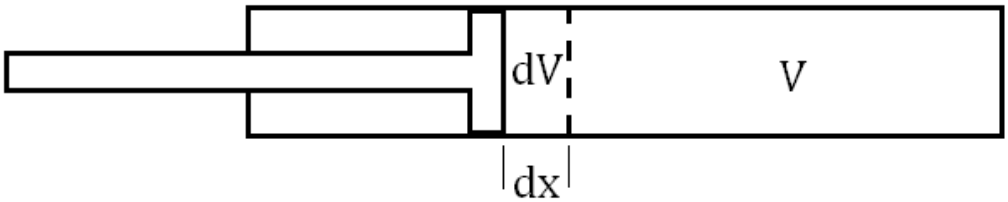

FIGURE 5-30: SKETCH DESCRIBING VARIBLES USED IN THE DERIVATION

EQUATION 5-3:

$$\delta V = A\delta x$$

$$\delta x = \frac{\delta V}{A}$$

$$\beta = V\frac{\delta P}{\delta V}$$

$$\Rightarrow \delta P = \beta\frac{\delta V}{V} = \beta\frac{A\delta x}{V}$$

$$\delta F = \delta P \times A = \beta\frac{A\delta x}{V} \times A = \beta\frac{A^2}{V}\delta x$$

$$\frac{\delta F}{\delta x} = K = \beta\frac{A^2}{V}$$

$$for\ two\ chambers\colon\ K = \beta\left(\frac{A_a^2}{V_a} + \frac{A_b^2}{V_b}\right)$$

When calculating the stiffness it is important to include the addition volumes for each chamber. Additional volumes include the volume of oil in the cavities of the end caps and the volume of oil in the pipe leading to the valves.

So as to be comprehensive, a spring mass model was programmed into MatLab to try and reproduce the spike seen in the deceleration stage model. A point mass of 300 kg was attached to a spring and dashpot with the same constants as the rubber. The other ends of the spring and dashpot were fixed. The mass was given an initial velocity of 17 m/s and the resulting force plotted. Figure 5-31 shows the spring mass system that was modelled.

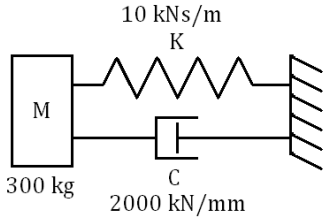

FIGURE 5-31: SCHEMATIC OF THE SPRING MASS MODEL

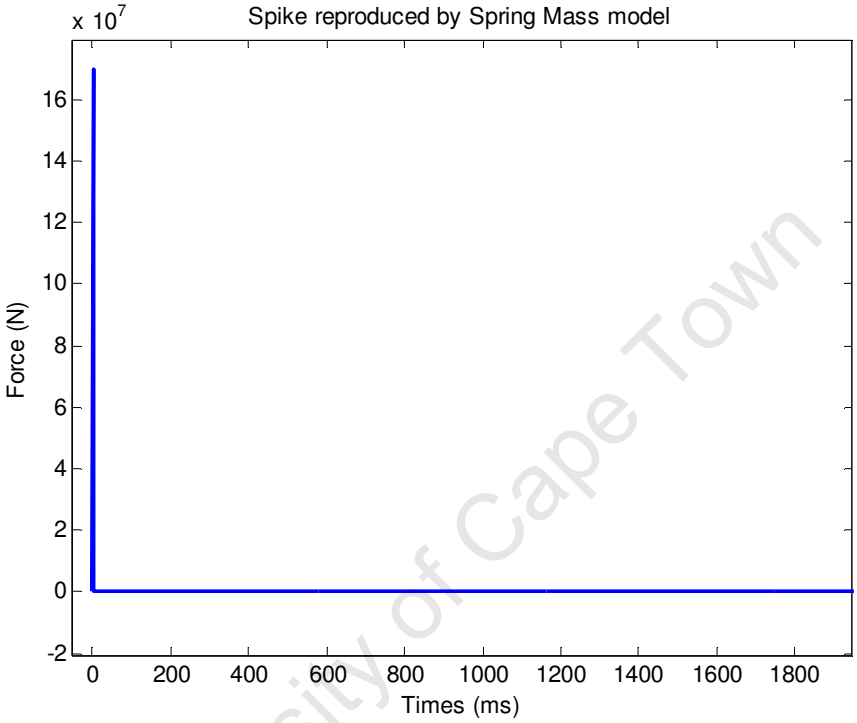

FIGURE 5-32: PLOT OF THE REPRODUCTION OF THE 170 MN SPIKE CREATED BY THE SPRING MASS MODEL

From Figure 5-32 the spike in the force profile can be seen. The reproduced spike has the same magnitude as well as a similar duration. The spike was removed from the results by reducing the value of the spring and damping constants; the expected decaying oscillation result then being seen. These results suggested that the spike could be removed by reducing the time step below some critical value; no practical time step would remove the spike. This confirmed that the spike was indeed a numerical anomaly and it could be disregarded.

The discussion that follows, details how the initial contact of the sled with the piston was dealt with using the auxiliary simulations.

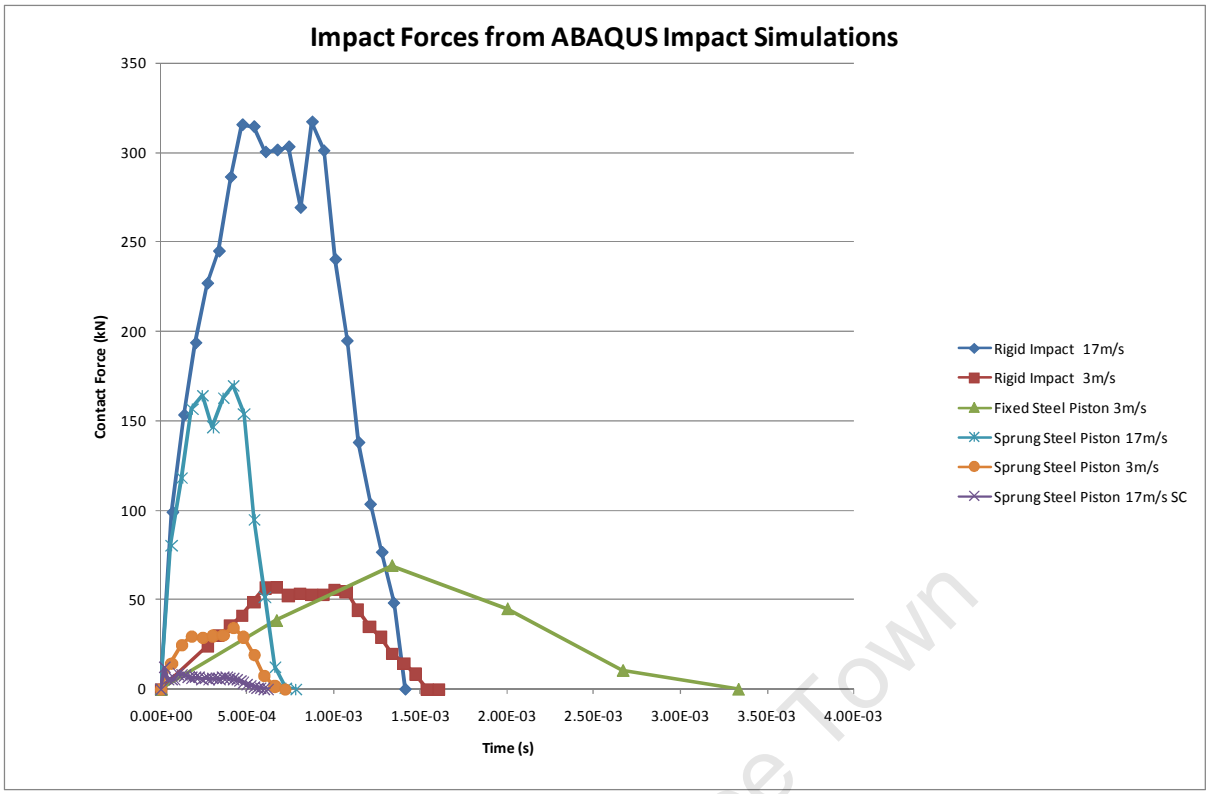

FIGURE 5-33: PLOTS OF THE IMPACT FORCE PROFILES FROM THE IMPACT SIMULATIONS

From the results of the auxiliary simulations it can be seen that the maximum peak force would occur if the sled collided with a rigid surface at 17 m/s. This peak value of 300 kN is over 500 times smaller than the spike predicted in the Deceleration Stage model. The duration of the peak is 70 times longer than the Deceleration Stage model.

Notice in Figure 5-33 that as the impact object becomes more like the physical piston the impact forces decrease. When the rigid surface was replaced with a model of a steel piston which accounted for the bulk modulus of the oil, the peak was 170 kN. Finally the peak forces were reduced to an insignificant level when the rubber stopper was accounted for. This was simply accounted for in the contact definition. Instead of using hard contact, soft contact was used. The spring and damping constants given by MOOG in the Deceleration Stage simulation were used to describe the soft contact.

The two impact simulations that were of most interest were those marked *Sprung Steel Piston 17m/s* and *Sprung Steel Piston 17m/s SC*. Both of these simulations had impact velocities of 17m/s and accounted for the compressibility of the oil by constraining the piston model with a spring. The difference between the two simulations was that the

Sprung Steel Piston 17m/s SC model used a soft contact interaction, which modelled the rubber stopper. The inclusion of the stiffness and damping of the rubber stopper reduced the impact force to an insignificant level.

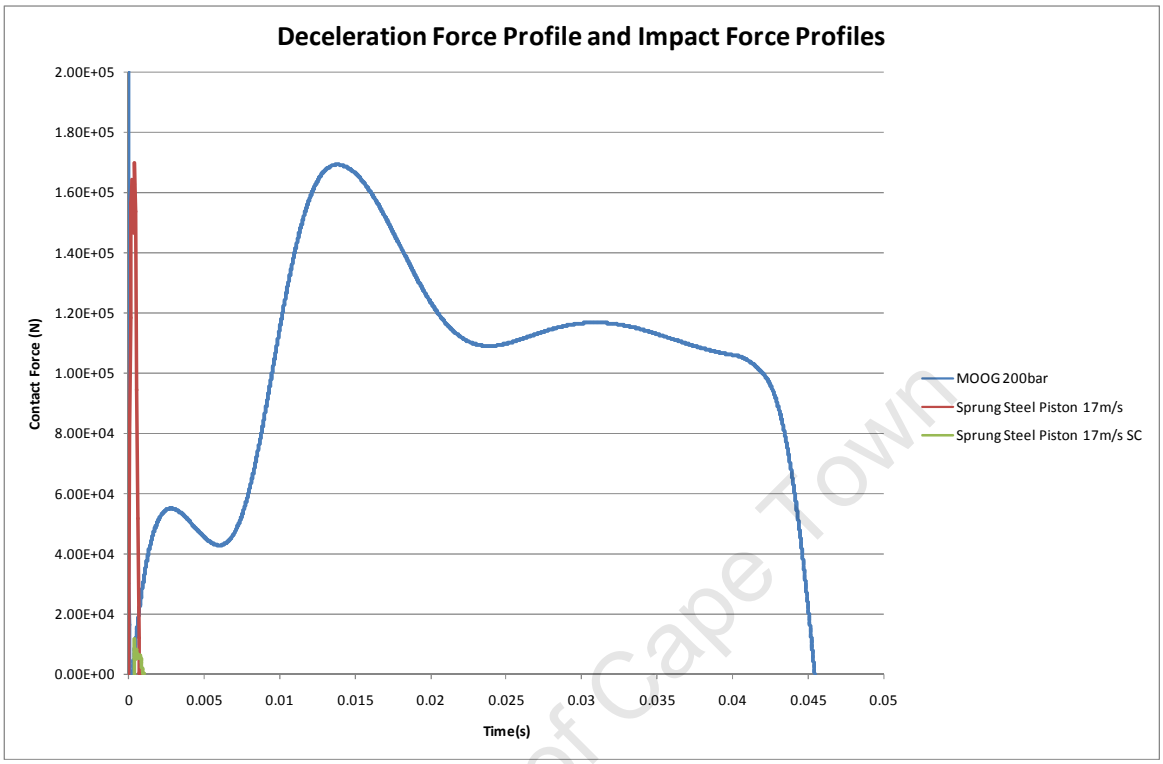

FIGURE 5-34: PLOT OF THE DECELERATION STAGE MODEL FORCE PROFILE OVERLAYED WITH THE IMPACT SIMULATION RESULTS

By combing the *Sprung Steel Piston 17m/s* and the *MOOG 200bar* curves from Figure 5-34, the force profile marked as *Combo_17_200* in Figure 5-27 was created. When looking at the curve for the impact simulation which included the rubber stopper, *Sprung Steel Piston 17m/s SC* in Figure 5-34, it can be seen how the force profile remains below the prediction from the Deceleration Stage simulation. Instead of combining these curves the spike was merely removed from the curve marked *MOOG 200bar*. This is plotted in Figure 5-27 as the *NoImpact_17_200* curve.

The *Combo_17_200* curve gave a worst case scenario for the 200 bar set point pressure, while the *NoImpact_17_200* curve gave the probable case if the constants describing the rubber stopper were correct. One other curve was also created. As the deceleration system was meant to be capable of decelerating the sled at 59g; a step function marked as *59g_Step* in Figure 5-27, was created and used to model a worst case scenario. The results of these load profiles are presented in the section 6.3.

6 RESULTS AND ANALYSIS

Data describing the dynamics of the sled during the acceleration and deceleration stage were collected from all the simulations that were run. This data was used to create the loading profiles used in the finite element model of the system.

Firstly, the data collected from the Acceleration Stage simulation was analysed. The trends relating to the effects of the input parameters were shown as well as typical plots of the data from selected simulations.

The results from the Deceleration Stage simulation were then shown. The predicted decelerations from different set point pressures were plotted. Again the typical plots of the output data were shown.

Finally the results of the finite element analysis were shown. These included: the eigenmodes of the rails system and the sled; maximum stresses in the system; deflections of the rails and their supports and highlighting of area containing design issues.

6.1 ACCELERATION STAGE SIMULATION

Select data calculated during the Acceleration Stage simulation was captured and plotted to describe the cylinder dynamics with respect to the input variables. This data included: chamber pressure and piston velocity histories as well a piston velocity vs. stroke plot. The profiles of the plots for the different input parameters had similar profiles, while the magnitudes varied. For this reason plots for all the combinations have not been included.

The time histories of the chamber pressures are shown in Figure 6-1. From the green line the pressure history of the rear chamber, which exerts a force in the acceleration direction, can be analysed. The delay in the pressure rise at the beginning of the simulation is due to opening transients of the valves. Once open the pressure rises rapidly.

The gradient of this rise is affected by the initial volume of the rear chamber. When the initial volume is too close to zero, numeric problems arise. The pressure rises extremely quickly as a result of the diminished volume. Depending on the time step this can lead to an over estimation of the pressure. For this reason the dead volumes of the cylinder were calculated as described in section 4.2.

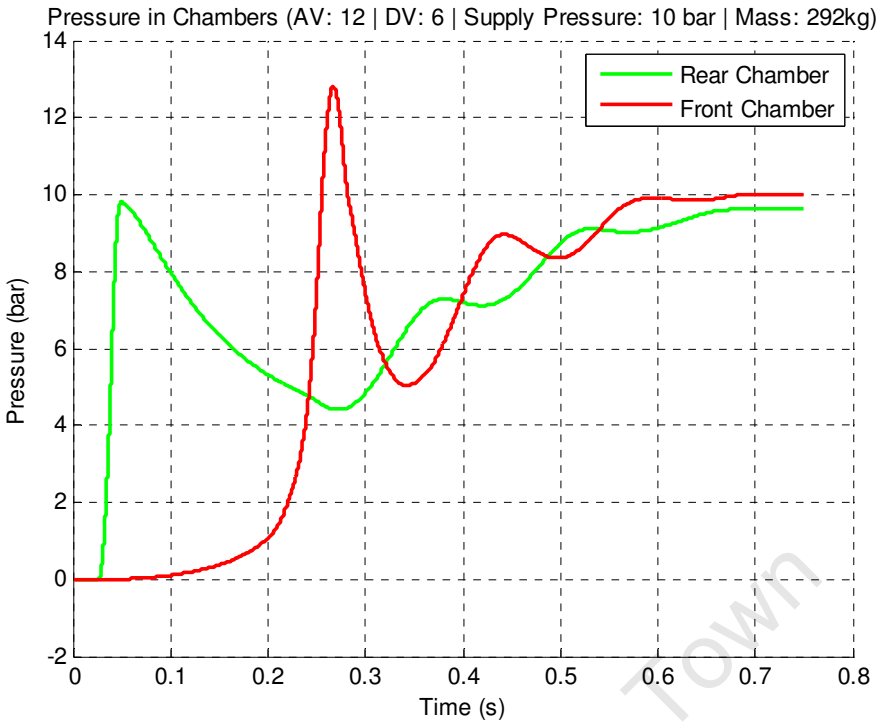

FIGURE 6-1: PLOT OF PNEUMATIC CHAMBER PRESSURES HISTORIES FOR THE MAXIMUM VELOCITY SIMULATION

The rear chamber pressure then decreased until the cushioning air had taken effect. The red line shows the pressure history of the front chamber. The pressure increases slowly due to the reduction of the chamber's volume as the piston extends. At the point at which the cushioning valves are opened this gradient increases due to the mass flow into the chamber.

The peak pressure in the front chamber is higher than the supply pressure. This is due to the movement of the piston compressing the air. The pressure can be seen to decrease once the velocity of the piston changes direction by comparing the peaks of Figure 6-1 to Figure 6-2. At this point in time the pressure in the rear chamber starts to increase. Both the pressures oscillate as the velocity of the piston causes the volume of the different chambers to change.

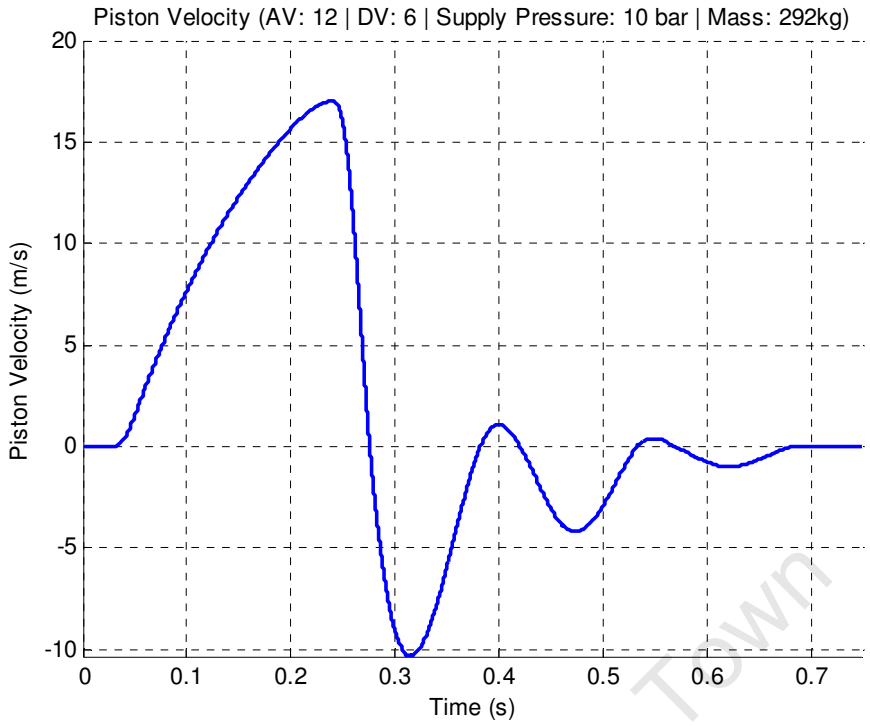

FIGURE 6-2: PLOT OF THE PISTON VELOCITY HISTORY FOR THE MAXIMUM VELOCITY SIMULATION

Finally the piston comes to rest. The pressure in the rear chamber is less than the front chamber. This is a result of sealing the rear chamber at the same time as activating the cushioning air. After the oscillations have dissipated, the piston comes to rest with an equal force being exerted on either side of it.

If the rear chamber was not sealed it would have reduced the effectiveness of the cushioning air and the piston would not have come to rest. Eventually the pressures in the two chambers would have become equal. As a larger piston area was exposed to the pressure in the rear chamber, there was a larger force pushing the cylinder forward.

The purpose of the cushioning air is to avoid impact of the piston with the end cap. Although the piston was fitted with a stroke cushioning device as shown in Figure 2-8 the piston velocities were so large that the suppliers specified the need for additional cushioning to be supplied via the cushioning air. The effectiveness of the cushioning air is seen in Figure 6-3. For this simulation the cushioning air was activated at 1.5 m. The red dotted line represents the full stroke of the cylinder. Notice that the piston remains well away from the end cap at the end of the stroke.

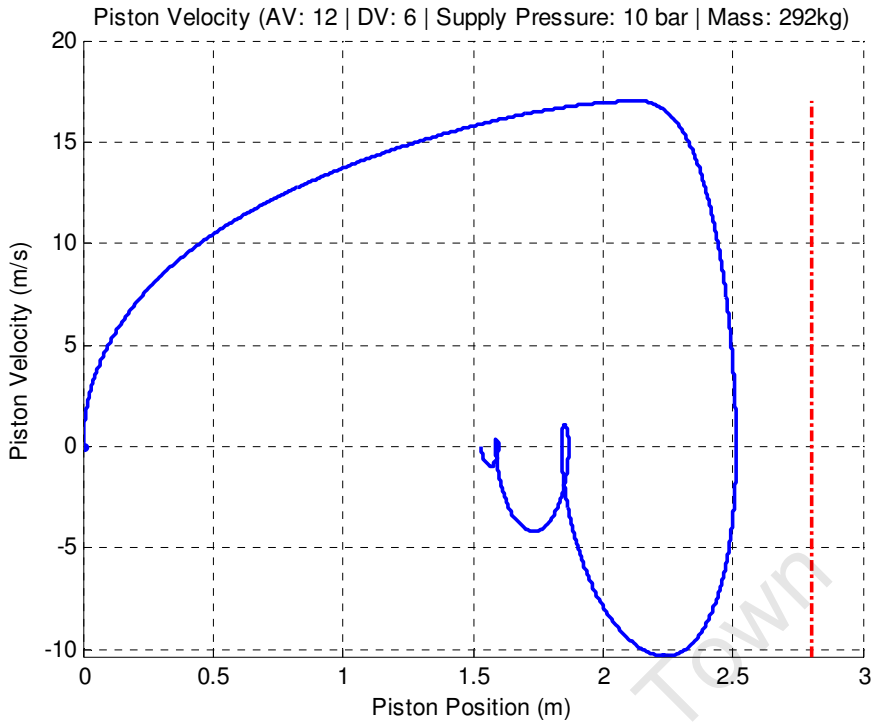

FIGURE 6-3: PLOT OF THE PNEUMATIC PISTON VELOCITY VS STROKE FOR THE MAXIMUM VELOCITY SIMULATION

On the other hand if no cushioning air was used the piston would collide with the end cap. Repeated collisions of the piston and the end cap would cause damage to both components, reducing their usable life. A simulation was run where the cushioning air valves remained in their off positions – exhausting the gas in the front chamber to the atmosphere. The velocity stroke plot is given in Figure 6-4.

While the maximum velocity increases slightly, the piston only decelerates once very near the end of the stroke. This deceleration is caused by the choking of the exhausting gas flow through the cushioning valves, which causes an increase in the front chamber pressure and a decrease in the piston velocity. The decrease in piston velocity caused by the flow choking was not sufficient. From the plot in Figure 6-4 the impact of the piston with the end cap is represented by the point where the red and blue lines meet. The impact velocity in this case was 4.7 m/s. Collisions like this one would have damaged the end cap and piston if they occurred in the physical cylinder.

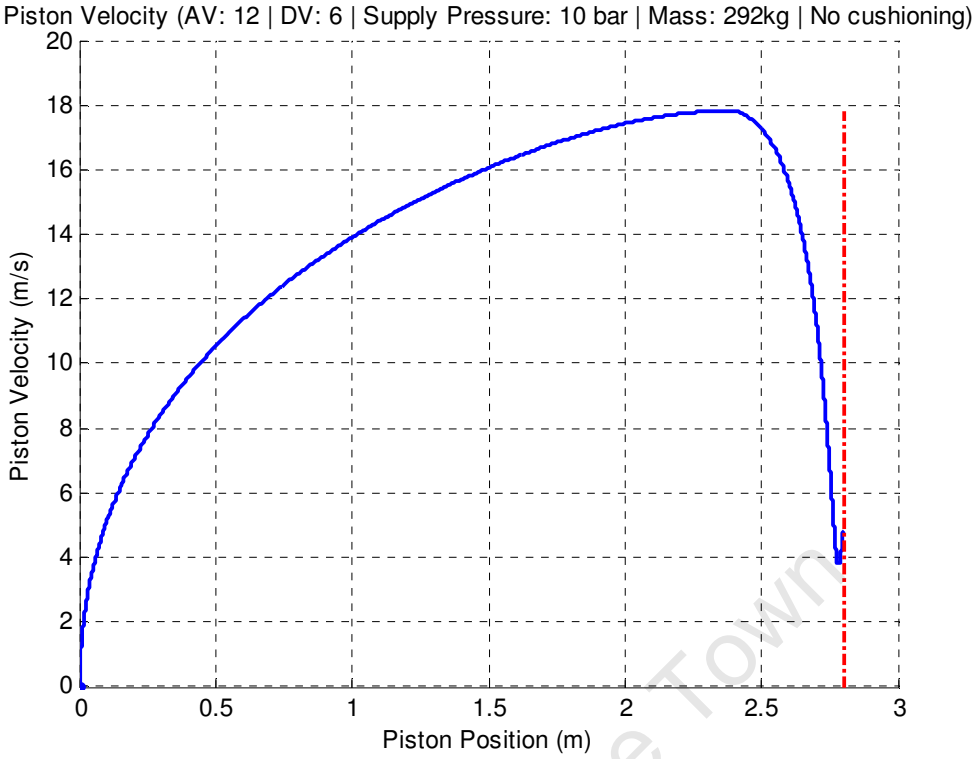

FIGURE 6-4: VELOCITY VS STROKE PLOT IF NO CUSHIONING AIR IS USED.

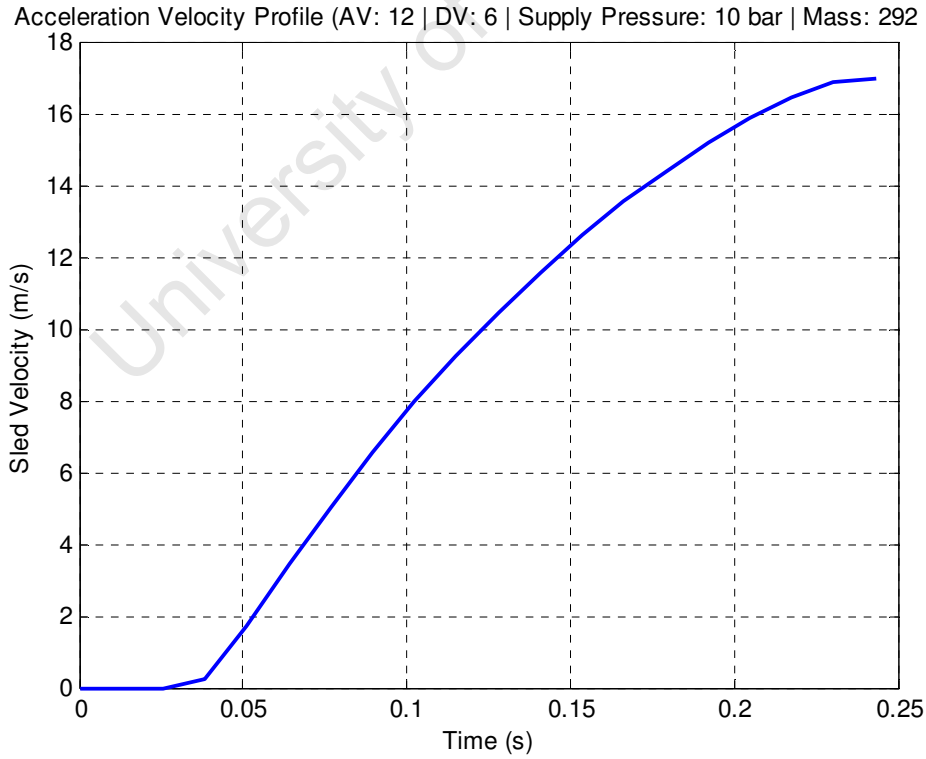

FIGURE 6-5: PLOT OF THE SLED VELOCITY HISTORY FOR THE MAXIMUM VELOCITY SIMULATION

While the dynamics of the piston were important in assessing the suitability of different test conditions, another important aspect was to estimate when the sled would be released.

This estimation was made by the addition code written to extract the tabular data for use in the finite element model. Figure 6-5 shows the sled's acceleration stage velocity profile which was extracted from the same simulation as the profile in Figure 6-2. The estimation captures the velocity up to the point where there piston starts to slow down, as the sled velocity.

The values of the input variables for maximum velocity are a supply pressure of 10 bar and the opening of all 12 acceleration valves. A table of the maximum velocities for different combinations of supply pressure and acceleration valves for a sled mass of 292 kg is shown in Table 6-1. 292 kg was the mass of the final sled concept, 50th percentile dummy and restraint system.

TABLE 6-1: TABLE OF MAXIMUM SLED VELOCITIES FOR COMBINATIONS OF INPUT VARIABLES

		No. of Valves			
	m/s	12	9	6	3
Supply Pressure (bar)	10	17.39	15.91	13.74	10.17
	8	15.60	14.30	12.36	9.08
	6	13.49	12.40	10.74	7.80
	4	10.87	10.04	8.71	6.20

A three dimensional surface was plotted using these values to show the effects of the input parameter graphically, shown in Figure 6-6. This surface was created by using linear interpolation to find the velocities for points between the values in Table 6-1. Not shown by the surface plot is the fact that fractions of valves cannot be used.

The interpolation was found to give good estimations of the final velocities when populating Table 6-2. Simulations were run using the estimations to ensure that they were accurate; the input parameters were then tuned to give even better results.

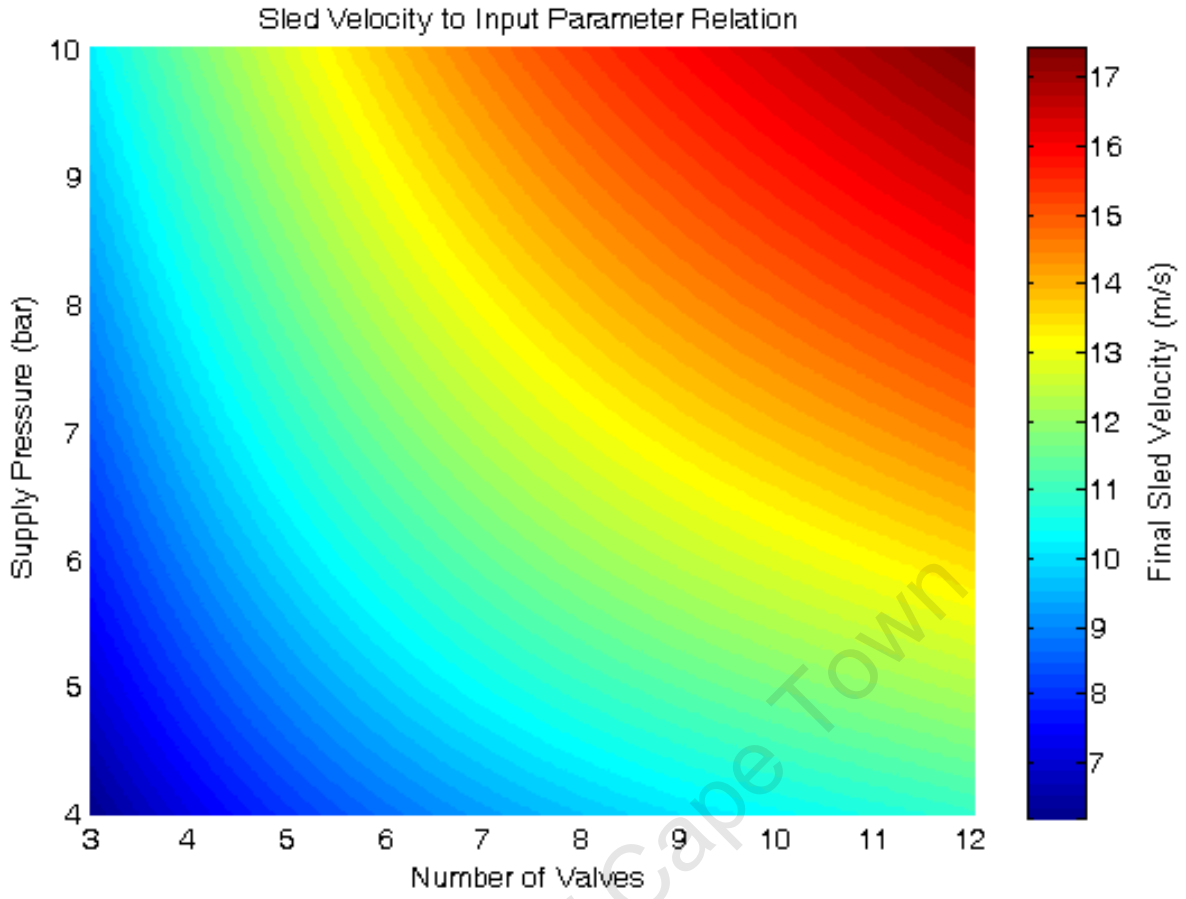

FIGURE 6-6: SURFACE PLOT SHOWING THE EFFECT OF THE INPUT PARAMETERS ON THE FINAL SLED VELOCITY

TABLE 6-2: EXAMPLES OF INPUT PARAMETER SETS WITH SIMILAR FINAL SLED VELOCITIES

Nominal Velocity: 8 m/s			Nominal Velocity: 10 m/s		
Valves	**Pressure (bar)**	**Velocity (m/s)**	**Valves**	**Pressure (bar)**	**Velocity (m/s)**
3	6.32	8.02	3	9.70	10.02
6	3.45	8.04	6	5.27	10.05
Nominal Velocity: 12.4 m/s			**Nominal Velocity: 15 m/s**		
Valves	**Pressure (bar)**	**Velocity (m/s)**	**Valves**	**Pressure (bar)**	**Velocity (m/s)**
6	8.00	12.36	8	9.60	14.99
9	9.00	12.40	9	8.86	15.02

From the plot and table it is seen that similar sled velocities could be achieved by various combinations of supply pressure and the number of valves opened. The differences between the velocity profiles of two tests which gave similar final sled velocities were investigated. The tests chosen for the investigation were: Supply Pressure = 6 bar, with 9 valves; and Supply Pressure = 8 bar, with 6 valves. The tests gave final sled velocities of: 12.40 m/s and 12.36 m/s respectively.

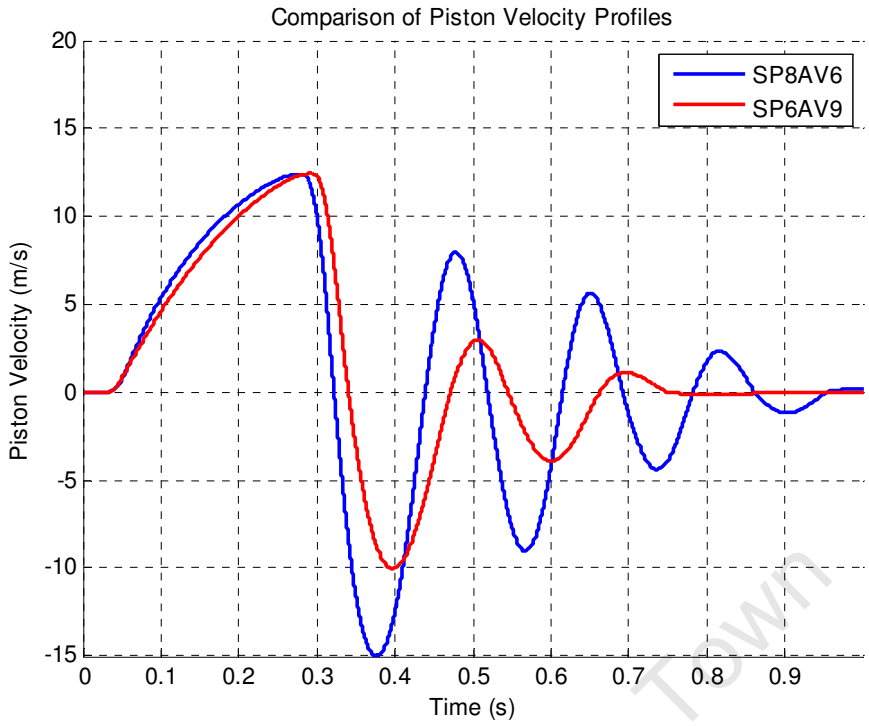

FIGURE 6-7: COMPARATIVE PLOT OF VELOCITY HISTORIES FOR SIMULATIONS WITH SIMILAR FINAL SLED VELOCITIES

From Figure 6-7 the first peak of both the curves can be seen to be similar to each other. The red line, representing the simulation with a supply pressure of 6 bar and opening 9 of the 12 acceleration valves, shows the piston velocity reaching its peak after the higher pressure simulation. The oscillations of the piston are also seen to decay faster, meaning that the piston comes to rest quicker than the higher pressure simulation.

This suggests that if faced with the choice between two sets of input parameters, the set which utilises the most acceleration valves should be used. The average acceleration over the acceleration stage would be slightly lower, leading to the longer acceleration time. The magnitude and duration of the oscillations in the piston velocity would also be reduced. The extent of the reduction of the piston position oscillation is shown in Figure 6-8.

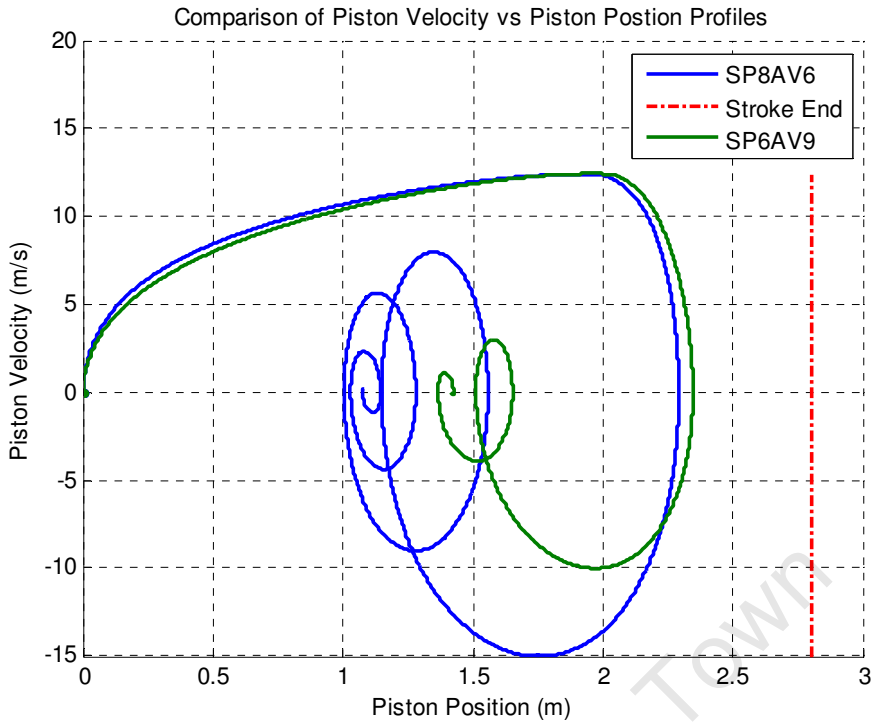

FIGURE 6-8: COMPARATIVE PLOT OF THE VELOCITY VS STROKE PROFILES FOR SIMULATION WITH SIMILAR FINAL SLED VELOCITIES

The green line shows the simulation which uses the higher number of acceleration valves (SP6AV9). By comparing the loops made by the plot after the cushioning air had been activated, the magnitude of the oscillations can be seen to be to be smaller for the lower pressure simulation (green).

If the chamber pressure histories between simulations with similar final sled velocities are compared, as in Figure 6-9, the extended duration of the oscillations in simulation with a higher supply pressure and fewer valves is also seen. The dotted lines, representing the lower pressure simulation, show the pressures stabilising at 725 ms, while the higher pressure simulation's pressures only start to stabilise at 1000 ms.

This was thought to be attributed to the smaller difference in the chamber pressures as the cushioning air pressure was rising. The *SP6AV9* simulation had: a larger flow area into the rear chamber and slightly lower piston acceleration. At the point that the cushioning air was activated the rear chamber pressure of *SP6AV9* was higher than that of *SP8AV6*. The *SP6AV9* front chamber pressure was also lower than that of *SP8AV6*; meaning that *SP6AV9* had a lower pressure when compared to *SP8AV6*.

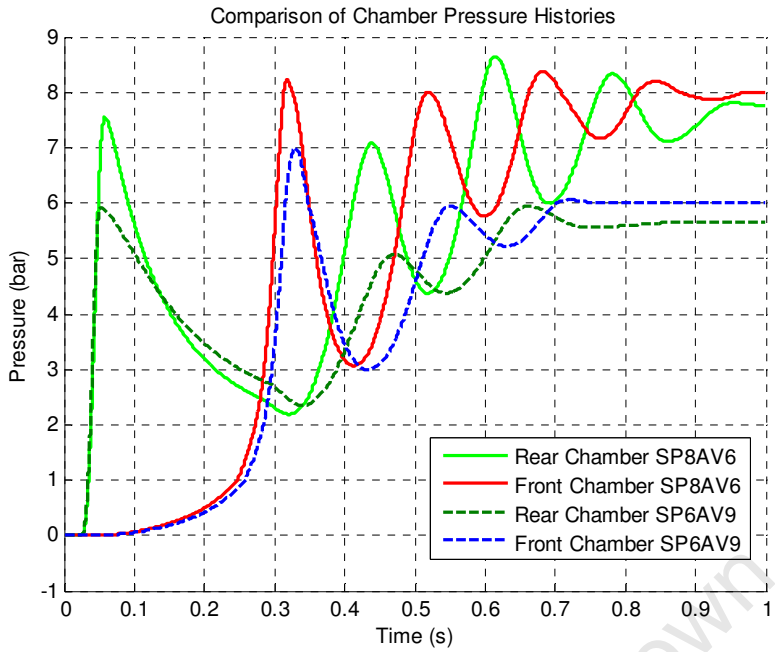

FIGURE 6-9: COMPARATIVE PLOTS OF THE CHAMBER PRESSURE HISTORIES FOR SIMULATIONS WITH SIMILAR FINAL SLED VELOCITIES

In order to compare the trends between oscillation decay time and the number of acceleration values used, a plot of the velocity histories for a range of simulations which used 12 valves was created, Figure 6-10. This plot shows that all the simulations stabilised between 650 and 780 ms, a 130 ms interval.

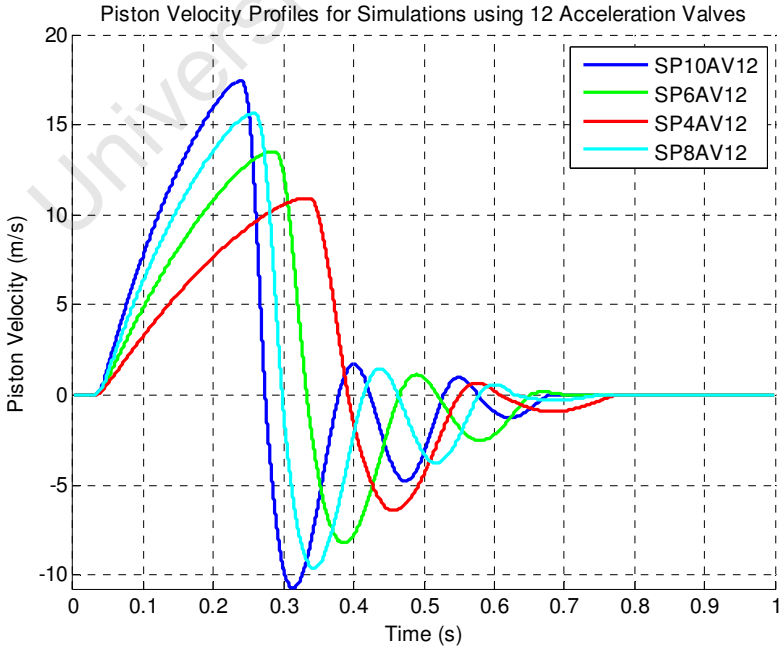

FIGURE 6-10: PLOT OF THE VELOCITY HISTORIES FOR SIMULATIONS USING 12 ACCELERATION VALVES

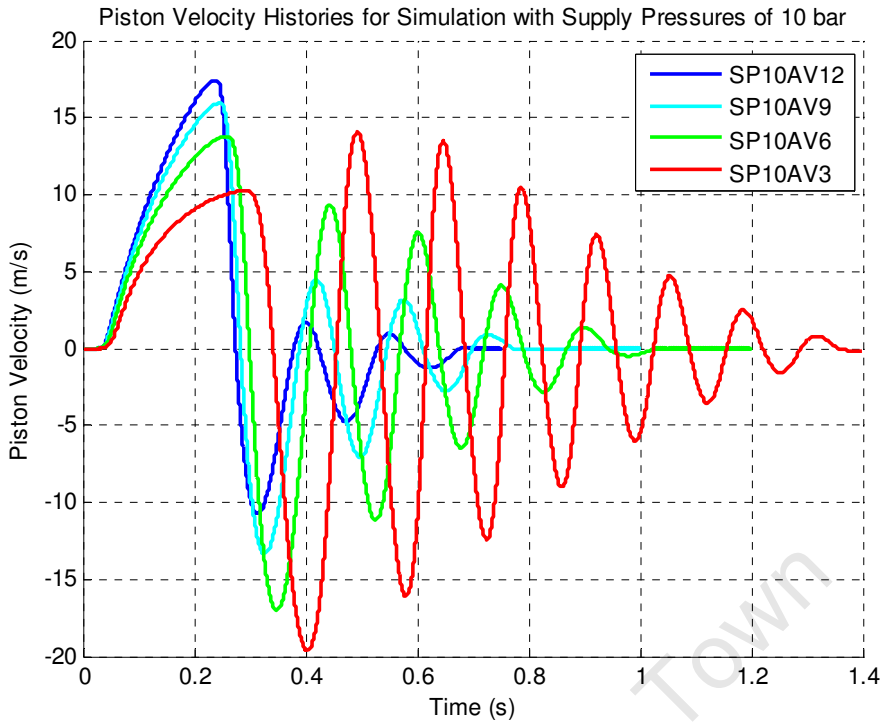

FIGURE 6-11: COMPARATIVE PLOT OF THE VELOCITY HISTORIES OF SIMULATIONS WITH A SUPPLY PRESSURE OF 10 BAR

Another comparison was made between the velocity histories of simulations where the pressure was kept constant, while the numbers of activated acceleration valves were varied. A plot was generated in which the velocity histories for simulations with a supply pressure of 10 bar were collected. This plot is shown in Figure 6-11.

An inversely proportional relation between the decay time and the number of acceleration valves activated is seen in Figure 6-11. To investigate this relationship, the decay times of the different simulations were plotted against the number of values for the 10 bar simulations. The decay time was defined as the time taken from the initial peak of the curve to when the piston came to rest.

The points provided by the curves in Figure 6-11 did not provide enough data to determine a trend, so simulations for all the valve combinations were run. A quadratic trend line was found to fit the data. The plot is shown in Figure 6-12. The trend line is described by the equation in Equation 6-1.

EQUATION 6-1:

$$t_{decay} = 9.6 \times 10^{-3} N_{valves}^2 - 0.2171 N_{valves} + 1.7105$$

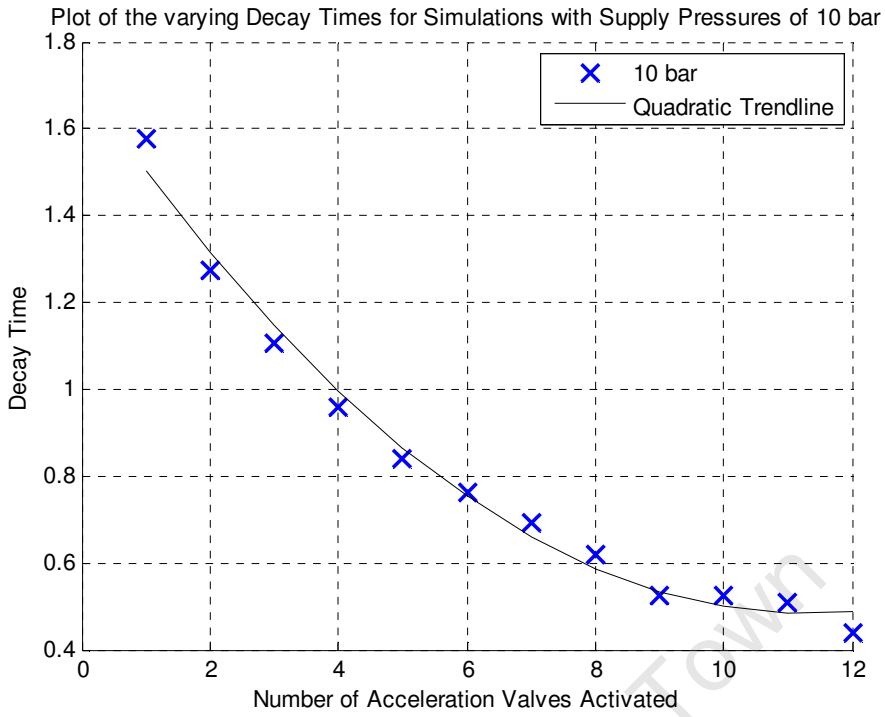

FIGURE 6-12: PLOT OF THE VARIATION OF DECAY TIME WITH AN INCREASE IN ACCELERATION VALVES

The cause of the increase in decay time and magnitude of the initial oscillation was attributed to the cushioning air entering the front chamber at the same rate for all the tests. Due to the manner in which the valves were connected in the physical system all 6 cushioning air valves had to be activated for each test. If any were not activated the cushioning air would escape to the atmosphere through the inactivated valves.

The less acceleration valves activated during a test, the lower the final sled velocity and the rear chamber pressure. For all the tests, the flow of cushioning air into the front chamber was constant. This created a similar piston velocity change for all the tests and as seen in Figure 6-9 a greater pressure difference between the chambers for the test with fewer activated acceleration valves.

To illustrate this, Figure 6-13 compares two 10 bar, 1 acceleration valve tests. During the one test, only one cushioning valve was activated. This investigation only supports the argument that **the flow rate of the cushioning is responsible for the oscillations**. It is not a solution as the number of cushioning valves cannot be changed in the physical system.

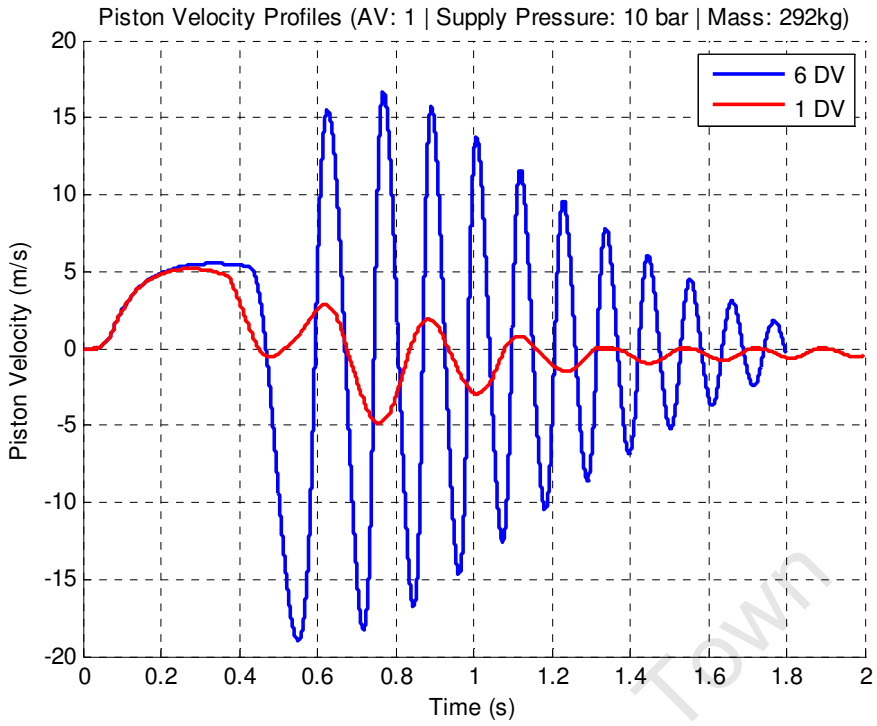

FIGURE 6-13: COMPARATIVE PLOT OF USING DIFFERENT NUMBERS OF CUSHIONING VALVES

The reduction in the magnitude of the oscillations through the reduction of the number of cushioning valves is highlighted in Figure 6-13. Initially the piston velocity remains the same for both simulations. The piston velocity of the simulation with a single cushioning value (1 DV) starts to slow prematurely. This is due to a reduction of flow out of the front chamber which causes its pressure to rise before that of the *6 DV* simulation. This phenomenon is visible in both the plots shown in Figure 6-14 and Figure 6-15.

In Figure 6-14 the effect of the gas in the front chamber only escaping through one valve is seen. The cushioning air is only activated once the piston position reaches 1.5 m. The piston velocity of the *1 DV* simulation starts to decrease from the 0.5 m mark. Once the piston reaches the 1.5 m mark, the cushioning air is activated and the piston is retracted after an initial increase in velocity. This increase can also be explained by the fact that the relatively low flow rate of the gas escaping from the front chamber causes a pressure rise in the front chamber, which reduces the piston velocity to zero *before* the cushioning air is activated. The stationary piston allows the pressure in the rear chamber to increase, moving the piston over the 1.5 m mark; activating the cushioning air.

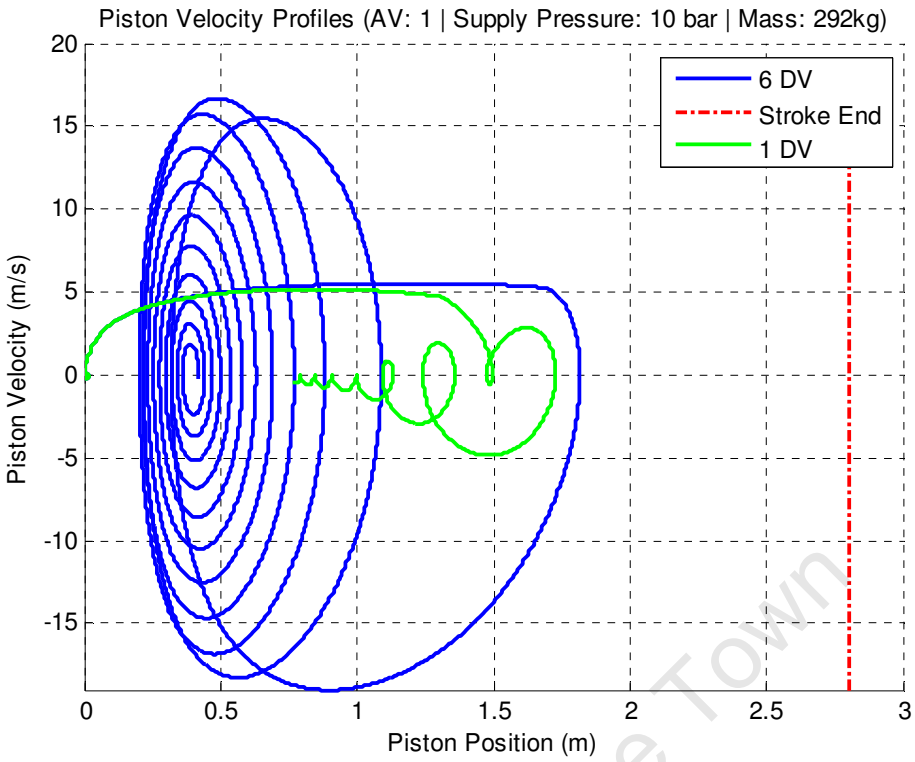

FIGURE 6-14: COMPARATIVE PLOT OF THE VELOCITY VS PISTON POSITION PROFILES FOR VARYING NUMBERS OF DECELERATION VALVES

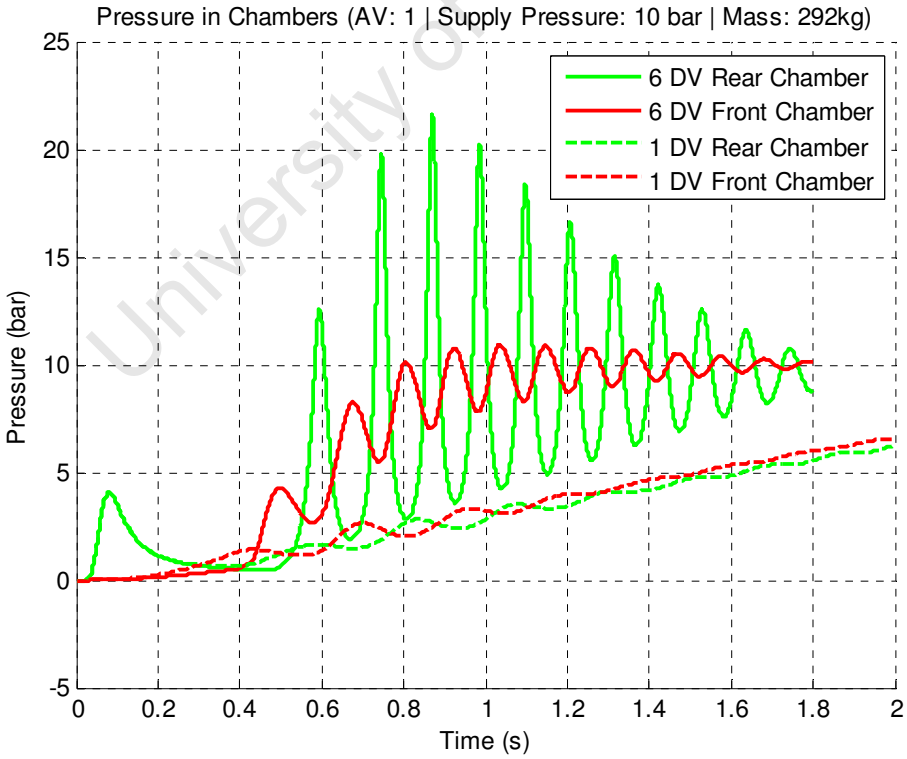

FIGURE 6-15: COMPARATIVE PLOT OF CHAMBER PRESSURE PROFILES FOR VARYING NUMBERS OF DECELERATION VALVES

The accuracy of these results was verified by comparing the final sled velocities, of simulations with the same input parameters, to those of the FESTO predictions. FESTO had provided plots of their piston velocity history predictions for four different simulations. The FESTO plots showed similar profiles to those outputted by the acceleration stage model. The peak velocities of these profiles were taken as the final sled velocities.

Although the FESTO predictions were not based on exactly the same conditions as the Acceleration Stage model, the results were compared with these differences in mind. There were differences in: the sled masses, cylinder strokes and the status of the acceleration valves after the activation of the cushioning air. These are shown in Table 6-3. As the FESTO predictions were made by software programmed for their standard components, the entry multiple valves into the chambers of the cylinder had to be accounted for through one port(15). In the Acceleration Stage model multiple valve ports were accommodated for by the code.

TABLE 6-3: DIFFERENCES IN THE SIMULATION CONDITIONS

		FESTO	Acc Stage
Stroke	m	2.5	2.8
Cushioning Air Trigger	m	1.5	1.5
Sled Mass	kg	250	292
Rear Chamber after CA Trigger	-	Not Sealed	Sealed

The longer stroke of the Acceleration Stage cylinder increased the volume of the front chamber, decreasing the initial increase in the front chamber pressure. The lower sled mass allowed higher accelerations to be achieved by the cylinder. Not sealing the rear chamber only affected the velocity profile after the cushioning air was activated, having little affect on the peak velocity.

TABLE 6-4: COMPARISON OF THE FESTO AND ACCELERATION STAGE MODEL VELOCITY PREDICTIONS

Input Parameters		Velocity (m/s)	
# Valves	Pressure (bar)	FESTO	Acc Stage
6	6	10.78	10.74
12	6	13.24	13.49
6	10	13.97	13.74
12	10	17.78	17.39

All the predictions shown in Table 6-4 show the velocity given by FESTO to be larger except for the 12 valve, 6 bar case. The FESTO predictions were expected to be larger as the sled mass was lower. The increased piston deceleration caused by the shorter stroke would be minimal compared to the affect of the lower mass.

This discrepancy was attributed to the differences in the modelling of the multiport end caps. The different methods used by the simulations to account for the multiple acceleration valves could have resulted in slightly different flow rates. In the 12 valve, 6 bar case this difference outweighed the affect of the lower sled mass. The method used by FESTO to incorporate the flow through one port was not known and so this could not be fully established.

This aside, **the comparison showed good correlation between the predictions**. The largest error was 2.2 % - in the 12 valve, 10 bar case.

6.2 DECELERATION STAGE SIMULATION

As mentioned in section 4.3, the original Deceleration Stage simulation written by MOOG was modified to incorporate the user defined input parameters and the final sled velocity from the Acceleration Stage simulation. The results mentioned in this section relate to those of the modified simulation.

The variables that were of primary interest were: the sled velocity profile and the force profile exerted on the sled by the deceleration piston. This is due to the fact that these where the two possibilities for use as loading profiles in the finite element model. Other variables of interest were: the cylinder's effective pressure; sled acceleration and the position histories of the sled and the end of the piston.

The adjustment of the control parameters was limited to the control parameter adjustment equations. No tuning or tweaking of the control parameters was performed. The method for using the control parameter adjustment equations and the set of tuned data supplied in the model documentation(6) were used to adjust the parameters. The consequence of this was that the accuracy of the resulting decelerations deteriorated for set point pressures further from the tuned value(6). The tuned parameters in the model documentation were tuned for a set point pressure of 100 bar.

As mentioned in section 5.7.2, a numerical anomaly was found in the force output of the deceleration stage. The anomaly was also present in the deceleration plots. In Figure 6-16 the spike in the deceleration prediction occurs at the same point in time as the drop in sled velocity. Time zero represents the moment that the sled makes contact with the end of the piston. In the auxiliary finite element simulations of the impact, the spike was proven to *not* be the actual force experienced by the sled. The spring mass model that was written to investigate the spike produced the same anomaly, when loading and constants similar to those of the deceleration stage were used. (For more detail about the spring mass model refer back to section 5.7.2.) This proved that the anomaly was a result of the spring mass approach used in the contact plate model, allowing it to be disregarded and replaced with forces from the auxiliary simulations.

For the maximum velocity case, the predicted contact velocity of the sled was 17.063 m/s. This was very close to the nominal value of 17 m/s. The system was tuned for the following conditions: a contact velocity of 17 m/s, sled mass of 300 kg and a set point pressure of 100 bar. The results in Figure 6-16 are for a test with: a contact velocity of 17.063 m/s, sled mass of 292 kg and a set point pressure of 100 bar. These values did not vary significantly from the parameters of the test for which the control parameters were tuned; meaning that the adjustment of the control parameters by their equations should have been enough to obtain good results.

The results from this simulation are shown in the following figures. The sled deceleration and velocity are plotted in Figure 6-16. At time zero the spike in the deceleration can be seen as well as the drop in velocity.

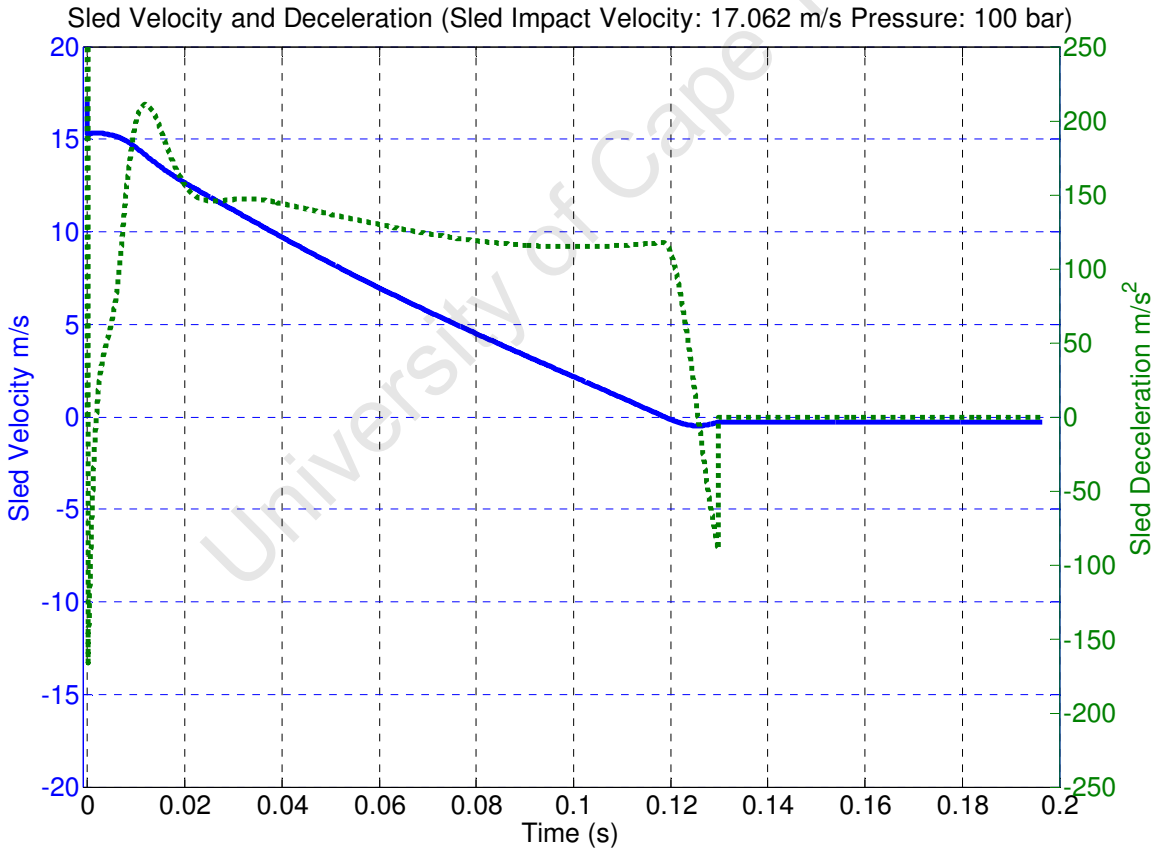

FIGURE 6-16: PLOT OF THE SLED VELOCITY AND DECELERATION PROFILES FOR A 100 BAR SET POINT

While the deceleration is relatively constant during the deceleration stage, it must be noticed that its magnitude is less than would be expected from an ideal application of the

100 bar set point pressure. The control system attempted to keep the effective pressure of the cylinder at the set point value. With an effective pressure of 100 bar, the 100 mm bore diameter should in theory decelerate the sled at 27g. The maximum deceleration of the sled ignoring the initial spike was 211 m/s^2; 58 m/s^2 lower than the theoretical value.

At time 0.1256 s the deceleration becomes negative. This was found to be caused by the damping constant of the rubber stopper and the method used to incorporate it in to the force calculation. The damping force was calculated by multiplying the difference between the piston and sled velocities by the damping constant; as in Equation 6-2.

EQUATION 6-2:

$$F_{damping} = C \times (v_{pis} - v_{sled})$$

This meant that as this difference became negative i.e. when the sled started moving away from the piston, the damping force would become negative. No measures had been taken into account in the damping model for the fact that: the interaction between the end of the piston and the sled could not exert a negative deceleration force on the sled and that the force created by the damping as the stopper relaxed, was exerted on the sled. The damping force was only forced to zero when the spring force was zero.

A filter was fitted to the spring model which only allowed it to exert a positive deceleration force on the sled. During the stage where the deceleration is negative, the spring force has not quite reached zero. This meant that the negative damping force was still being transferred the sled. As the magnitude of the damping force was larger than that of the spring force, the resulting force exerted on the sled was negative. This was not a reality as there was no physical connection to allow this type of force. As the spring force reached zero, the damping force was forced to zero as well; resulting in the discontinuous jump to zero acceleration at time 0.1298 s.

The fact that the negative forces exerted on the sled cannot be supported by the physical piston meant that the increase in sled velocity as the sled loses contact with the end of the piston, was another irregularity of the model. In an actual test, **the sled would travel back along the tracks at the velocity represented by the lowest point of the curve.**

As mentioned before, the acceleration predicted by the model, was lower than the theoretical force exerted by an effective pressure equal to the set point pressure. This together with the fact that the effective pressure was actually higher than the set point pressure highlighted the losses in the system. Figure 6-17 shows the effective pressure profile for the same simulation as discussed above.

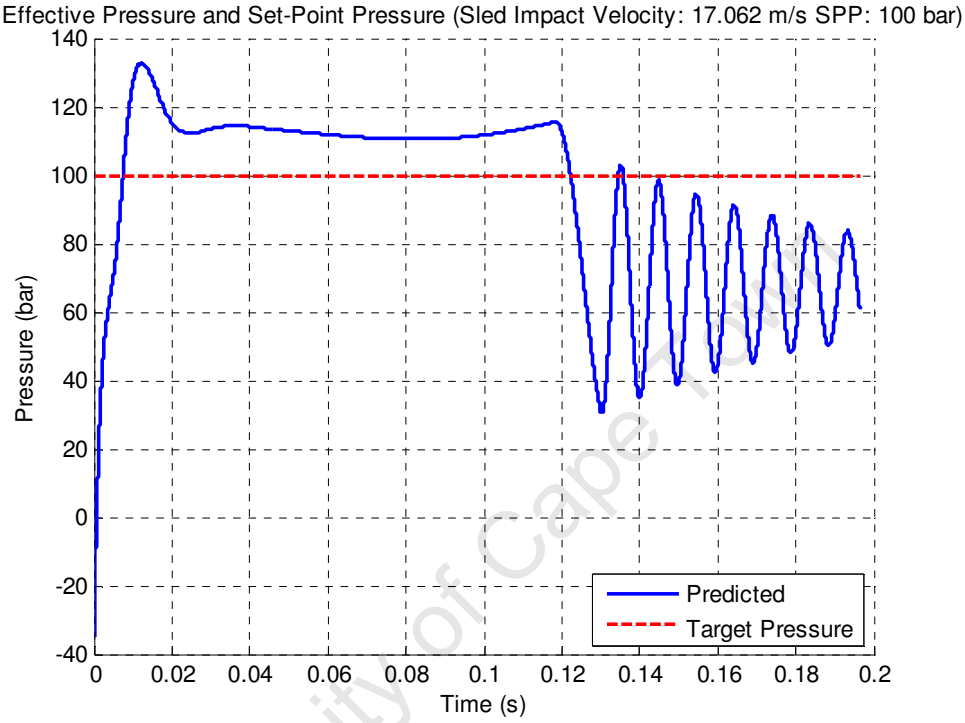

FIGURE 6-17: PLOT OF THE EFFECTIVE PRESSURE HISTORY FOR A 100 BAR SET POINT

The plot in Figure 6-17 covers the domain from time zero, the moment of impact, to the end of the duration of the simulation. Notice how, at time zero, the effective pressure is -35 bar, meaning that the resultant force was in the retract direction. After the sled had made contact with the end of the piston, the effective pressure increased to above the set point of 100 bar. The initial negative pressure was a result of the pre-acceleration of the piston. The plateau region represents the deceleration of the sled. Once the sled had been decelerated, the effective pressure started to oscillate in an effort to hold the piston at the retract position.

So as to compare the profiles of the tuned simulation to those of a higher deceleration, plots of both simulations' velocity and displacement profiles were made. A set point pressure of 200 bar was chosen for the higher deceleration. The maximum predicted

deceleration from the 200 bar simulation was 583 m/s^2, which is equivalent to 59.4g. As 59g was the maximum deceleration specified for the design of the system, 200 bar was taken to be the maximum set point pressure. Figure 6-18 shows the velocity profiles of the two simulations.

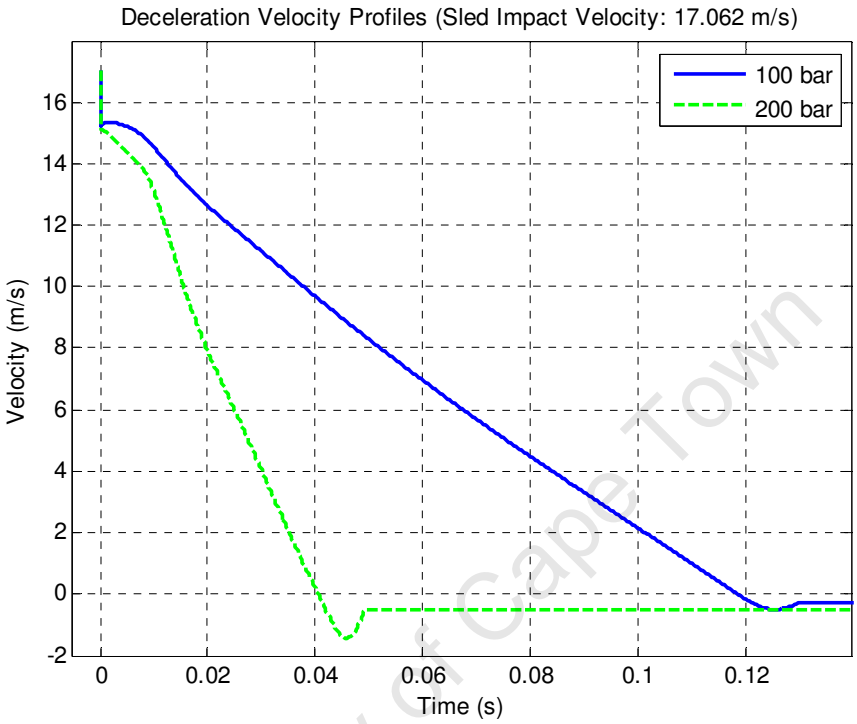

FIGURE 6-18: COMPARATIVE PLOT OF THE DECELERATION VELOCITY PROFILES WITH SET POINTS OF 100 AND 200 BAR

Notice how the initial drop in velocity is very similar for both the 100 and 200 bar simulations; being 2.37 m/s and 2.52 m/s respectively. The emphasised dip at the end of the 200 bar simulation was a result of the larger difference between the sled and piston velocities. Again the actual rebound velocity of the sled was the lowest point of the profile.

The increased rebound velocity of the sled in the 200 bar prediction is seen in Figure 6-19. Figure 6-19 is a plot of both the piston and sled positions from the operating point onwards. In both the 100 and 200 bar cases, before the sled and piston come apart, the red piston position curves are covered by the blue curves.

The difference in the rebound velocities can be seen by comparing the gradients of the sled positions for the two set point pressures. At the point immediately to the right of their turning points, the gradient of the *Sled 200 bar* curve was steeper than that of the *Sled 100*

bar curve. The higher rebound velocity created a larger damping force, increasing the size of the dip in the velocity profile.

For the maximum velocity case the set point pressure should not be lower than 100 bar. Figure 6-19 shows the sled leaving the piston very near the retract position of the piston. If the set point pressure was lowered, the sled would stop suddenly as the piston reached its end stop. This could cause damage to the cylinder and the sled. The displacement plot from a 50 bar simulation is shown in Figure 6-20. After the piston reaches its end stop, the sled is rebounded at a high velocity. Apart from the possible damage caused to the piston and sled during the rebound, the sled would start travelling back towards the pneumatic cylinder at the rebound velocity.

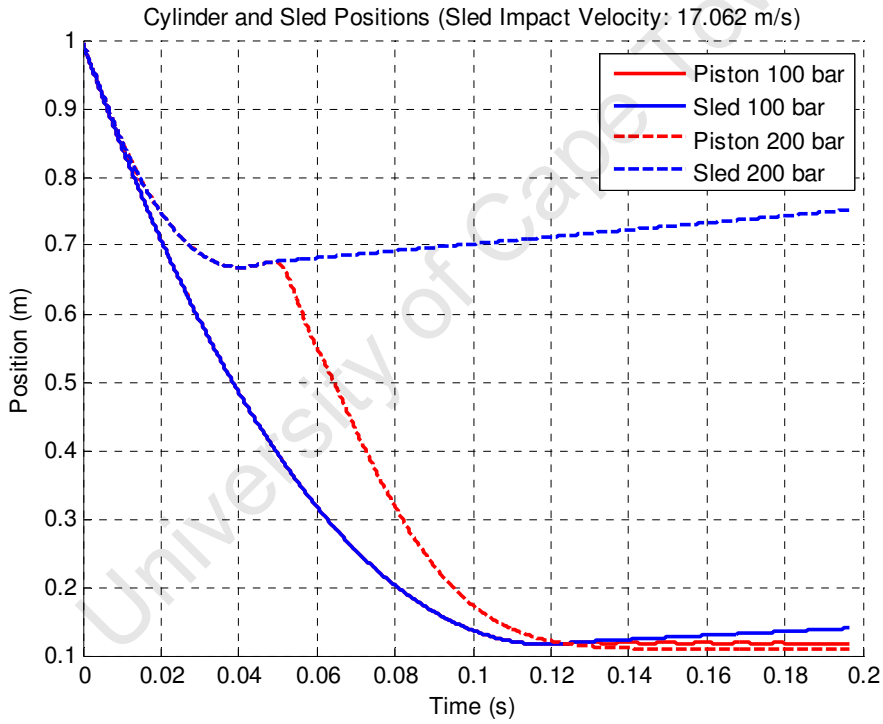

FIGURE 6-19: COMPARATIVE PLOT OF THE SLED AND PISTON POSITIONS FOR THE 100 AND 200 BAR SIMULATIONS

The *Piston 200 bar* curve illustrates how the piston retracts to it retract position after the sled has been decelerated. The same is not clear in the *Piston 100 bar* curve as the deceleration was only completed once the retract position had been reached.

In the case of the 50 bar curve in Figure 6-20, the cylinder bottoms out after which the control system struggles to find the retract position; retracting the piston to the end stop again. Finally the piston is extended back to the retract position.

This simulation illustrates the importance of having a deceleration which can slow the sled down in time. In the case shown in Figure 6-20, the hydraulic cylinder would have been damaged after which the sled would travel back down the rails at a velocity similar to that at which it approached.

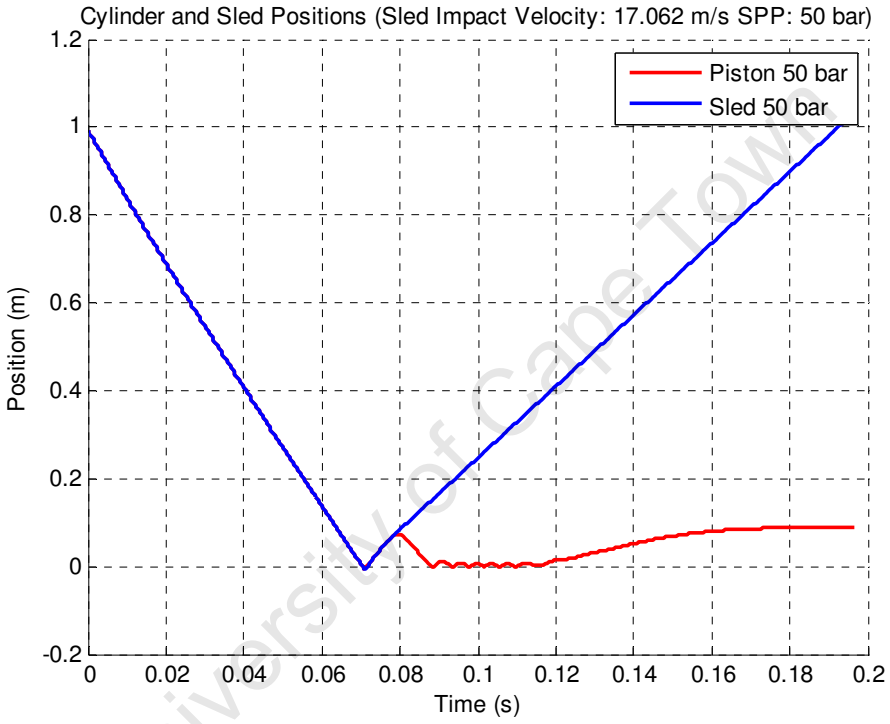

FIGURE 6-20: COMPARATIVE PLOT OF PISTON AND SLED POSITIONS SHOWING THE EFFECT OF AN END STOP COLLISION

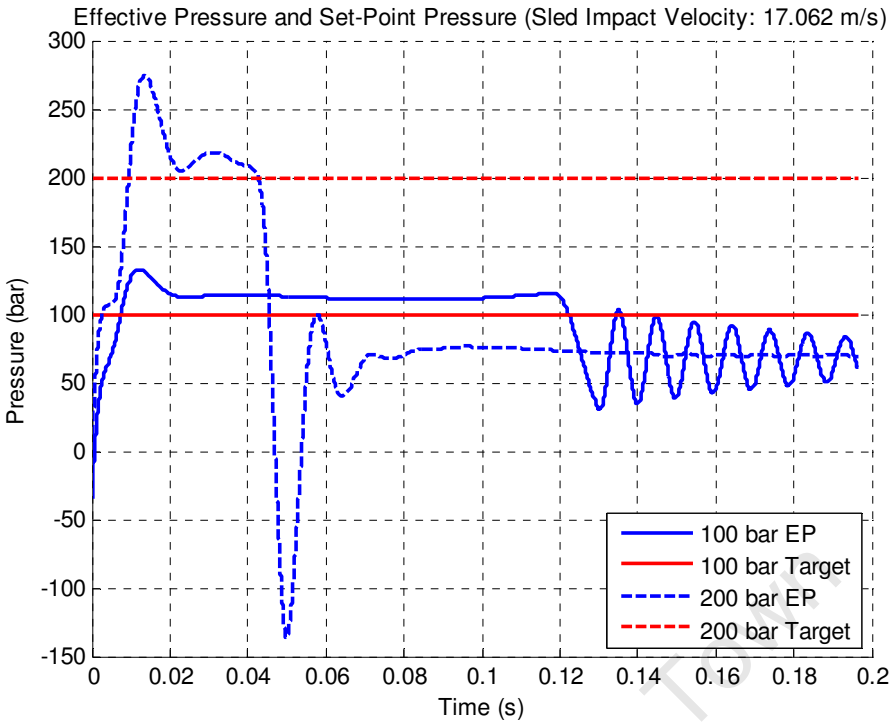

FIGURE 6-21: COMPARATIVE PLOT OF THE EFFECTIVE PRESSURE PROFILES FOR THE 100 AND 200 BAR SIMULATIONS

Figure 6-21 shows the difference in the effective pressure profiles of the 100 and 200 bar simulations. The plateaus of the blue curves represent the regions where the deceleration of the sled takes place. The negative pressure after the plateau of the *200 bar EP* curve was to retract the piston to the retract position. No negative pressure was needed in the 100 bar simulation because the piston was already in the retract position at the end of the deceleration.

The extended oscillations at the end of the 100 bar curve were due to the fact that the control system was continually over correcting in an attempt to achieve the retract position. This over correcting was not as prevalent in the 200 bar simulation as the sled was rebounded well away from the retract position, so the control system could better control the retraction of the piston.

6.3 FINITE ELEMENT ANALYSIS

The finite element analysis of the system was carried out in two ways: a modal analysis was performed separately on the rail system and the sled and a dynamic analysis of the sled sliding along the rails was also carried out.

The loading used for the dynamic analysis was, as mentioned before, derived from the result of both the acceleration and deceleration stage simulations. The adjustments made to the deceleration stage loading were detailed in section 5.7.2.

6.3.1 MODAL ANALYSIS

The results of the modal analysis were used to identify the weakest loading orientations of the structures and the frequencies associated with the modes. The frequencies were used to compare to any oscillating phenomena found in the dynamic analysis's results.

As the sled and the rail system were analysed separately for this section, boundary conditions had to be assigned to the sled to imitate the rail interactions. The sled was constrained in the X and Y directions at the slide mounts while allowed to move freely in the Z direction. 10 eigenvalues were requested from the sled simulation. For the rail system simulation the boundary conditions remained as detailed in section 5.6. 10 eigenvalues were also requested from this simulation.

Images of the deformed structures for all the modes of the sled structures are shown below as well as the eigenvalues, eigenfrequencies and maximum displacement. The deformation scale factor was set to 1 for all the modes. The legend in the bottom right applies to all the sled modes. The nodal displacements in Mode 1 were all of equal magnitude along the Z direction as there was no constraint in this direction. This mode represents the sled sliding along the rails. For this reason no base view was show as it is similar to Mode 1.

The boundary conditions are shown in the images by the orange symbols. The point mass which represented the dummy and restraint system is shown; it is coupled to the sled as shown by the grey lines.

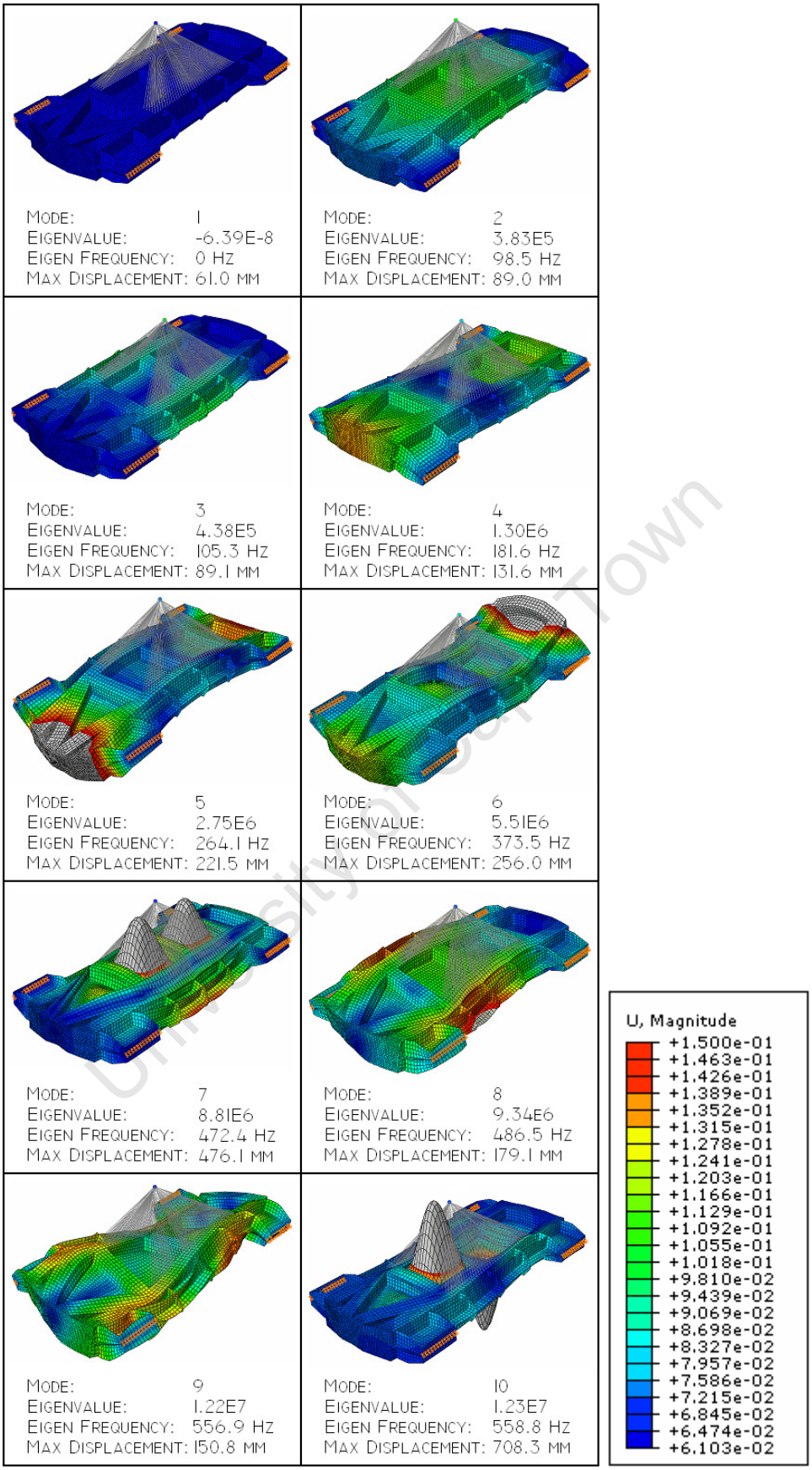

FIGURE 6-22: PLOTS OF THE SLED EIGENMODES

The modal analysis of the rail system highlighted the rail supports as the major weak point of the rail system. Deformations were created in the rail supports in all of the first 10 eigenmodes. No significant deformations were seen in the cross members.

The base state and the colour contour legend used for all the plots are shown in Figure 6-23. The contour plots are of displacement. The boundary conditions are represented by the orange and blue symbols. The blue symbols represent fixed rotation degrees of freedom while the orange represent constraint displacements.

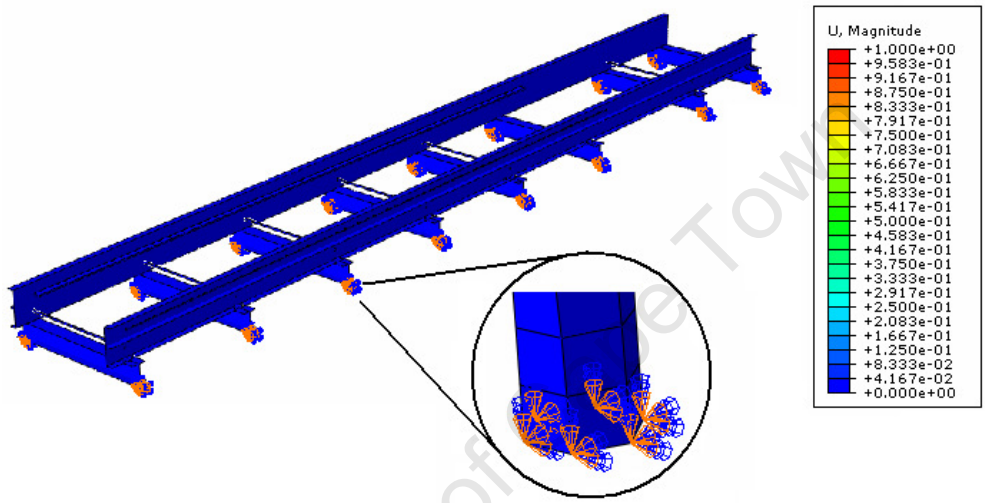

FIGURE 6-23: BASE STATE FOR THE MODAL ANALYSIS OF THE RAIL SYSTEM AND THE CONTOUR LEGEND

As the loads applied to the rail system were all from the interaction between the slides and the rails, the frequency of the loading was unknown. The model analysis helped indentify regions which would benefit from being stiffened.

It was clear from the results that the **rail supports lacked stiffness in the X direction** (parallel to the cross members). As no direct loading was applied in this direction this lack of stiffness might have been satisfactory; the result of the dynamic results answered this question.

The images and details of the different eigenmodes for the rail system modal analysis follow.

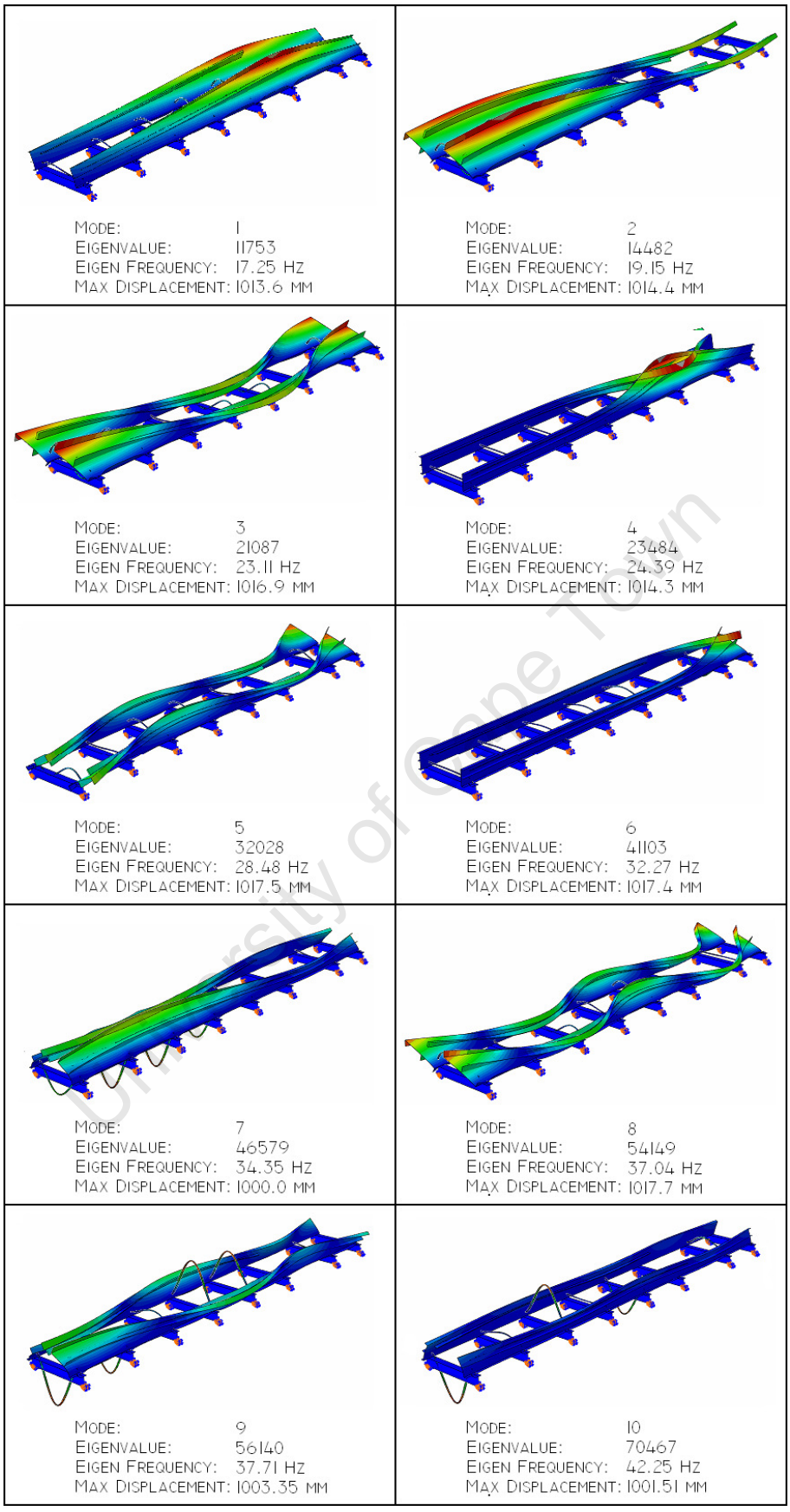

FIGURE 6-24: PLOTS OF THE RAIL SYSTEM EIGENMODES

6.3.2 DYNAMIC ANALYSIS

To analyse the structure under loading which represented the actual test, results from the acceleration and deceleration stage simulations were used. Three scenarios were used for the dynamic simulations. All of them used the acceleration force profile from maximum final velocity simulation. The deceleration force profiles of the three scenarios were all based on the maximum deceleration specification of 59g. Details on how the loading profiles were obtained and modified are in section 5.7.

6.3.2.1 STRESS ANALYSIS

Mild steel and high strength aluminium were to be used to construct the components of the system. For this reason it was decided that the stresses should ideally be kept under 100 MPa. This would give the system a design factor of over 2.

The acceleration and coasting stages of all three scenarios were exactly the same. As the acceleration force was relatively low compared to the deceleration force, the stresses in the system during these stages were low. The stresses in the system never increased over 100 MPa during these stages.

The maximum stresses and other results gained from the simulations are detailed for each of the three loading profiles in the sections that follow.

The highest stress in the entire system was in the slides. As the design of the slides or the method that would be used to attach them to the sled was not known, a rudimentary model was used. The stresses in the slides could easily be reduced by altering their cross sections. Figure 6-25 is an image of the slide at the point of the simulation where it was at its maximum stress state. As the loading scenarios differed in length and profile, the maximum stress states did not necessarily occur at the same points in time. Table 6-5 details the magnitude and point in time of the maximum stress states for the three scenarios. The stresses in the ERTACTEL C polymer never increased above their yield strength.

TABLE 6-5: MAXIMUM STRESSES IN THE SLIDES INSTANCES

Scenario	Time (ms)	Stress (MPa)
No Impact	15.59	214
Combo	15.59	323
59g Step	15.59	335

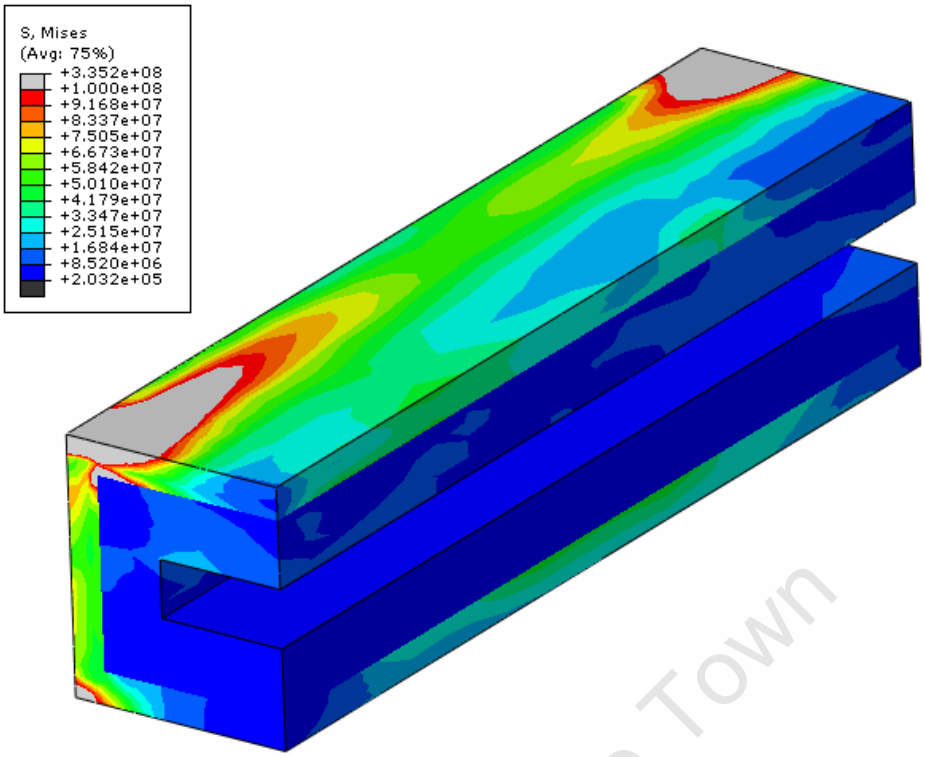

FIGURE 6-25: CONTOUR PLOT OF A SLIDE AT IS MAXIMUM STRESS STATE

Stresses in the sled remained below 100 MPa for the entire deceleration of the No Impact scenario. The stresses increased above this level in both the other scenarios. The points of maximum stress were where the gussets supporting the mounting plates joint the main part of the sled. Stress concentrations can also be seen at the corners of the impact area. These were accentuated by the kinetic coupling used to couple the reference point, through which the force was applied, to the impact area. The maximum stresses and contour plot for the sled are given in Table 6-6 and Figure 6-26.

TABLE 6-6: MAXIMUM STRESSES IN THE SLED

Scenario	Time (ms)	Stress (MPa)
No Impact	15.59	96.2
Combo	15.59	154
59g Step	6.00	172

Notice the more realistic stress distribution created by the distributed coupling used to couple the point mass representing the dummy, compared to the kinetic couplings used on the impact areas. The distributed coupling, distributes more of the load created by the inertial forces of the dummy mass to the edges of the mounting area.

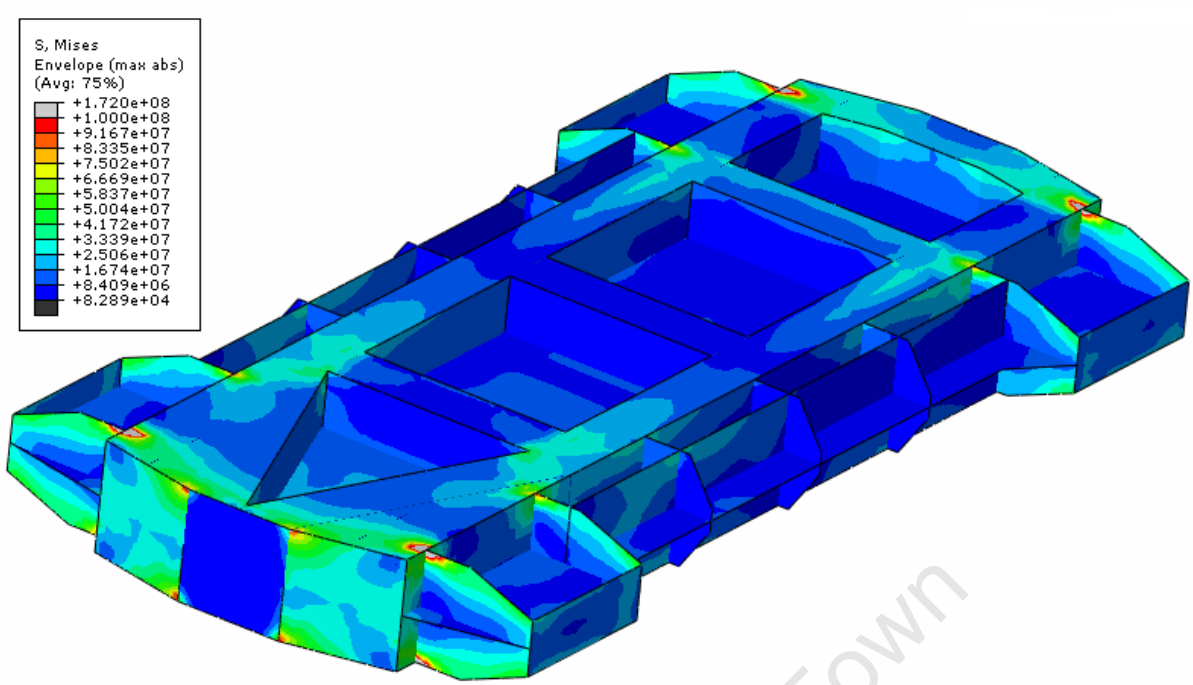

FIGURE 6-26: CONTOUR PLOT OF SLED AT ITS MAXIMUM STRESS STATE

A contour plot from the auxiliary simulations showed how the stresses were distributed across the impact area when it impacted the model of the piston, see Figure 6-27. Notice the different stress contours around the border of the impact area compared to the image in Figure 6-26.

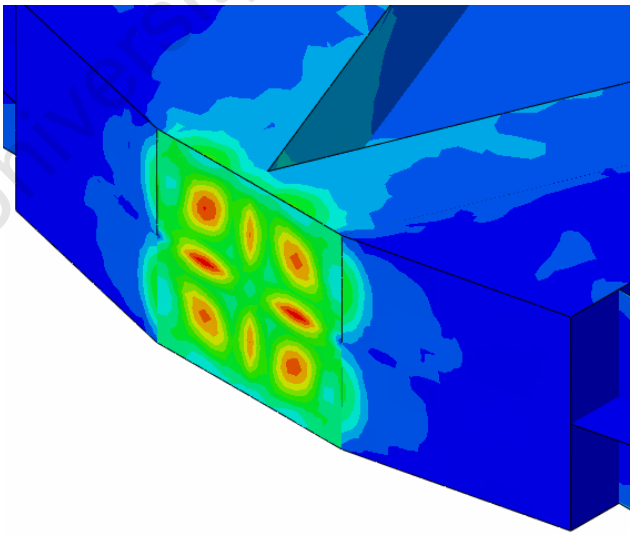

FIGURE 6-27: FORCE DISTRIBUTION ACROSS THE SLED IMPACT AREA FROM THE AUXILIARY SIMULATIONS

The results from the analysis of the sled suggest that **the conceptual design of the sled will survive the deceleration stage.** Modifications need to be made to the gussets of the slide

mounting plates to remove the stress concentrations at their corners. If a more substantial piece of material was used for the impact area the stresses would be more uniform, reducing the concentrations where the plate was connected to the rest of the structure.

Stress in the rails, rail supports and cross members were also investigated. These investigations were of real importance as construction had already begun. Any problems would have to be rectified by adding addition support to the existing design as it could not be changed.

The regions in which high stresses were found were near the deceleration end. These regions were at the ends of the first three cross members closest to the deceleration cylinder and at the points where the brace closest to the end joined the rail supports.

The cross member which experienced the highest stress was the one closest to the end. Stresses in the following two also rose above 100 MPa. The maximum stresses in the cross members for each scenario are given in Table 6-7. As the stress states at the end of the cross members were all similar a contour plot of the maximum stress state shown in Figure 6-28.

TABLE 6-7: MAXIMUM STRESSES IN THE CROSS MEMBERS

Scenario	Time (ms)	Stress (MPa)
No Impact	16.56	133
Combo	17.54	211
59g Step	6.60	203

From Figure 6-28, the maximum stresses are shown to be where the grounding bolts connect to flanges of the cross member and the region on the flanges between the grounding bolts. Both these regions of the model had been simplified during their creation.

The physical grounding bolts were fixed to the cross member flanges by two nuts; one on either side of the flanges. The bolts were extruded from the flange faces, meaning that the nodes at the top of the bolts were shared between the bolts and the flanges. This was effectively the same as a tie constraint, linking the displacements and rotations of nodes involved. Under the assumption that the nuts fastening the components together were tightly fastened this simplification was reasonable. As the nuts would have to be tightened to ensure the alignment of the rails was not affected by loads induced by the sled, it was therefore reasonable to assume that the nodes were linked.

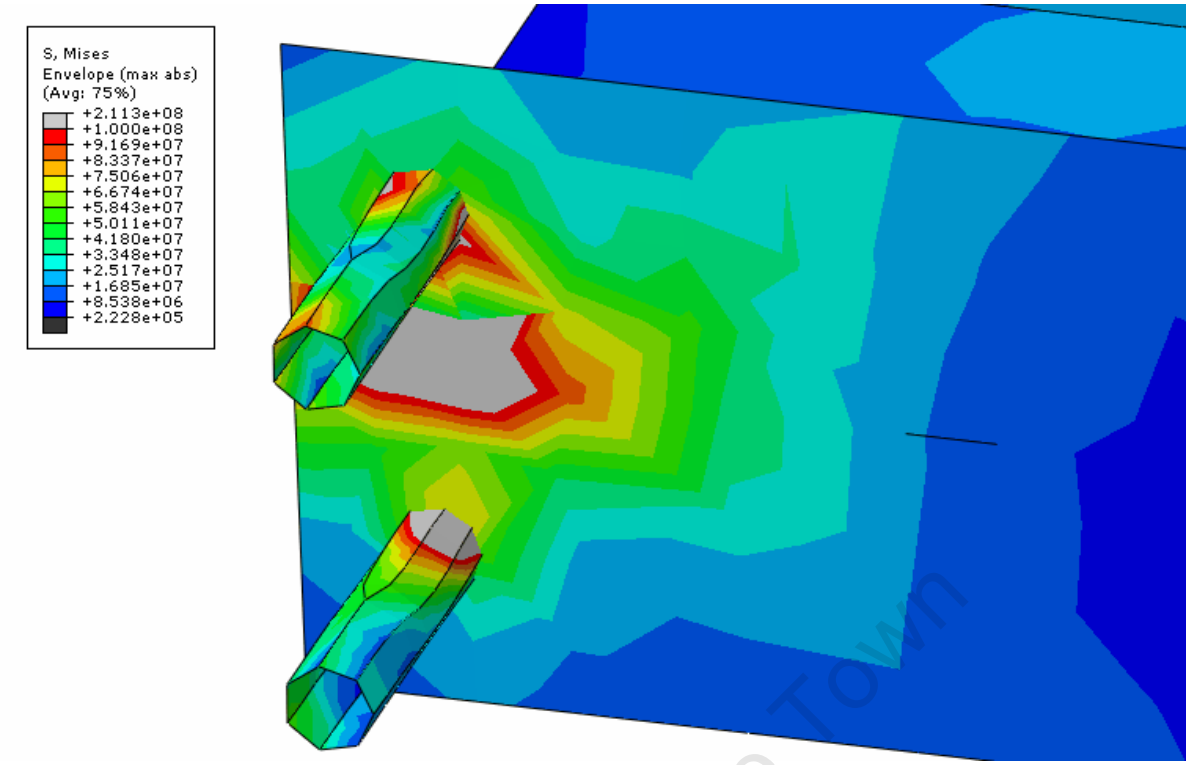

FIGURE 6-28: CONTOUR PLOT OF THE MAXIMUM STRESSES OF THE CROSS MEMBERS

The physical cross member had been constructed from two lengths of channel section bolted together, back to back. In the model the cross members were assumed to be I-beam profiles. Modelling the bolted connections between the channel sections would have required contact interactions to be specified between the touching faces of the channel sections. The computational expense of the calculating this interaction was increased by the fact that there were 7 instances of the cross member part in the assembly. Due to the computational expense the simplified model was used. To assess the manner in which the flanges were being loading Figure 6-29 was plotted.

Figure 6-29 shows the tops of the grounding bolt bending inwards. This suggests that the flange is loaded in tension. In the physical cross member the channel sections are not fastened at the ends. Loading of this nature would separate the channel sections from each other. This accommodating movement would remove stresses from their current position, but increase displacements and create higher stresses at the bolts which fasten the channel sections together. **Modifications to the rails system would be necessary** to reduce these stresses below 100 MPa.

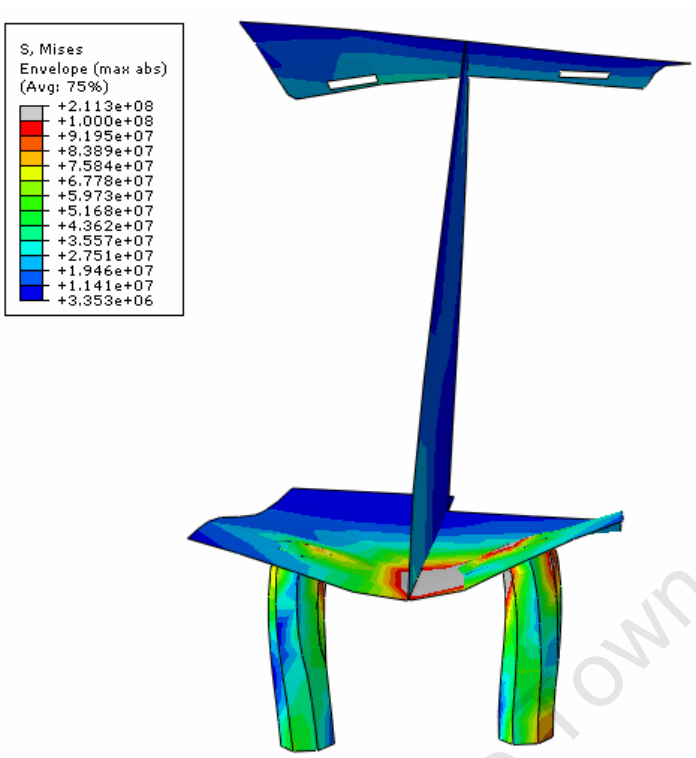

FIGURE 6-29: AN EXAGERATED DEFORMATION OF THE FORST CROSS MEMBER

The other regions of high stress were in the rail supports. Stress concentrations were found at the points where the braces connected to the rail supports. Before the braces were modelled the rail supports tended to deflect outwards. This meant that the braces were loaded in tension, pulling at the regions of the rail supports to which they were connected. Again this connection was simplified to a tie constraint causing localised loading at these points. The highest stresses were found in the brace closest to the deceleration cylinder. The maximum stresses from each loading scenario are given in Table 6-8. An example of the stress distribution is shown in Figure 6-30.

TABLE 6-8: MAXIMUM STRESSES IN THE RAIL SUPPORTS

Scenario	Time (ms)	Stress (MPa)
No Impact	42.87	132
Combo	44.82	197
59g Step	29.40	235

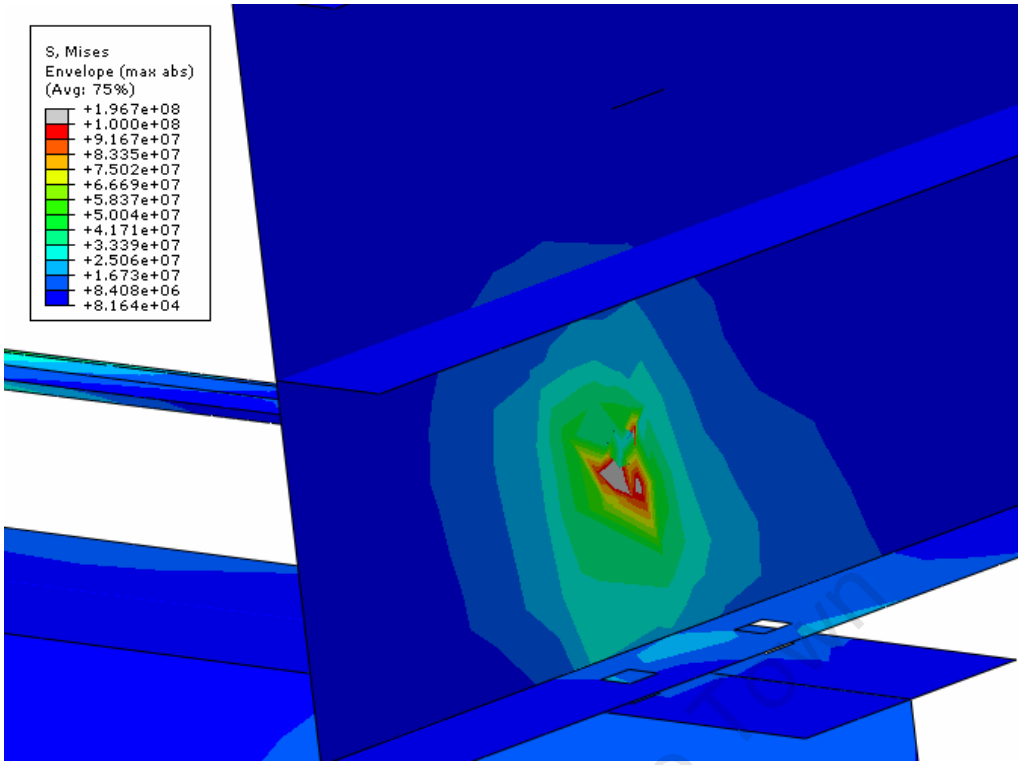

FIGURE 6-30: CONTOUR PLOT OF THE STRESSES IN THE RAIL SUPPORTS AT A BRACE CONNECTION POINT

Although not above the 100 MPa threshold Figure 6-31 shows a plot of the stresses in the rails during the 59g deceleration. The stress created by the interactions between the slides and the rail supports can be seen. Each slide caused a stressed region. The positions of the regions are important because they affect which of the cross members experience the brunt of the loading.

Notice how in Figure 6-31, the stresses at the first and third set of bolt holes are higher than at the second. It was for this reason that it was important to initiate the deceleration stage when the sled was in the correct position. As the operating stroke of the deceleration cylinder was 1 m, the length of the coasting step was tuned until the distance between the end of the rails and the front slides was just greater than 1 m. The distance used in the final simulation was 1001.1 mm.

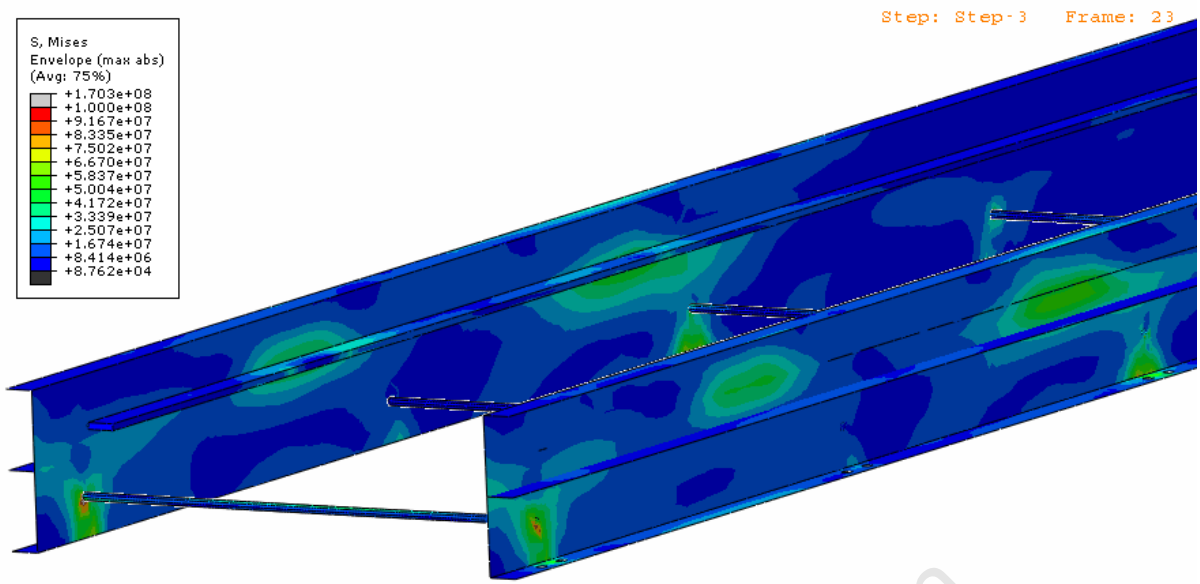

FIGURE 6-31: CONTOUR PLOT OF THE STRESSES IN THE RAIL SUPPORTS OVER THE ENTIRE DECELERATION REGION

6.3.2.2 DISPLACEMENT ANALYSIS

By creating a contour plot of the node displacements, the dynamics of the rail supports could be analysed. From the modal analysis of the rail system, the rail supports were found to be the most deformable part of the structure. As all the significant displacements occurred parallel to the cross members the displacements in the X direction were plotted.

Deformations which represented Modes 8 and 9 were found when the deformation scale factor was increased to 100. These are shown in Figure 6-32, Figure 6-33 and Figure 6-34. The contours show the ends of the rails deflecting up to 1.9 mm towards each other. In the simulation a 1 mm clearance was left between each slide and the inside face of the rail. This was large enough to accommodate the rail deflections.

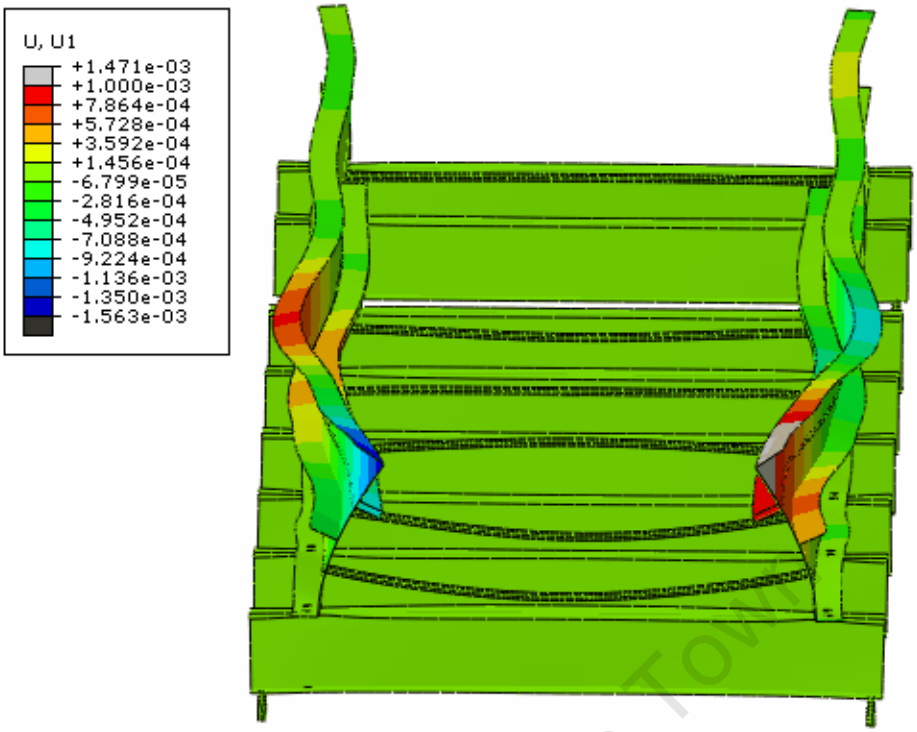

FIGURE 6-32: DISPLACEMENT CONTOUR PLOT OF THE RAIL SYSTEM EXHIBITING MODE 9 BEHAVIOUR

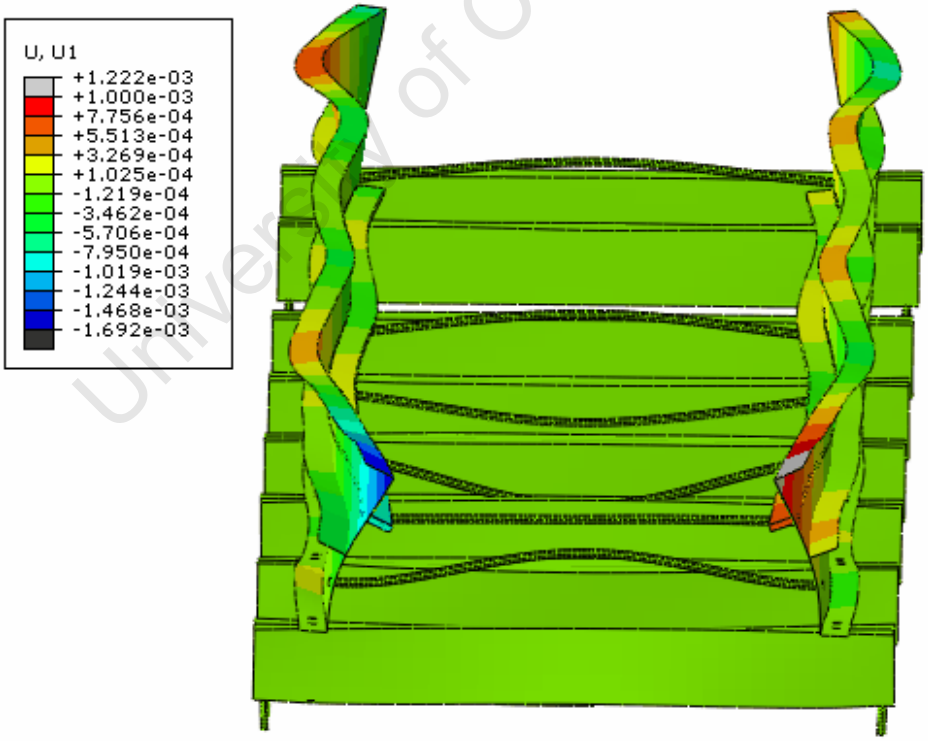

FIGURE 6-33: DISPLACEMENT CONTOUR PLOT OF THE RAIL SYSTEM EXHIBITING MODE 8 BEHAVIOUR

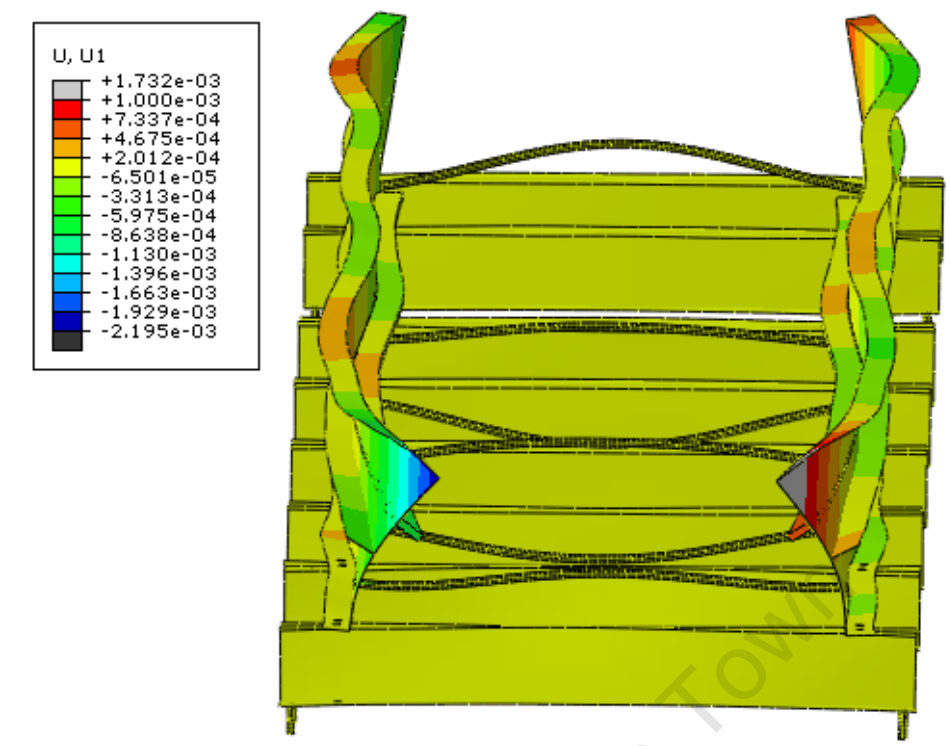

FIGURE 6-34: DISPLACEMENT CONTOUR PLOT OF THE RAIL SYSTEM EXHIBITING MODE 8 AND 9 BEHAVIOUR

6.3.2.3 COMPARATIVE PLOTS

From the history outputs of the simulations plots of: the kinetic and internal energy and the velocity and acceleration of the dummy mass were plotted. The plots of all three loading scenarios were plotted together for each variable to allow the differences to be compared.

In Figure 6-35 the kinetic energies of the different scenarios are compared. The acceleration and coasting stages of the simulations are identical. This was expected because the same loading was used during the acceleration stage for all the scenarios.

Very little difference can be seen in the *Combo* and *No Impact* curves. There was a slight deviation in the *Combo* curve from that of the *No Impact* at the beginning of the deceleration stage. This was due to the impact spike superimposed over the Deceleration Stage simulation's force prediction.

In the 59g scenario drops with a steeper gradient to the others. This is due to the force constantly decelerating the sled at 59 g, opposed to in the other scenarios where the deceleration only peaks at 59g for a moment.

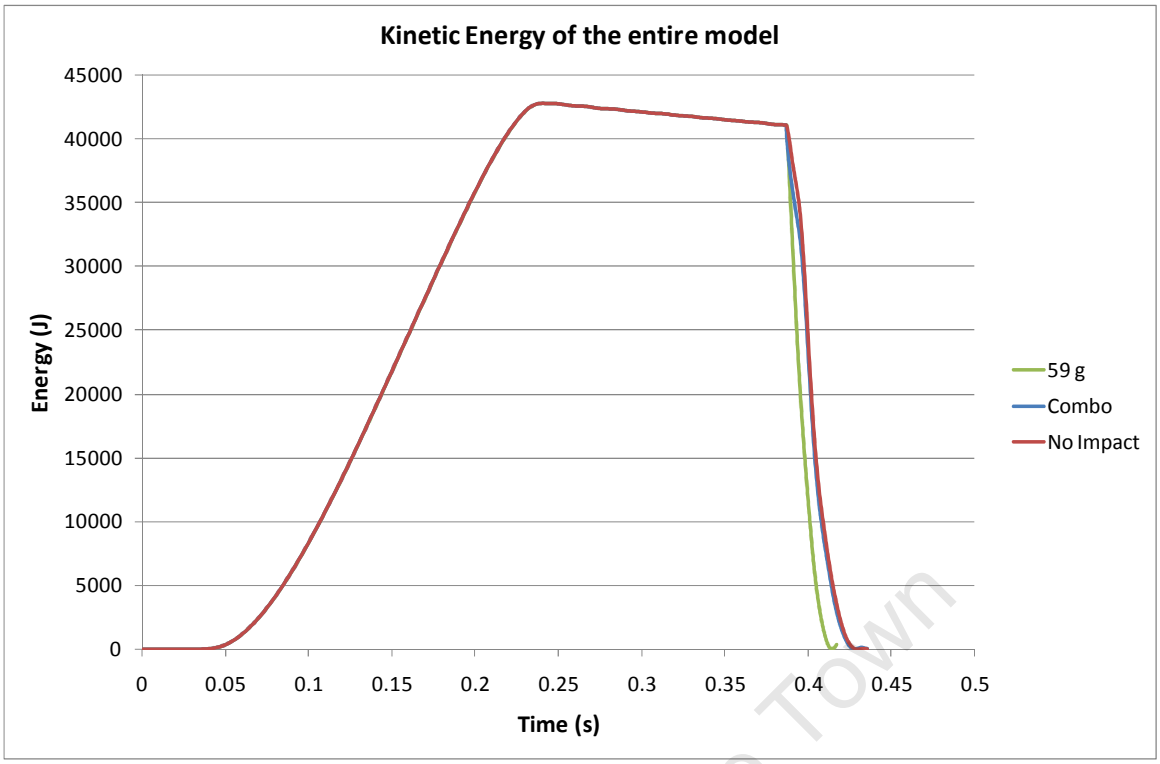

FIGURE 6-35: COMPARATIVE PLOT OF THE KINETIC ENERGIES OF THE DIFFERENT LOADING SCENARIOS

The fact that the kinetic energy plot has a similar profile to the dummy velocity suggests that all mass that has significant velocity in part of the sled and dummy systems. This was what was expected as the other components were all fixed to ground. Any large vibrations of the rail system should have had an effect on the kinetic energy.

Although the kinetic energy profiles were very similar, the different loading profiles did affect the total strain energy. The strain energy showed the same trends between the loading scenarios as the stress analysis. Total strain energy, referred to as Internal energy by ABAQUS, represents the amount of energy stored in an object due to undergoing deformations. Plots of the total strain energy gave an indication of the relative stress levels of the different scenarios. A plot of the models internal energy for the different scenarios is given in Figure 6-36.

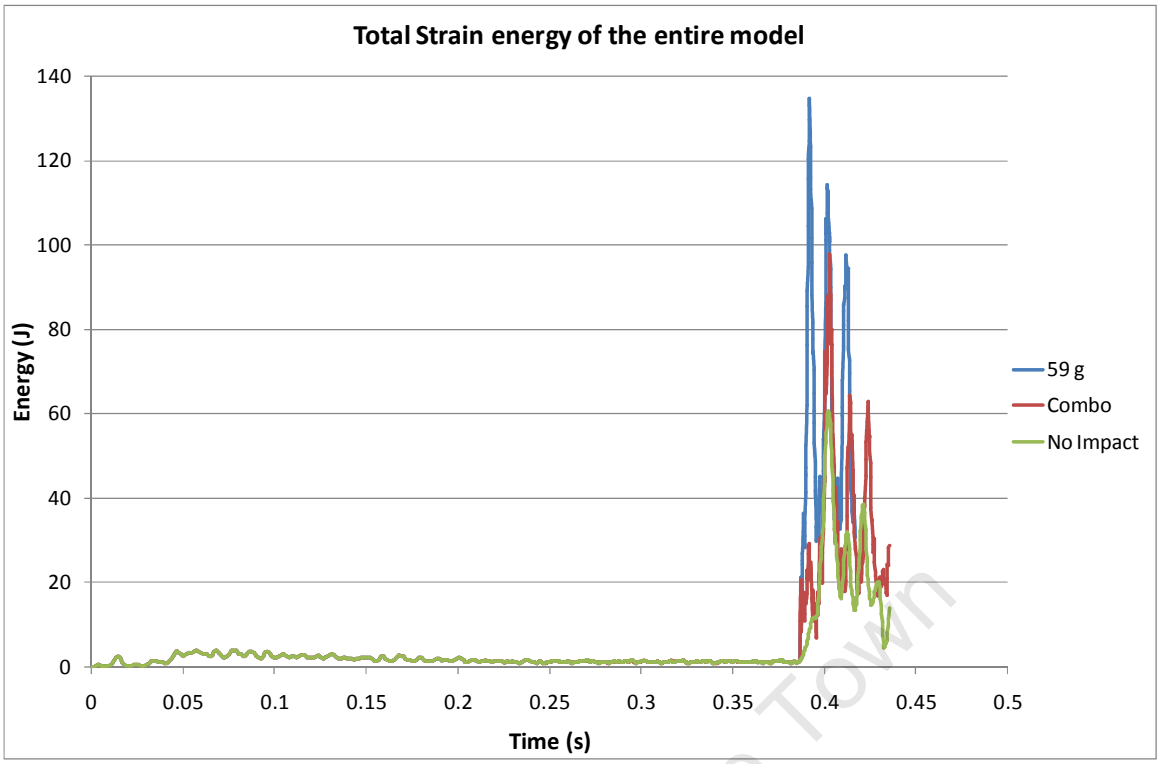

FIGURE 6-36: COMPARATIVE PLOT OF THE TOTAL STRAIN ENERGIES FOR THE DIFFERENT LOADING SCENARIOS

As in the before the energies during the acceleration and coasting steps were identical. The curves differ during the deceleration stage as seen in the stress analysis. The *59g* curve peaked at 134.5 J while the *Combo* curve peaked at 97.5 J and the *No Impact* curve at 60.0 J. This displayed the same trends as were found when comparing the stress in the different components of the model.

In Figure 6-37 the acceleration experienced by the dummy mass during the deceleration stage for each of the three scenarios are plotted. A target line at 59g was also plotted to compare to the other curves. **All the scenarios reached the 59g target**. If the *Combo* and *No Impact* curves were compared it was found that fundamental difference between the two was that the *Combo* curve contained larger oscillations than the *No Impact* curve. These large oscillations were also present in the *59g* curve.

The *Combo* and *59g* load profiles both increase rapidly to a peak value compared to the *No Impact* profile. Both the oscillations in the *59g* and *Combo* curves were of similar frequency suggesting that they were caused by the same phenomena. **The oscillations were thought to have been triggered by the sharp increase in load and perpetuated by the oscillation of the dummy mass above it mounting regions.** This hypothesis was supported by the modal

analysis. Frequencies of the oscillations in the *59g* and *Combo* curves were calculated to be 333 and 316 Hz respectively at the beginning of the simulation. Mode 6 of the modal analysis of the sled structure shows the sled deformed in a way similar to if the amplitude of these oscillations were increased. The eigenfrequency of this mode was 373.5 Hz, relatively close to those of the dummy mass accelerations.

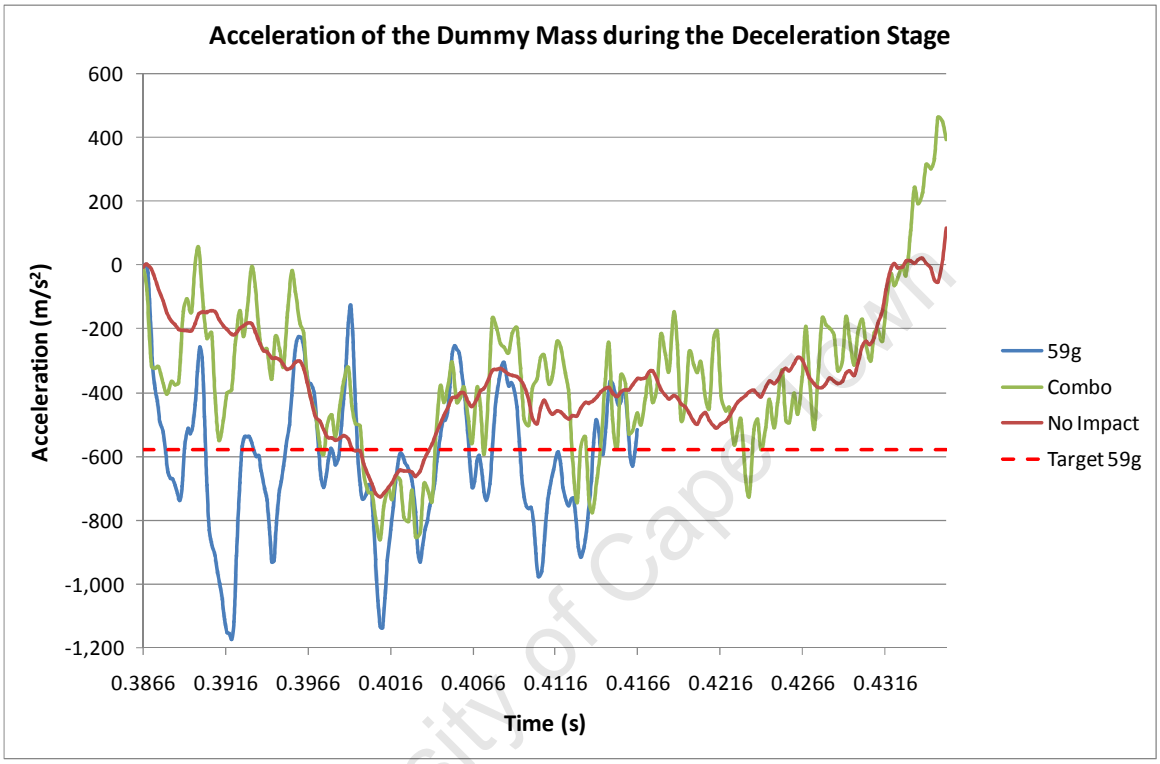

FIGURE 6-37: COMPARATIVE PLOT OF THE ACCELERATION EXPERIENCE BY THE DUMMY MASS DURING THE DECELERATION STAGE

A comparative plot of the dummy mass velocities for the different scenarios reiterates the similarity of the *Combo* and *No Impact* scenarios in terms of their dynamics. As in the kinetic energy plot the 59g scenario shows its higher overall deceleration with a steeper gradient of its descent during the deceleration stage.

The dips at the ends of the *No Impact* and *Combo* profiles are cause by the error mentioned in section 0. The error was due to a negative deceleration force which was applied to the sled as it was rebounding. Notice that the *59g* curve continues linearly into negative velocity region. The duration of the 59g step used in the simulation was roughly estimated as it was an idealised loading scenario.

The correct profile would be one where the dummy mass ceases to accelerate once the sled has lost contact with the piston and decelerates to rest under the frictional affects of the rails.

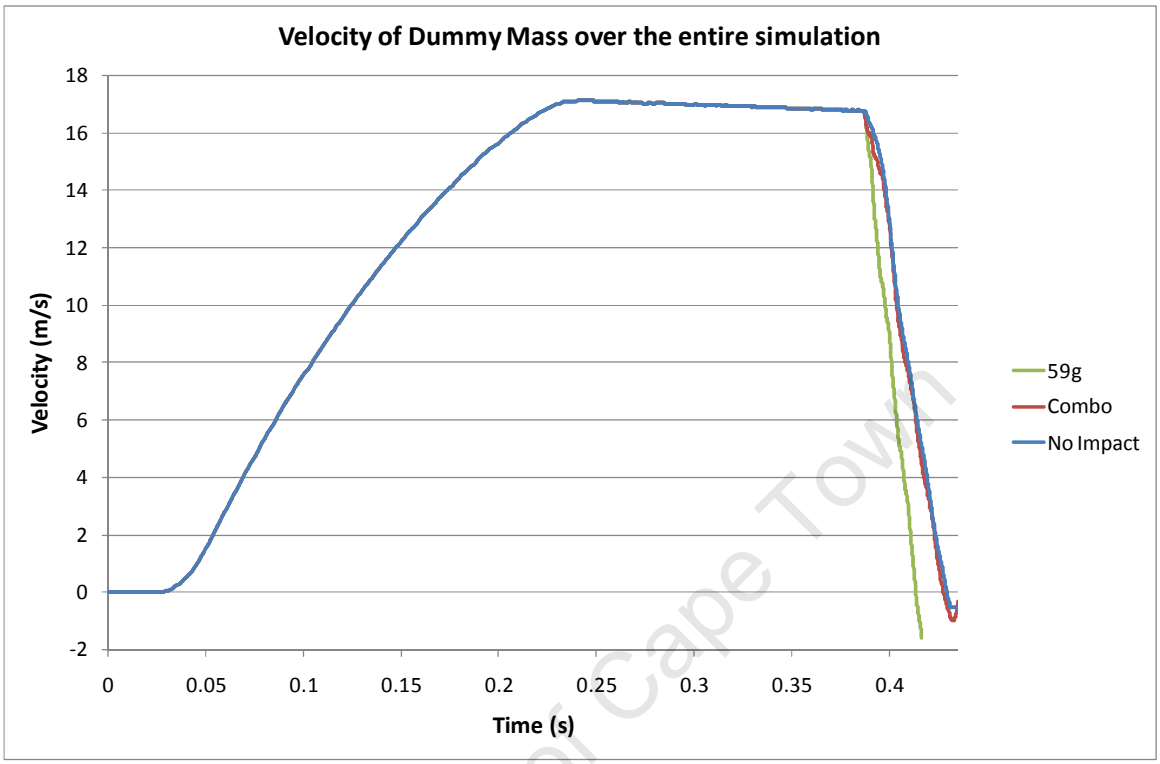

FIGURE 6-38: COMPARATIVE PLOT OF THE DUMMY MASS VELOCITY OVER THE ENTIRE SIMULATION

From the curve the maximum dummy mass velocity was at the end of the acceleration stage. The magnitude of this velocity was 17.13 m/s. This velocity was reduced to 16.83 m/s by the time the sled reached the end of deceleration piston.

These velocities were comparable to the velocities predicted by the Acceleration Stage model. The Acceleration Stage model predicted the sled velocity after the acceleration stage to be 17.39 m/s. By using the equation of motion for constant acceleration the sled velocity was predicted to be 17.06 m/s at the beginning of the Deceleration Stage.

Both simulations predicted similar losses in velocity over the coasting stage. The largest discrepancy between the simulations was during the acceleration stage, but this error was only 1.5 %. This discrepancy was due to the simpler friction assumption used to describe the rail friction in the Acceleration Stage model. The friction in the finite element model was

more complicated as it took into account the varying contact pressure at each of the slides, resulting in higher frictional forces.

The velocity profiles during the deceleration stage of the finite element model were slightly different to those of the Deceleration Stage. The obvious difference was the absence of the sudden drop in velocity at the start of the deceleration stage. This was excepted because the force profiles taken from the Deceleration Stage model had been modified. The reduction in the rebound velocity was not corrected in the force profile and can still be seen in the velocity prediction of the *Combo* and *No Impact* curves.

In general **there was good correlation between the velocity predictions from the different models**.

7 DISCUSSION

In the previous chapters the processes followed and the results obtained from these processes have been detailed. The Acceleration Stage model was shown to be able to predict the sled velocity and piston dynamics for any combination of the input parameters. This allowed the acceleration stage load profiles to be created and the predicted histories of a number of the cylinder parameters to be analysed.

In combining the models the results obtained by the Acceleration Stage model were incorporated into the Deceleration Stage model. This gave the results from the duration of the deceleration stage which, were relevant to the input parameters prescribed for the acceleration stage. By exploring the code of the Deceleration Stage model, the cause of the numerical anomaly was found to the method used to model the contact plate. After rectifying the anomaly with the assistance of auxiliary finite element simulations, the modified force profile was used as the deceleration stage loading in the main finite element model.

The results of the simulations run using the finite element model highlighted areas of the rail system which needed strengthening and assisted in the improvement of the conceptual sled design. Problem areas in the rail system were in the vicinity of the three cross members closest to the deceleration cylinder.

In this chapter, the following three issues will be discussed: the importance of the cushioning air and its effect on the pneumatic piston dynamics; the method used to model the contact plate and the consequences of this and finally, the stress concentrations at points in the rail system and suggestions on how to improve these.

Cushioning Air

The importance of the cushioning air system was shown in section 6.1, as well as the effects of using fewer than 6 acceleration valves. If less than 6 acceleration valves are used, the retract velocity of the piston starts to increase beyond the final sled velocity. This is not of much consequence except for in the 10 bar cases, where the retract velocity was predicted to be substantially above the specified maximum of 17 m/s for a simulation with one

acceleration valve. If less than six acceleration valves are to be used in the actual system, the affect of the increased piston velocity on components (like the piston supporting structure) must be investigated.

Simulations were run which showed how decreasing the number of cushioning air valves improved the piston dynamics, by reducing the retract velocity. As mentioned before, due to the realities of the pneumatic system all six deceleration valves have to be fired to ensure that the cushioning air is not exhausted to the atmosphere. (The exhaust ports of the acceleration valves, connected to the rear chamber, are all blocked off; allowing various combinations of the valves to be activated.) A simple solution to this would be to plug the exhaust ports of the cushioning valves that would not be fired. This would block the cushioning air from escaping through the exhaust ports of the unfired valves; having the same effect as reducing the number of cushioning valves in the acceleration stage simulation.

Although simple, the solution would require the ports on the valves to be blocked manually. This would introduce the possibility of human error affecting the cushioning air. If, due to operator error one of the unblocked valves was not fired, the cushioning air would escape through the unfired valve and impede the cushioning process. Without sufficient cushioning air pressure, the risk of impacting and damaging the piston or end cap increases severely.

The reality shown by Figure 6-7 is that no benefit would be gained by using input parameter sets which use only a few acceleration valves; as the resulting velocity profiles are similar to those of an input parameter set with a lower supply pressure and more acceleration valves. The only scenarios where a better input parameter set would not be able to be found would be for low velocity situations. In low velocity situations the risk of the piston impact causing damage is reduced by the lower kinetic energy of the piston. This allows the method of manually blocking the exhaust port to be used more safely.

Contact Plate Model

The two anomalies in the deceleration stage model stemmed from the contact plate model. The contact plate model accounted for the rubber stopper fixed to the end of the hydraulic cylinder. The model converted the positions and velocities of the sled and deceleration piston into the decelerating force experienced by the sled.

The main anomaly was the large spike in force as the sled made contact with the end of the piston. This was not an error in the model but an attribute of the spring mass model used to model the rubber. The high spring constant reduced the stable time increment to less than was practical. The spring mass model, which was created to verify that the spike was indeed due to the use of a spring mass model, was still unstable when a time increment of 0.001 ms was used.

The actual magnitude of the impact event was investigated using auxiliary finite element simulations which calculated the worst case scenario of the impact force (metal on metal contact during the impact). These results were used in the *Combo* load profile. When the properties for the rubber stopper were included into the contact interaction between the piston and the sled, the force at the impact event disappeared. This was modelled using the *No Impact* load profile, which was effectively the force profile from the deceleration stage model with the spike anomaly removed. If the constants given in the Deceleration Stage model correctly described the rubber stopper, the *No Impact* load profile would be close to the actual loading scenario experienced by the sled.

What all these models relied on were the spring and damping constants of the rubber stopper. The spring constant received with the Deceleration Stage model was high, 2000 kN/mm. As shown before the stiffness relates to a Young's modulus of 2 GPa.

Although this is reasonable value for rubber, compression tests were performed using a universal tester which contradicted the value of the spring constant. The force-displacement curves for quasi-static compression tests performed on an identical rubber stopper showed a much lower stiffness value. As the material properties for rubber compounds are complicated, hyper-elastic and strain rate dependent, the validity of quasi-static testing is

questionable. For this reason the constants provided by the suppliers were used in the study and the discrepancy in the constant was highlighted here in this discussion.

The other irregularity in the contact plate model was the decrease in the rebound velocity due to the method used to ensure that the cylinder only decelerated the sled. The effect that this had on the results was minimal as it only affected the sled dynamics after the sled had rebounded. It must be noted that the final rebound velocity of the sled is in fact the minimum value on the curve and not the last value outputted by the simulation. As the rebound velocities were negative, this meant that magnitude of the actual rebound velocity was greater than the final outputted velocity.

The importance of the rebound velocity was the fact that, this was the velocity at which the sled would travel back towards pneumatic cylinder. This would have implications if the friction effects of the rail and slide interaction could not bring the sled to rest before it reached the end of the pneumatic cylinder. If this were the case the sled would collide with the pneumatic cylinder which could possibly still be oscillating. The uncontrolled nature of this collision could cause damage to both the sled and the pneumatic cylinder.

Stress Concentrations

A number of regions were found in the finite element analysis to have high localised stresses. The regions in the sled and slides were not a problem as they were both conceptual designs. The results of the finite element model showed that the concepts would survive the loading after some minor design changes which addressed the localised stresses.

However, the regions in the rail system posed more of a problem. As the rail system had already been constructed, methods to reduce the stresses by modifying the existing design as little as possible were necessary.

Stress concentrations were present at the connections between the braces and the rail supports. Some of this was due to the simplifications made to the interactions between the components. The stresses in the physical components could be improved by fitting a larger washer between the nut and the rail support to distribute the load over a larger area.

In the case of the stresses at the ends of the cross members a more substantial solution was needed. The loads felt by the cross members are transferred through bolts which fasten

them to the rail supports. By stiffening the rail supports in the X direction and grounding them through other means as well as by the cross members, these stresses would be relieved. These changes would also improve the stresses at the brace connection points.

Deflections of the rail supports caused moments to be applied at both ends of the cross members. These moments caused the cross members themselves to bend, which in turn compressed the grounding bolts; resulting in high stresses in the flange area between the grounding bolts and the bolts themselves. As mentioned before the physical cross member flanges would not show the same stress concentrations; the channels sections were not fastened together at this point and would pull apart slightly. To minimise this, the displacements of the rail supports needed to be reduced; this would consequently reduce the moments on the cross member and the loading of the braces.

A suggestion of modifications to the rail system which would achieve this is given in Appendix A. The reduction in the stress concentrations was verified by incorporating the modifications into the finite element model.

8 CONCLUDING REMARKS

From the investigations into the dynamics of the different aspects of the BISRU Sled Tester, the following were achieved and realised.

A computational model of the Acceleration Stage was created. The model is able to predict the dynamics of the sled and the piston for different combinations of input parameters. From these predictions the suitability of the simulated test can be assessed as well as the input parameters needed to achieve the desired final sled velocity.

Using the model, the dynamics of the piston were analysed. From the analysis it was found that faced with a choice between multiple sets of input parameters which resulted in similar final sled velocities, the set with the most acceleration valves should be chosen. The simulations showed that increasing the number of acceleration valves: decreased the time taken by the piston to come to rest after the sled had been released and the average acceleration of the sled was slightly lower.

If less than 6 acceleration valves were used the flow rate of the cushioning air was higher than that of the acceleration air. Although the flows did not occur simultaneously, the lower acceleration air flow rate resulted in lower rear chamber pressures. This teamed with the relatively high cushioning air flow were the causes of the unfavourable piston dynamics that were found in the simulations with lower number of acceleration valves.

The time taken for the piston to come to rest was found to increase quadratically with a decrease in the number of acceleration valves.

The model of the deceleration stage created by the suppliers of the hydraulic equipment, MOOG, was investigated and the outputs modified to allow them to be integrated into the finite element model. Velocity and force histories were not outputted by the original simulation, but were necessary to be able to create loading profiles for the finite element analysis.

Simulations run with Deceleration Stage model showed that the target deceleration of 59g could be achieved by the system. They also highlighted the importance of having a **high enough set point pressure to decelerate the sled over the stroke of the cylinder**. If the set

point pressure was too low the cylinder would bottom out and the sled and the cylinder itself would be damaged.

Two errors were found in the Deceleration Stage model. The first, a numerical anomaly which created a fictitious spike in the force experienced by the sled as it made contact with the end of the hydraulic piston. The second, an error in the calculation of the contact plate damping, which predicted a reduction in the rebound velocity of the sled. The spike caused by the anomaly was manually removed from the loading profiles. The remaining part of the profile was appended to the force prediction from an impact simulation created using finite elements. These combined load profiles were used to load the sled in the main finite element model during the deceleration stage. No changes were made to rectify the rebound velocity error, as the actual rebound velocity can easy be read off the plots.

Note needs to be taken of **the presence of the rebound velocity**. If the rebound velocity is larger than 3.5 m/s, a simple application of the equations of motion predict that the sled will continue sliding until within the reach on the pneumatic cylinder. This could result in unwanted impact between the sled and the pneumatic cylinder, depending on the position and velocity of the piston. It is suggested that the rebound velocity is accounted for in the design of the sled to avoid any collisions.

The finite element analysis of the structural parts of the system revealed the **modifications to the rail system were necessary**. The interaction between the sled's slides and the rails created high stress points: at the connections between the braces and the rail supports and in the cross members in the vicinity of the grounding bolts. Modifications to the rail system which alleviate these stresses are suggested in Appendix A.

The sled model showed the design to be conceptually sound. Apart from stress concentrations at the connection points of the mounting brackets, the stresses were found to be less than 100 MPa. By modifying the bracket design, the stress concentrations would be removed and the required yield strength of the material lowered. An aluminium alloy with a yield of 200 MPa would result in a design factor of 2. This would lead to a cost saving by allowing a lower grade alloy to be used. Aluminium 6082-T6 with a yield strength of 250 MPa and is a weldable alloy is recommended as a replacement for the afore specified Aluminium 7015-T5.

The stresses in the ERTACETAL C polymer used for the slide never reached its yield point. What was not modelled was the wear of these components. ERTACEL C is manufactured to be used in sliding applications and has good wear characteristics. A similar product was used by Wichita State University; their slides experienced 0.4 mm of wear over 13 years of use(31). The wear was regarded not to have any significant impact on the slides, but should be monitored during periodic maintenance intervals.

The dynamics of the mass which represented the test specimen showed similar velocity profiles to those predicted by the Acceleration and Deceleration Stage models. A plot of the dummy mass acceleration showed that the *Combo* and *59g* load profiles caused the mass to oscillate in the Z direction. These oscillations were found to have similar frequencies to the eigenfrequency of the 6^{th} eigenmode of the sled. The deformations seen in mode 6 would have caused the mass to move in the Z direction. This suggested that the steep gradient of the force profiles excited this eigenmode.

The excitation was not apparent in the *No Impact* simulation which was the loading scenario closest to that which would probably be experienced by the actual sled. The amplitudes of the oscillation in the other two simulations were small and did not affect the structural integrity of the system. For these reason this **excitation was not thought to be significant**.

9 WORKS CITED

1. **Moog Controls Limited.** Sled Deceleration Control System MatLab/Simulink Simulation. 1 July 2005. Issue C.

2. *Sled Tester Simulation Documentation.* **FESTO.** 2004.

3. **Urban, Bernard.** *Magnetic Brakes for Sled Tester.* s.l. : InTraSys, 2005.

4. **Balchin, Keith.** Private conversation with. 29 June 2009.

5. **AMR representives.** Conversations. 2009.

6. **Moog Controls Limited.** Sled Deceleration System Control Matlab/Simulink Simulation - Model Operation. 6 December 2005. Issue: A.

7. **Norgren Pneumatics.** Avoiding the Bounce. *Hydraulics & Pneumatics.* [Online] [Cited: 16 April 2009.] http://www.hydraulicspneumatics.com/200/Issue/Article/False/17815/Issue.

8. **Beater, Peter.** *Pneumatic Drives: System Design, Modelling and Control.* Berlin : Springer, 2007.

9. **Cengel, Yunus A and Boles, Micheal A.** *Thermodynamics An Engineering Approach.* 4th Edition. New York : McGraw-Hill, 2002.

10. **Engineers Edge.** Pressure Drop Along Pipe Length. *Engineers Edge.* [Online] [Cited: 28 January 2009.] http://www.engineersedge.com/fluid_flow/pressure_drop/pressure_drop.htm.

11. **Douglas, John F, Gasiorek, Janusz M and Swaffield, John A.** *Fluid Mechanics.* 4th Edition. Harlow : Pearson Education Limited, 2001.

12. **Beck, S and Collins, R.** *Moody diagram. lines created using Swami and Jaine formula.* University of Sheffield, s.l. : Wikimedia Commons, 2008.

13. **Binder, R C.** *Fuild Mechanics.* Englewood Cliffs, New Jersey : Prentice-Hall iInc., 1973.

14. *An improved dynamic model of pneumatic actuators.* **Mare, J C, Geider, O and Caen, R.** 2, International Journal of Fluid Power, Vol. 1, pp. 39-47.

15. **Kefer, Joachim.** Email conversation. s.l. : FESTO Germany, 21 April 2009.

16. *Friction Models and Friction Compensation.* **Olsson, H, et al.** 4, s.l. : The European Union Control Association, 1998, pp. 176-195.

17. *Identification and Model-based Compensation of Stribeck Friction.* **Marton, Lorinc and Lantos, Bela.** 3, Budepest : s.n., 2006, Acta Ploytechnica Hungarica, Vol. 3.

18. *The effect of a tangential force on the contact on metalic bodies.* **Courtney-Pratt, J and Eisner, E.** 1957. Proceedings of the Royal Society. Vol. A238, pp. 529-550.

19. *Friction at a lubricated line contact operating at oscillating sliding velocities.* **Hess, D P and Soom, A.** 1990, Journal of Tribology, Vol. 112, pp. 147-152.

20. *The role of the rate of application of the tangential force in determining the static friction coefficient.* **Johannes, V I, Green, M A and Bockley, C A.** 1973, Wear, pp. 381-385.

21. *Surface friction under time-dependent loads.* **Richardson, R S H and Nolle, H.** 1, 1976, Wear, Vol. 37, pp. 87-101.

22. *A New Model for Control of Systems with Friction.* **Canudas de Wit, C, et al.** 3, 1995, IEEE Transaction on Automatic Control, Vol. 40, pp. 419-425.

23. **Moog Controls Limited.** *Sled Deceleration Control Simulation (SDS_5.mdl).* [Simulation] Ashchurch : s.n., 2005.

24. **Balden, Victor.** Private Conversation with. 2009.

25. **Gilbert Curry Industrial Plastics.** ERTACETAL C Datasheet. *Gilbert Curry Industrial Plastics Co Ltd.* [Online] June 2001. [Cited: 24 Febuary 2009.] http://www.gcip.co.uk/pdf/ERTACETALC.PDF.

26. **IDES.** Tensile Properties - ISO 527. *IDES - Plastic Web.* [Online] [Cited: 27 July 2009.] http://www.ides.com/property_descriptions/ISO527-1-2.asp.

27. **Maizey Plastics.** Physical Properties Table of Engineering plastics. 2004.

28. **Goodfellow Cambridge Ltd.** Polyoxymethylene - Copolymer (Acetal-Copolymer POMC) Material Information. *GoodFellow R&D Materials.* [Online] [Cited: 26 Febuary 2009.] http://www.goodfellow.com/E/Polyoxymethylene-Copolymer.html.

29. **Micro Plastic Inc.** DuPontDerlin Supertough Acetal. *Micro Plastics Inc - Plastic Fasteners.* [Online] [Cited: 27 Febuary 2009.] https://secure.microplastics.com/Materials/ACETAL%20IMPACT%20MODIFIED.htm.

30. **Hughes, Thomas.** *The Finite Element Method: Linear Static and Dynamic Finite Element Analysis.* Dover : Dover Pubications Inc., 2003.

31. **Mitchell, Joseph.** Archived email conversation with. s.l. : Wichita State University, 30th July 2004.

32. *A new method of specifying the flow capacity of pneumatic fluid power valves.* **Sanville, F E.** 195, 1971, Hydraulic Pneumatic Power, Vol. 17.

APPENDIX A: A RECOMMENDED SOLUTION

CONTENTS

List of Figures ..... A ii

A-1 Introduction ..... A 1

A-2 Reasons for Modifications ..... A 2

A-3 Proposed Solution ..... A 2

A-4 Verification of the Concept ..... A 4

A-4.1 Bracket Model ..... A 4

A-4.1.1 Assembly ..... A 6

A-4.1.2 Constraints ..... A 6

A-4.1.3 Loading ..... A 7

A-4.2 Results of the Modifications ..... A 7

A-5 Concluding Remarks ..... A 9

LIST OF FIGURES

Figure A-1: Sketch of the bracket design ..... A 3

Figure A-2: Dimensioned sketch of the bracket design ..... A 3

Figure A-3: Graphical representation of the shell normals and offsets ..... A 4

Figure A-4: Information regarding the meshing of the bracket ..... A 5

Figure A-5: Image showing the positions of the brackets relative to the rail system ..... A 6

Figure A-6: Image showing the brackets not interfering with the sled path ..... A 7

Figure A-7: Maximum stress state of the rail system after the inclusion of the brackets ..... A 8

Figure A-8: Close up of the stress concentration found in the channel section of the front right hand bracket ..... A 8

A-1 INTRODUCTION

The finite element analysis of the rail system of the BISRU sled tester revealed that the design was not strong enough to withstand the loading exerted on it by the sled. While the stresses during the acceleration and coasting stages were below the safe limit of 100 MPa; the stresses increased to 211 MPa and 235 MPa in the deceleration stage when loaded with the *Combo* and *59g* profiles respectively.

The safe limit of 100 MPa was chosen to provide a design factor of 2. The rail system was constructed from mild steel which typically has a yield strength of 250 MPa, but can reduce to 200 MPa depending on the origin of the steel.

From the finite element analysis, it was seen that the stresses were concentrated in the vicinity of the grounding bolts of the three cross members closest to the hydraulic cylinder and connection points of the braces above these cross members. For this reason the proposed modifications focus on these areas.

A finite element simulation run to assess the effectiveness of the modifications showed that the stresses in the rail system were reduced below 103 MPa. The stresses in the brackets added to the rail system were found to be below 115 MPa. The proposed modifications did not interfere with the sled path.

A-2 REASONS FOR MODIFICATIONS

From the original analysis, the cause of the high stresses in the cross members and at the brace connection point were found to be due to the deflections of the rail supports. During the deceleration of the sled, the rails were deflected outwards causing a moment to be applied to the ends of the cross members and the braces to be loaded in tension. The moments applied to the cross members caused them to bend, compressing the grounding bolts; thus increasing the stresses in them as well.

The solution aimed to reduce the outwards deflection of the rail supports as well as give vertical support to reduce the loading on the ground bolts. By reducing the outwards deflection the moment transferred to the cross members as well as the tension in the braces would be relieved.

A-3 PROPOSED SOLUTION

The solution needed to relieve the stresses in the system, while not interfering with the path of the sled. The cost of the modifications was also a concern. It was desired that the existing constructed should not be changed and that if possible material left over from the construction should be used to strengthen the system.

A simple yet effective solution was found which satisfied all these specifications. Substantial brackets, manufactured from channel section left over from the construction of the rail supports, were designed. The brackets were made to be mounted at three points along each of the rail supports; one at each end of the three cross members closest to the hydraulic cylinder. Figure A-1 shows a sketch of one of the brackets. The brackets are 470 mm in height and 320 mm long.

Dimensions of the brackets are given in Figure A-2 (dimensions in mm).

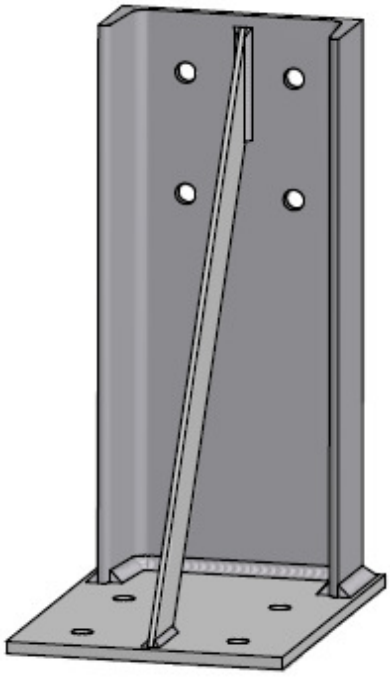

FIGURE A-1: SKETCH OF THE BRACKET DESIGN

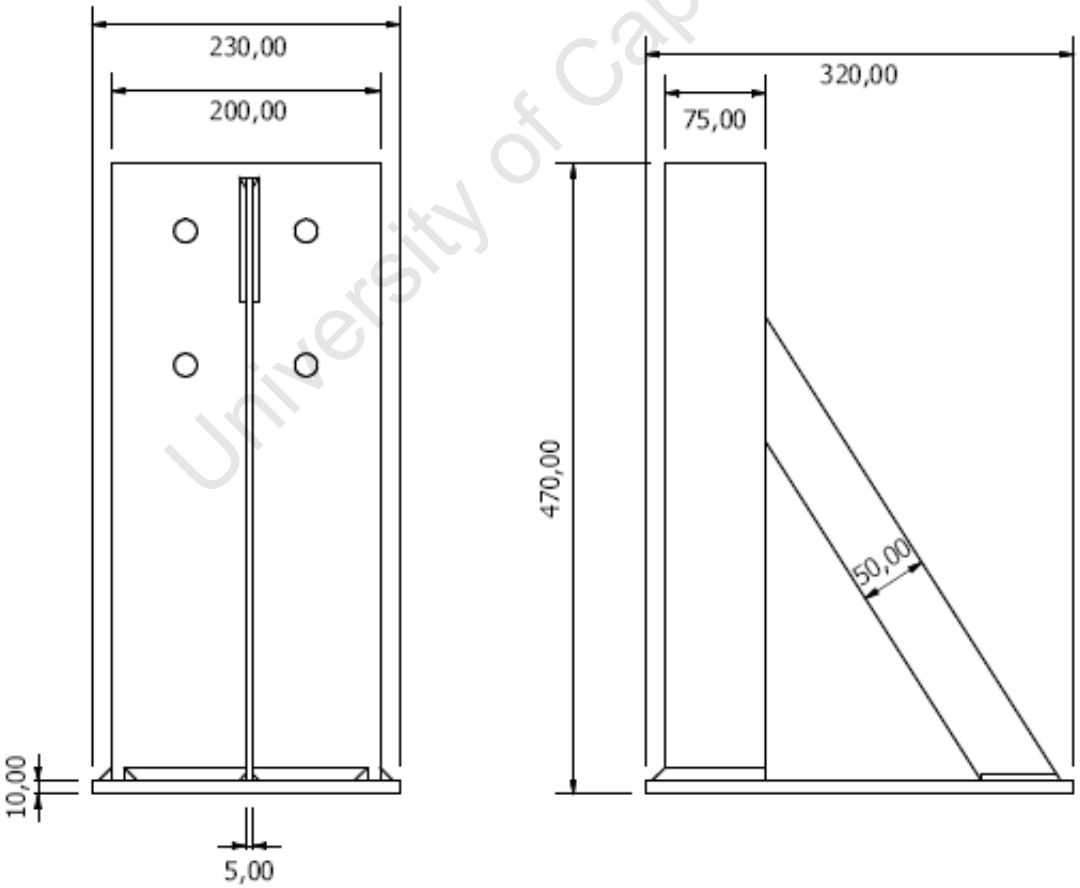

FIGURE A-2: DIMENSIONED SKETCH OF THE BRACKET DESIGN

A-4 VERIFICATION OF THE CONCEPT

To verify that the addition of the brackets would indeed reduce the stresses in the rail system a finite element model, including the brackets, was run. A model of bracket was created and added to the existing model created to analyse the sled and rail system.

As the bracket design was relatively simple, a shell model could be used. The brackets were placed in the correct positions relative to the rail system and the nodes of the relevant regions of the brackets and the rail supports tied to each other. The bases of the brackets were constrained by their translational degrees of freedom.

A-4.1 BRACKET MODEL

The entire bracket was made of mild steel. Hence mild steel properties were assigned to the bracket model. 10 mm sections were assigned to the channel section and the base plate; the gusset was assigned a 5 mm section. The shell normals and offsets are shown in Figure A-3. The bracket was meshed as detailed in Figure A-4.

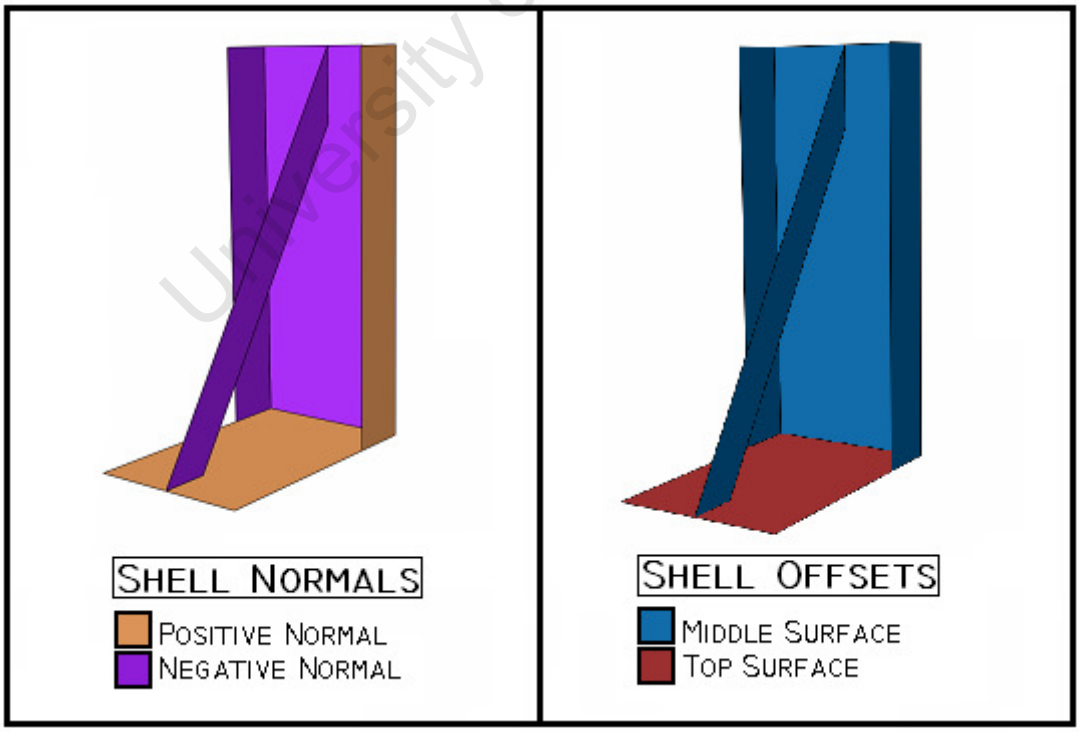

FIGURE A-3: GRAPHICAL REPRESENTATION OF THE SHELL NORMALS AND OFFSETS

PART: BRACKET

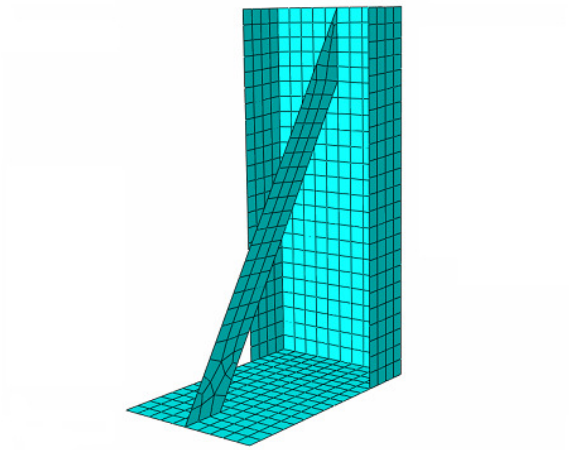

ELEMENT TYPE:

S4: A 4 NODED GENERAL SHELL

NUMBER OF ELEMENTS:

650

STABLE TIME INCREMENT:

1,42 E-6 S

MINIMUM EDGE LENGTH:

6,57 MM

AVERAGE ELEMENT SIZE:

18,2 X 28 MM

FIGURE A-4: INFORMATION REGARDING THE MESHING OF THE BRACKET

A-4.1.1 ASSEMBLY

The brackets were placed on the inside of the rail supports. Although this meant that path of the sled had to be avoided; it would be simpler to connect to the brackets to the flat side of the rail supports and there would be no interference with components outside the rail system footprint. Figure A-5 shows the positions of the brackets. The edges of the brackets are typically 45 mm from the closest cross member.

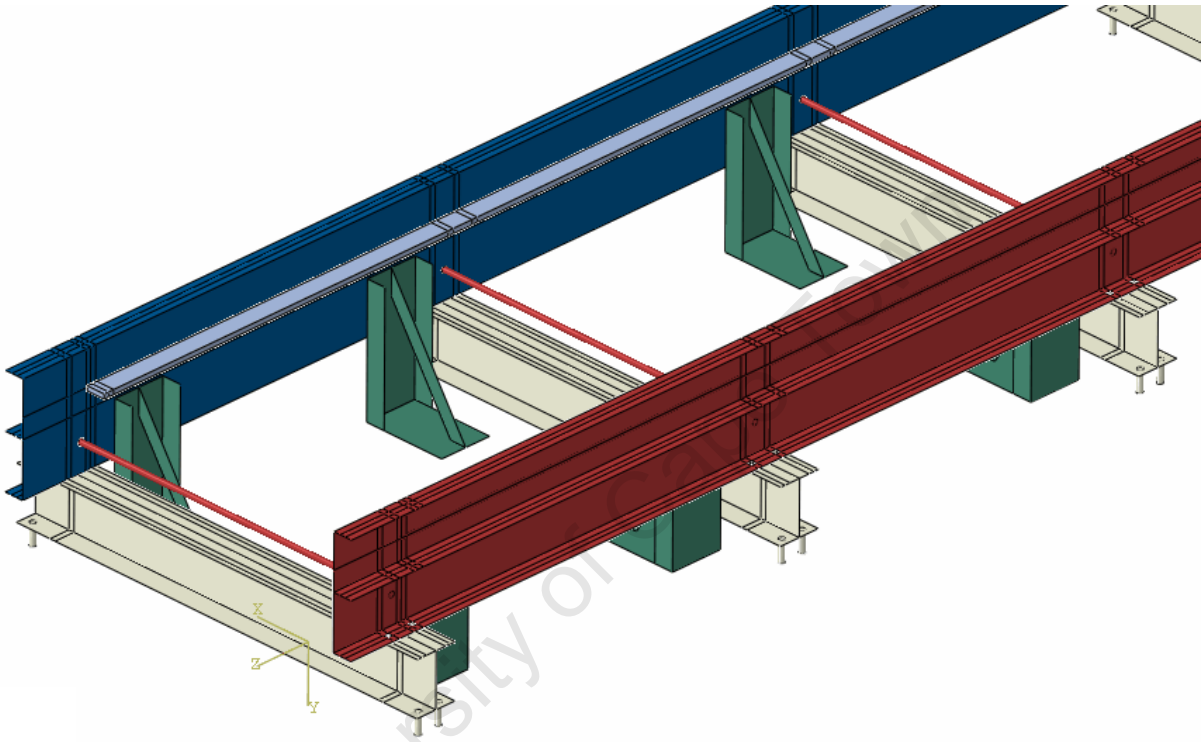

FIGURE A-5: IMAGE SHOWING THE POSITIONS OF THE BRACKETS RELATIVE TO THE RAIL SYSTEM

A-4.1.2 CONSTRAINTS

The original rail system was constrained as before, by applying encastre constraints to the ends of the grounding bolts. The addition of the brackets meant the rail supports were also constrained, via the tie constraint with the bracket, by the pinned constraint applied to the bases of the brackets.

The interaction between the sled and the rails was kept identical to that used in the original model.

A-4.1.3 LOADING

In order to minimise the run time and as the stresses during the acceleration and deceleration stages were not significant, the model was started at the beginning of the deceleration stage.

The position of the sled as the deceleration loading was initiated was important. The sled was place 1 m from the end of the rails and given an initial velocity of 17 m/s. The *59g* force profile was then applied to the same reference point as in the original simulation. The *59g* profile was chosen as it had resulted in the highest stresses originally.

This loading was effectively the same as modelling the entire acceleration and coasting stages.

A-4.2 RESULTS OF THE MODIFICATIONS

The simulation showed that the inclusion the bracket greatly reduced the stress in the rail system. The regions of maximum stress changed from the cross members to the vicinity of the rails. These stresses were below 103 MPa (shown in Figure A-7).

The maximum stress in the cross members was reduced to below 50 MPa. The stresses in the brackets are generally below 100 MPa; an isolated increase of the stress to 114.3 MPa was found in the corner of the right hand bracket (shown in Figure A-8). The actual channel section used in the bracket design has a large fillet in this region which would reduce this stress.

The design and placement of the brackets kept the sled path clear. No obstructions were caused by the brackets.

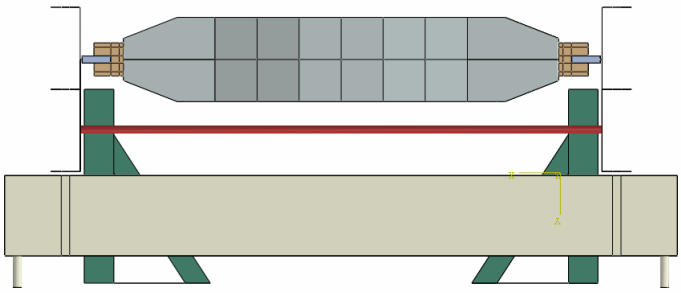

FIGURE A-6: IMAGE SHOWING THE BRACKETS NOT INTERFERING WITH THE SLED PATH

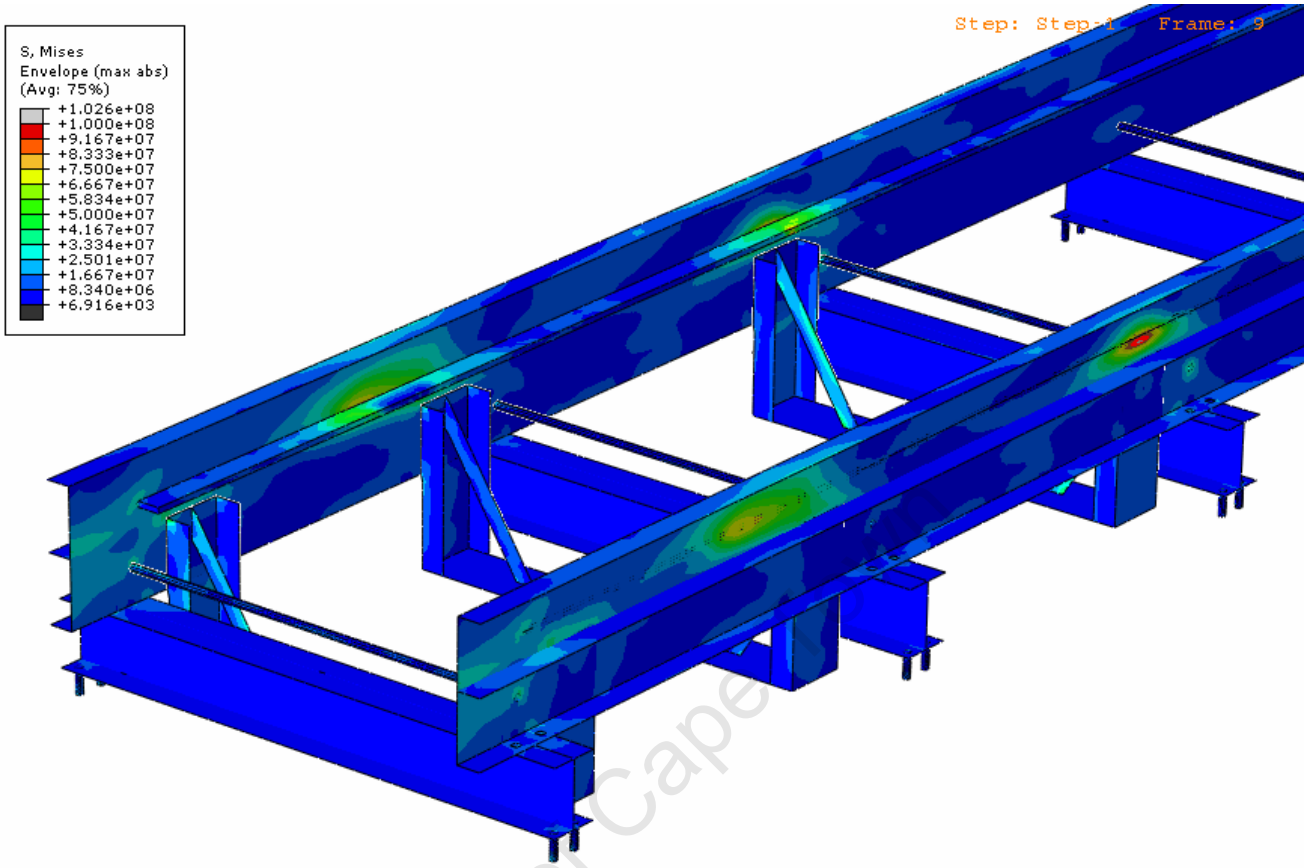

FIGURE A-7: MAXIMUM STRESS STATE OF THE RAIL SYSTEM AFTER THE INCLUSION OF THE BRACKETS

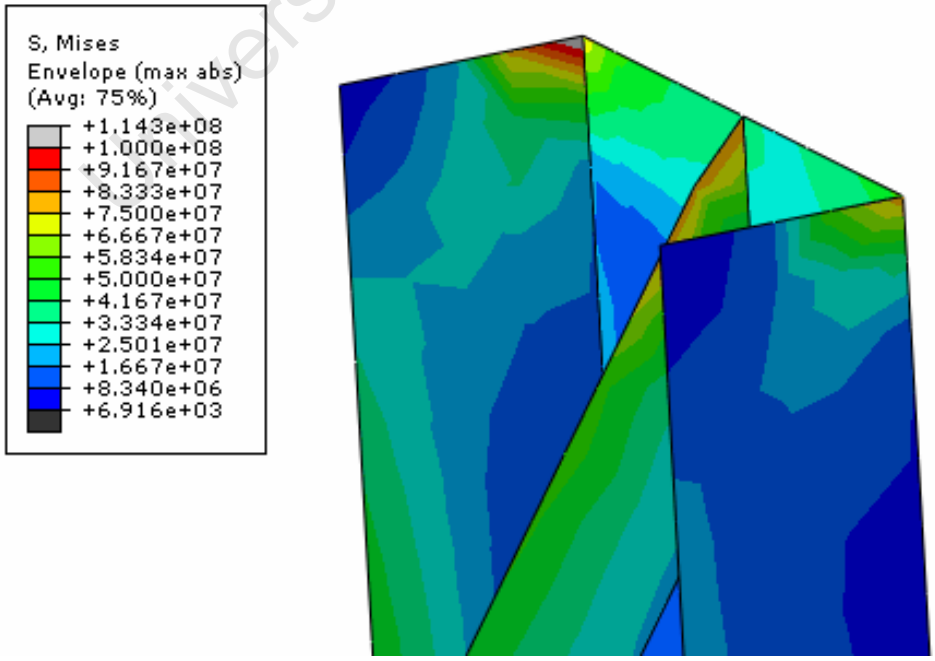

FIGURE A-8: CLOSE UP OF THE STRESS CONCENTRATION FOUND IN THE CHANNEL SECTION OF THE FRONT RIGHT HAND BRACKET

A-5 CONCLUDING REMARKS

The verification of the solution carried out using the finite element model showed that the brackets would relieve the stresses in the rail system.

The slight increase above the stipulated 100 MPa level was not an issue as the stress peaked at 102.6 MPa which was acceptable. The four areas of higher stress shown in Figure A-7 were a result of the interaction between the slides and the rails. As the sled only interacts with the rails through the slides these localisations occur.

The strength of the bracket design is adequate. The peak stress of 114.3 MPa was due to the simplification of the channel section; the fillet is the actual section would reduce this stress.

The proposed positioning and design of the bracket will not interfere with the path of the sled.

The addition cost of adding the bracket is minimal, as the brackets have been designed to use material remaining from the rail system construction.

It is recommended that the brackets are manufactured and installed to strengthen the rail system.